PHOTOPRODUCTION OF ETA MESONS FROM HYDROGEN AT PHOTON ENERGIES BETWEEN 0.8 AND 1.45 GeV

Thesis by

Leon S. Rochester

In Partial Fulfillment of the Requirements

For the Degree of

Doctor of Philosophy

California Institute of Technology

Pasadena, California

1968

(Submitted May 14, 1968)

ACKNOWLEDGEMENTS

As in our earlier experiments, the success of this effort is in a large part due to the cooperation of every member of our group. My advisor, Clemens Heusch, conceived the experiment, and provided much help and advice during all phases of the construction, running, and analysis. Elliott Bloom and Charles Prescott assisted in all aspects of the experiment. Thanks are also due to the other members of the group for sharing the task of running. Walter Nilsson constructed much of the apparatus used in this experiment, and I gratefully acknowledge his skill and patience.

My thanks go to the synchrotron crew, under Larry Loucks and Paul Van Ligten , to Earle Emery and Dick Wileman, and to the synchrotron operators, headed by Al Neubieser, for their continued assistance.

I am grateful to our scanners for their careful work, and especially to Sherwood Wilner who supervised the scanning operation and kept it running smoothly. I thank Phyllis Nilsson for her programming help and her assistance in the details of preparing this thesis.

For financial support I am indebted to the National Science Foundation, the Atomic Energy Commission, and to the California Institute of Technology.

Finally, I gratefully acknowledge the aid of my typist, who is also my wife, whose constant encouragement and support helped to make this work possible.

ABSTRACT

We measured the differential cross section of the process $\gamma p \to p\eta$ at the 1.5 GeV Caltech electron synchrotron, at photon energies from 0.8 to 1.45 GeV, at various angles between 45° and 100° in the center of mass. A counter-spark chamber array was used to determine the kinematics of all particles in the final state of the partial mode $\gamma p \to p\eta$ ($\eta \to 2\gamma$). Analysis of 40,000 pictures yielded 6,000 events above a background which varied with energy from 5% to 30% of foreground. The cross section shows an energy dependence confirming earlier results up to 1000 MeV, but with improved statistics; it then remains roughly constant (at 50° C.M.), to 1.45 GeV. The data show a small angular variation, within the limited range covered, at energies between 1000 and 1100 MeV.

TABLE OF CONTENTS

TABLE OF CONTENTS (cont.)

LIST OF FIGURES

LIST OF FIGURES (cont.)

LIST OF FIGURES (cont.)

LIST OF FIGURES (cont.)

LIST OF TABLES

To Myrna

"Going on an Expotition?" said Pooh eagerly. "I don't think I've ever been on one of those. Where are we going to on this Expotition?"

"Expedition, silly old Bear. It's got an 'x' in it."

"Oh!" said Pooh. "I know." But he didn't really.

"We're going to discover the North Pole."

"Oh!" said Pooh again. "What is the North Pole?" he asked.

"It's just a thing you discover," said Christopher Robin carelessly, not being quite sure himself.

I. INTRODUCTION

In this experiment we measure the reaction

$$\gamma + p \rightarrow p + \eta$$

at photon energies from 0.8 to 1.45 GeV.

The discovery of the η meson was reported in 1961 by Pevsner et al.[1] who studied the reaction

$$\pi^+ + d \rightarrow p + p + \pi^+ + \pi^- + \pi^o$$

in a bubble chamber. The three pion effective mass spectrum exhibited a peak at about 550 MeV, in addition to the ω peak.

The observation of the η in the process[2]

$$k^- + p \rightarrow \Lambda + \pi^+ + \pi^- + \pi^o$$

led to the conclusion that the isotopic spin of the eta was either zero or one. Several experiments have looked for the charged counterpart of the η, but none has been found, which demonstrates that the isotopic spin of the η is zero.

If this is the case, then the η may not decay into $3\pi^o$'s and still conserve isotopic spin. The fact that this decay does occur with a large probability and also that π^o's are involved, led to the conjecture that the η

decays via the electromagnetic interaction, which does not conserve isotopic spin.

This was verified when the decay[3]

$$\eta \rightarrow \gamma\gamma$$

was observed. This also proved that the η could not have spin one.

This result, combined with an analysis of the Dalitz plot for 3π decays of the eta, showed that the spin parity assignment of the η is

$$J^{PG} = 0^{-+}$$

Numerous bubble chamber experiments have identified and measured the different decay modes of the η, with often inconsistent results. In a recent analysis of these data, C. Baltay[4] has shown that the difficulty arises in the measurement of $\Gamma(\eta \rightarrow \pi^o\gamma\gamma)/\Gamma(\eta \rightarrow \gamma\gamma)$. When two of a total of nine experiments are excluded from the fit, the inconsistencies disappear, and the results shown in Table 1.1 obtain.

A recent measurement[5] of the partial width $\Gamma_{\gamma\gamma}$, performed by isolating the diagram shown in Figure 1.1 (f), has shown that the width of the eta is

$$\Gamma_{\gamma\gamma} = 1.2 \pm 0.5 \text{ keV}$$

Table 1.1

Main Decay Modes and Branching Ratios of the Eta Meson

Decay Mode	Fraction (%)
$\pi^+ \pi^- \gamma$	5.7 ± 0.6
$\pi^+ \pi^- \pi^0$	23.0 ± 1.2
$\pi^0 \pi^0 \pi^0$	29.0 ± 2.5
$\gamma \gamma$	40.3 ± 1.6
$\pi^0 \gamma \gamma$	2.0 ± 1.6

or

$$\tau_\eta \simeq 10^{-19} \text{ seconds.}$$

The η was first observed to occur in photoproduction in 1962.[6] The first feature of the cross section to be observed was the striking enhancement at threshold, which seemed to be isotropic in production angle. This same effect was observed in pion production of η's.[7] At first this was thought to be connected with the $P_{11}(1400)$ resonance, but subsequent work indicates that the $S_{11}(1570)$ resonance seems a more likely candidate.

The diagrams which can contribute to eta photoproduction are shown in Figure 1.1.

Charge conjugation invariance precludes the exchange of a π^o or η. Exchange of a photon ("Primakoff Effect") has been observed from heavy nuclei in the extreme forward direction. Exchanges of vector mesons or nucleon isobars (t and u channel processes) are not expected to be very important at low energies.

Contribution of the nucleon Born terms to π^o photoproduction in the isobar region are found experimentally to be much smaller than calculation of these first order diagrams would predict. This may also be true in η photoproduction.

Among the direct channel diagrams, the S_{11} resonance has already been mentioned. In this regard it is interest-

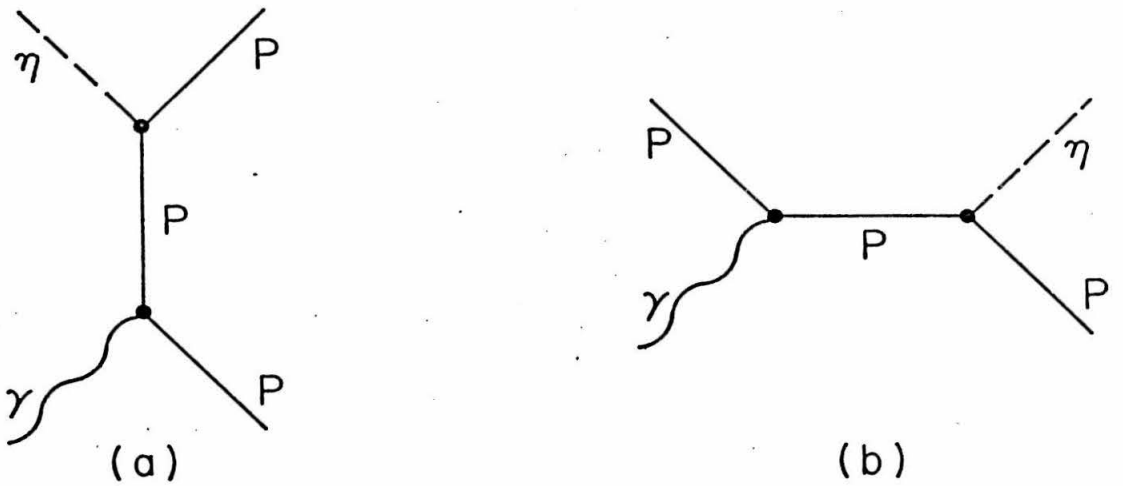

NUCLEON BORN TERMS

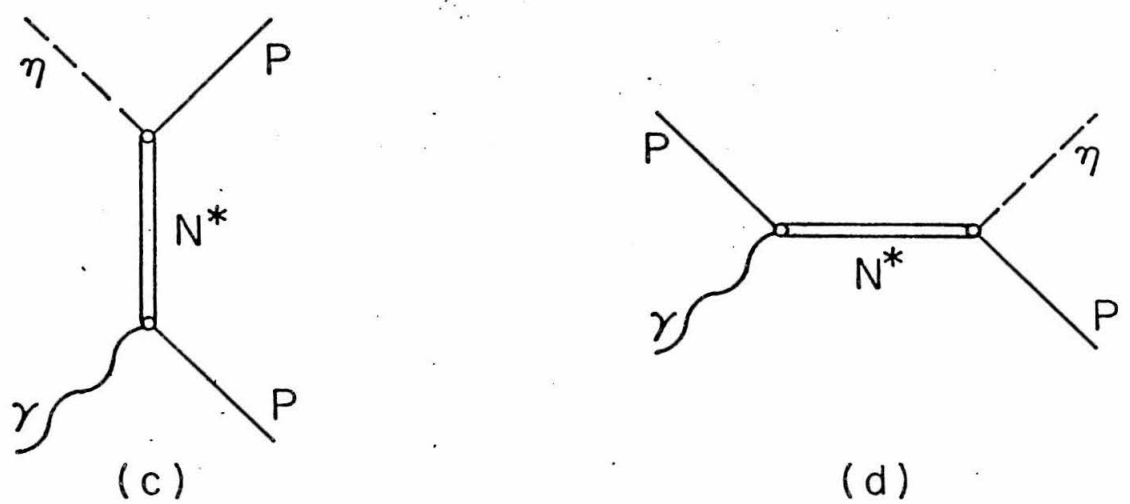

s AND u CHANNEL PROCESSES WITH
EXCHANGE OF I = ½ RESONANCES
[$D_{13}(1525)$, $S_{11}(1570)$, $D_{15}(1670)$, $F_{15}(1688)$, ETC.]

Figure 1.1 Diagrams which can contribute to eta photoproduction

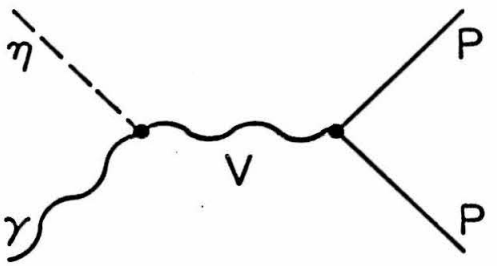

(e)

t CHANNEL PROCESSES WITH
EXCHANGE OF VECTOR MESONS (ρ, ω, ϕ)

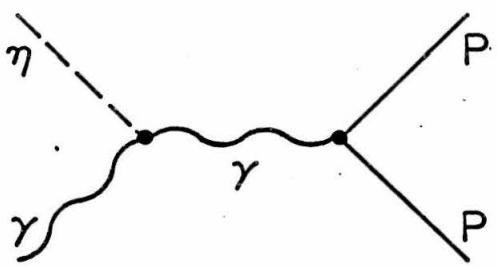

(f)

PRIMAKOFF EFFECT

Figure 1.1 (cont.) Diagrams which can contribute to eta photoproduction

ing to note that threshold enhancements have been observed in the $\Lambda\eta$ and $\Sigma\eta$ systems,[8,9] leading to the conjecture that perhaps these effects represent the presence of a new baryon-eta octet.[10] (The $\Lambda\eta$ enhancement is isotropic, but the $\Sigma\eta$ enhancement is fit by a mixture of S and D waves.)

Some other isobars which can be intermediate states in η production are shown in Figure 1.1 (c). Of these, contribution of the $D_{13}(1525)$ resonance would be suppressed by the angular momentum barrier. (A recently reported[11] slight peaking of the cross section in the forward and backward directions at about 800 MeV may be due to this resonance.) The $F_{15}(1688)$ resonance has already been shown to contribute very little to this production process.[12] Other resonances may become important at higher energies.

Attempts have been made to fit the eta production cross section with various models, especially near threshold. The enhancement observed in both photoproduction and pion production is difficult to fit because of its rapid energy variation. One of the purposes of our experiment was to provide a set of points with good statistics in the falling region of the cross section to help delineate this feature; the existing data contain large error bars in the region of particular interest.

Another aim of the present effort was to examine the angular dependence of the cross section in a limited way up to about 1100 MeV.

Finally, nothing was known about the cross section above 1100 MeV, with the exception of one preliminary bubble chamber measurement[13] of the total cross section indicating that it was very small. This was surprising, since the cross section in pion production of etas, which exhibited the same qualitative features as the photoproduction cross section, fell off very slowly up to an energy equivalent to about 1500 MeV. Therefore, the third objective of our experiment was to get good data at energies as high as we could obtain at the 1.5 GeV Caltech synchrotron.

II. EXPERIMENTAL METHOD

In this experiment we wished to study the reaction

$$\gamma + p \rightarrow p + \eta$$

at incident photon energies up to the maximum available from the Caltech Synchrotron, 1.5 GeV. Before we began our experiments, the cross section for this reaction had been measured by various groups at several angles, and at incident photon energies from threshold (710 MeV) to about 1000 MeV.[6,14-16] These groups had employed two different detection schemes. In the first, the recoil proton was detected in a spectrometer and a step in the counting rate was observed as the endpoint energy was increased. In the second, one forward-going photon from various decay modes of the eta (as well as numerous background processes) was detected in coincidence with the recoil proton. Both of these methods involved a large background subtraction to convert raw data into cross sections.

The results obtained in these experiments show that the cross section rises rapidly above threshold to a maximum of about 1 μb/ster and then falls to about 0.2 μb/ster at about 1000 MeV. This cross section is already quite small compared to those of competing processes, and we wished to be able to measure precisely cross sections which might be even smaller. Therefore,

our experimental method had to be chosen to maximize the event rate for the reaction of interest and at the same time to facilitate the rejection of background processes. Our solution was to observe the production reaction via the two-gamma decay mode of the eta meson. This is the only two particle decay mode of the eta; the two photons and the recoil proton are the only particles in the final state, making feasible electronic detection, with reasonable efficiency, of all the reaction products. Furthermore, the branching ratio of this mode is relatively large (about 41%), and larger than that of any other decay.[4]

Thus, the process observed was

$$\gamma + p \rightarrow p + \eta \quad (\eta \rightarrow \gamma\gamma)$$

In the first experiment done by our group,[17] we measured a cross section of 0.2 μb/ster in the region of the third nucleon resonance and succeeded in reducing the background contamination to about 50% of the foreground.

At the time that the present experiment began, preliminary bubble chamber data[13] indicated that the total cross section dropped off drastically above 1100 MeV. (This result changed after a complete analysis.) By this time we had modified our apparatus so as to increase our detection efficiency by an order of

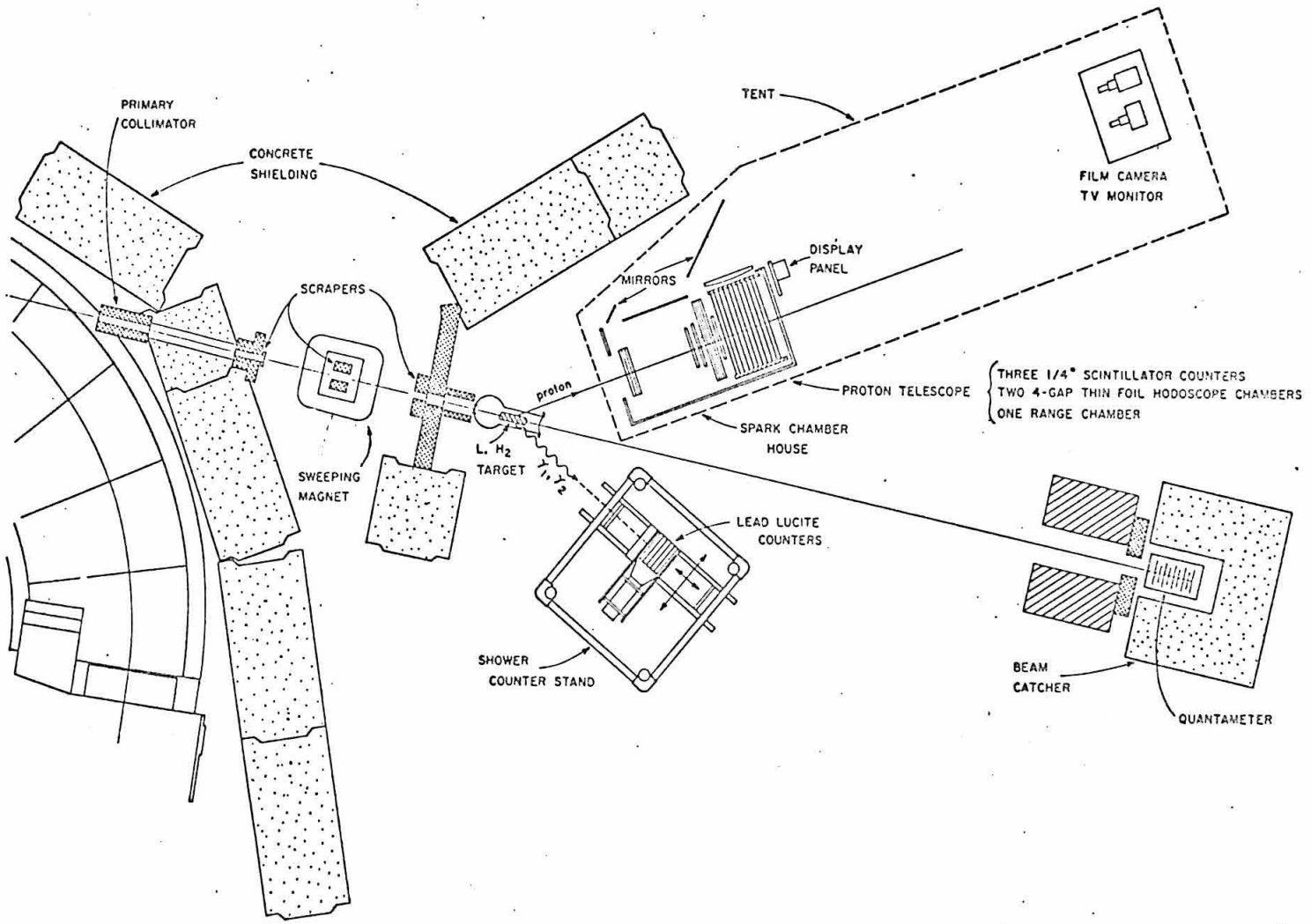

Figure 2.1 General experimental layout

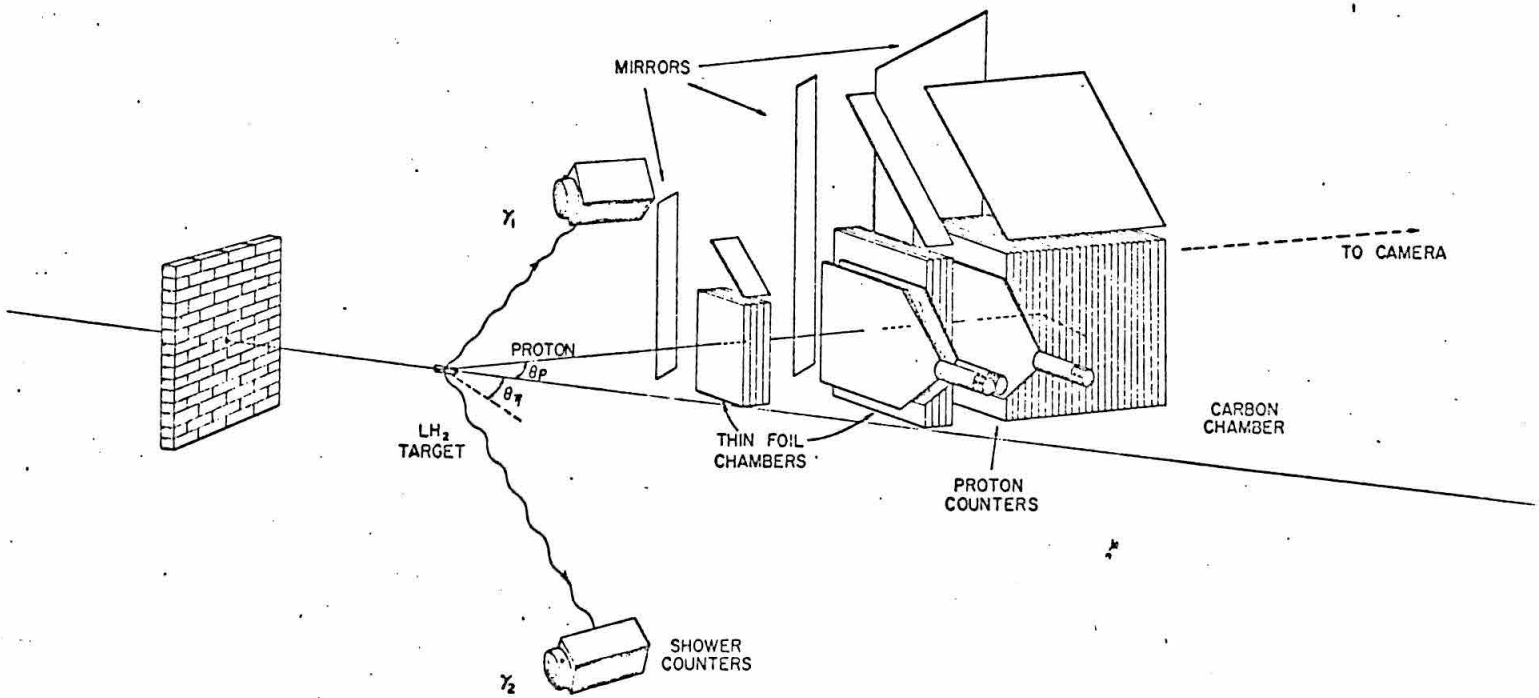

EXPERIMENTAL SETUP

Figure 2.2

magnitude, and at the same time to decrease the fraction of background contamination by about a factor of three. This was done by moving our counters closer to the target, and by adding extra counters, as we will show later. We were thus prepared to detect cross sections as low as about 0.02 μb/ster.

The general experimental area is shown in Figure 2.1; the main features of our own apparatus can be seen more clearly in Figure 2.2. The photon beam was produced when electrons of energy E_o, circulating in the synchrotron ring, struck a tantalum target and underwent bremsstrahlung. The beam emerged continuously and uniformly for about 150 milliseconds during each one-second acceleration cycle. The collimated beam passed between the poles of a sweeping magnet, then through the hydrogen target, and finally stopped and was monitored in a quantameter. (The photon beam is described in detail in Appendix VI. 1 , the hydrogen target in Appendix VI. 3 , and the beam monitoring in Appendix VI. 2 .)

We detected the recoil proton in a telescope consisting of three scintillation counters and three spark chambers. This telescope is described in detail in Appendix VI. 5 , along with the fiducial system and optics. The signature of a proton was a coincidence among all three counters. The biases on these counters

were set so that protons associated with etas would always be detected in each counter, while pions and electrons, which deposited less energy in the counters, would tend to pass through the system undetected. The two chambers closest to the target were made of thin aluminum foil sheets, and were used to measure the trajectory of the proton; the third chamber contained carbon plates, and was used to measure the range, and thus the energy of the protons.

In addition to absorbing energy, the carbon plates could be used to provide information about the polarization of the final proton in the reaction. When a polarized proton interacts with a nucleus, the proton tends to scatter preferentially to one side in a plane perpendicular to the polarization vector, due to L·S coupling effects. The extent of this asymmetry for a fully polarized proton beam, called the analyzing power, is for a given material, a function of proton energy and scattering angle, and is well measured for carbon. Thus, events in which scatters occurred could give us information about the proton polarization. (This analysis is not included in this thesis; a complete experiment to measure the polarization with good statistics is now in progress.)

On the opposite side of the beam from the proton telescope, we placed two essentially identical counter

assemblies, each to detect one of the two photons from the eta decay. These assemblies are described in detail in Appendix VI. 4 . Briefly, each consisted of the following elements: a pair of scintillation counters, run in veto, to reject initially charged particles; two radiation lengths of lead, to convert most of the photons into charged particles; a grid of partially overlapped scintillation counters called the horizontal and vertical hodoscopes, which divided the 6" x 10" aperture into 63 equal rectangular regions, 9 across and 7 down, to localize the shower; and finally a shower counter of alternate plates of lucite and lead, with five radiation lengths of lead in all, and with the lucite sheets connected via a light pipe to a single 5" phototube. The horizontal hodoscopes were a new feature of this experiment, and led directly to the large reduction of background contamination mentioned earlier. The shower counter was only sensitive to charged particles whose velocity was greater than 0.7c, the Čerenkov threshold in lucite. A photon or electron of sufficiently high energy to shower appreciably would produce several such particles (electrons and positrons), and would therefore generate more light in the counter than would a single non-showering particle, such as a pion.

The signature of a photon, then, consisted of the following elements, all in coincidence: a signal from

the shower counter above a certain bias, a count in at least one horizontal and one vertical hodoscope, and no count in the veto counters. The coincidence of a photon in each detector was required to generate the "gamma" signal.

The two gamma detectors were placed symmetrically above and below the average production plane, which was horizontal. Thus, we observed eta decays close to symmetrical, that is, those in which both decay photons made approximately the same angle with the eta direction. This is the most efficient way to detect the decay, for two reasons: First, the effective solid angle for simultaneously detecting the two photons is largest in this configuration. Secondly, the symmetrical decay yields photons of equal energy, while in any other decay, the more backward-going photon is less energetic. This further decreases the overall detection efficiency, since the sensitivity of the gamma detector starts to decrease below a certain energy. (See Appendix VI.4.) Since the eta has no spin, its decay is isotropic in the center of mass, and the fact that we are not sensitive to decays over the entire sphere presents no difficulty.

The proton trajectory and the beam line defined the production plane and origin for each event. This origin and the hodoscope grids on each gamma counter defined the

plane of the eta decay. The intersection of these two planes defined the eta trajectory, and thus the angles between the eta and both decay photons. The eta decay plane was chosen perpendicular to the production plane so that the eta trajectory would be determined as accurately as possible. Had any other decay plane been chosen, the determination of the eta trajectory would have been less accurate; in the extreme case in which the decay is observed in the production plane almost nothing can be deduced about the eta trajectory, unless the photon energies be measured very precisely.

The primary data of the experiment consisted of the photographed record of the events. A typical picture is shown in Figure 2.3. When the logic perceived an event, that is, a coincidence between a "gamma" signal and a "proton" signal, the spark chambers were fired to make the proton track visible. A camera which viewed the spark chambers by mirrors from the side and from above photographed the tracks. Next, fiducial marks were illuminated, so that the observed tracks could be related to the laboratory frame, and lights on a data panel were flashed which indicated the event number and the kinematical information from the eta side, e.g., the pulse heights in the two shower counters, and the elements in the hodoscope grids which were involved in the event.

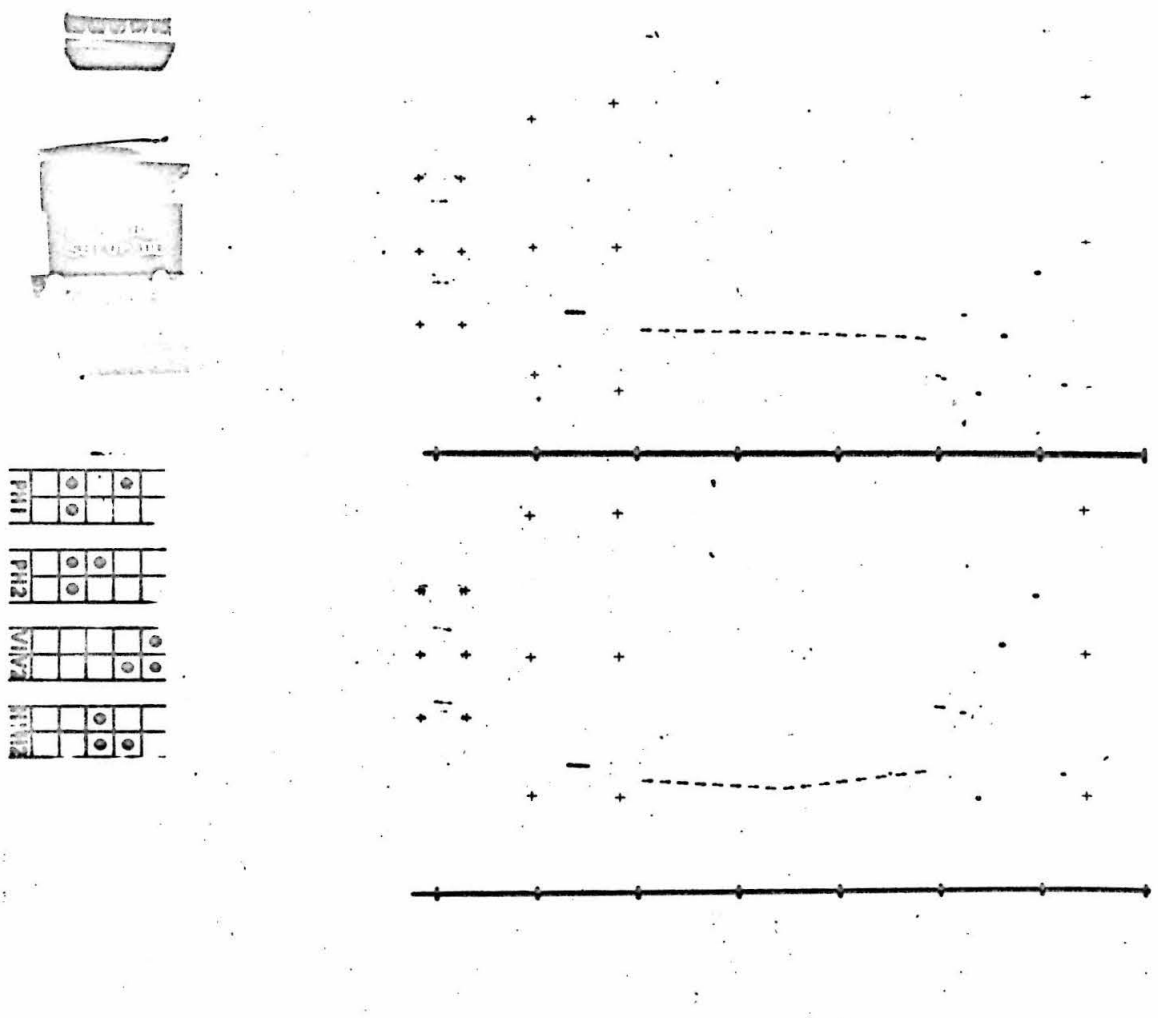

Figure 2.3 Typical event picture (shown in negative)

The film was then advanced and the camera awaited the next event. In this way 46,000 events, at five kinematical settings, were collected. Table 2.1 shows the kinematical parameters for the five settings. In addition to these filmed data, we kept records of the counting rates of every important counter in the experiment, and of the coincidence rates at each level of the logic. Daily tabulation of these rates provided a very sensitive monitor of the state of the apparatus.

It is instructive to examine the kinematic quantities measured in this experiment, with respect to the total available in order to completely specify the reaction. We assume that we have photoproduced a meson of unknown mass which decays into two photons. This gives us five particles in all, a photon and a proton in the incoming state, and a proton and two photons in the outgoing state. Each is specified kinematically by the four components of a relativistic momentum, so that the reaction yields 20 numbers which may be determined. Within experimental resolution, 17 kinematic quantities are known or directly measured, as follows: the mass of the incoming photon is known, and its direction is determined by the beam collimation (3); the target is known to be a proton at rest (4); the final charged particle is determined to be a proton by the trigger

TABLE 2.1

KINEMATICAL PARAMETERS

Setup	$\langle k \rangle$	$\langle \theta^*_\eta \rangle$	θ°_p	θ°_η	$\theta^\circ_{\gamma\gamma/2}$	D_1	D_2	E_o	BIP's
	Mev	deg	deg	deg	deg	cm	cm	MeV	$\times 10^3$
I	1200	50	43.5	22.8	30.6	173.9	92.9	1370	53.5
II	1000	50	36.9	24.8	36.9	173.0	94.8	1193	25.7
III	850	70	28.6	30.7	49.0	209.7	91.8	995	23.0
IV	1000	90	30.7	42.3	45.6	181.2	85.6	1193	26.0
V	1350	50	48.6	22.5	27.0	190.1	82.5	1472	15.5

$\langle k \rangle$ and $\langle \theta^*_\eta \rangle$ are the nominal photon energy and center-of-mass production angle for each setting. θ°_p, θ°_η, and $\theta^\circ_{\gamma\gamma}$ are the central values of the laboratory proton angle, eta angle and photon opening angle. D_1 and D_2 are the distances to the solid-angle-defining counters on the proton and eta sides, respectively. E_o is the end point energy of the synchrotron.

One BIP is typically 1.12×10^{13} MeV of integrated beam energy.

conditions, and its direction and energy are measured in the spark chambers (4); and each final photon is determined by the trigger conditions, and its direction is measured by the hodoscope grid (2 × 3) -- giving 17. Four-momentum conservation gives us four relations among the numbers, so that the three numbers not measured, say the energies of the incoming and outgoing photons, may be calculated, determining the reaction kinematics entirely, including the mass of the meson. The remaining relation contains no unknown parameters, and may be used as a test of the validity of the mechanism assumed.

In practice, we take the mass of the eta to be known for part of the calculation. Then we have two constraints to be satisfied among the measured quantities. If the reaction proceeded as assumed, these two constraints will be satisfied to within experimental error. Background events, in which one or more of our assumptions is not true, will fail to satisfy the constraints, except possibly by accident. In addition, the pulse heights in the photon detectors, which give a rough measure of the photon energies, tend to be lower for background events than for actual eta events. These criteria allow us to reject most of our background, as will be seen in the next section.

III. DATA ANALYSIS

1. Scanning

The retrieval of data from the film proceeded in two stages, scanning and measuring.

All of the film was scanned twice, each time by different scanners. For each frame, the scanner recorded the event number and the information on the data panel, along with a coded description of the tracks in the spark chambers. He noted how many correlated sets of tracks existed, how far they penetrated into the range chamber, which, if any, scattered, etc.. Each event was recorded, even if no tracks were present. If the scanner could not classify an event for any reason, this fact was recorded and the event was re-examined later.

The information recorded by the scanners was punched onto IBM cards, one per event, and the two sets of cards were compared by computer. The computer generated a list of mismatches, which were "verified" by a third scanner, who arbitrated the disagreements. This process involved more than ten percent of the events. A fair fraction of the differences were due to errors in reading lights or in recording information. This is not too surprising, since from 10 to 18 numbers were recorded for each event. Thus if each scanner missed one number in 1000, about 3 percent of the events would show

disagreements. The remainder reflected either differences of opinion in marginal cases, or temporary lapses of consciousness. After verification, the scan cards were corrected, and these verified scan cards were used in all subsequent stages of the analysis.

As a check of the scanning system, 20 percent of the events were rescanned in blocks, with the personnel shuffled, and the results were compared with the original scans. The discrepancies were found to be quite small, and we are satisfied that essentially all the measurable events were found.

The verified scan cards were used in several ways. First, they yielded lists of events to be measured. For each type of event of interest, a simple computer program could be written to pick out all events of that type. Also, the scan cards allowed us to calculate corrections for events which could not be analyzed. An example of this kind of event is one with two complete proton tracks, or one in which more than one bin in a hodoscope array fired. Lastly, the cards supplied various numbers for the kinematic reduction. Since all the information on the scan cards was presumably correct, we decided that errors would be reduced if we took as many numbers as possible from the scan cards, and only the spark positions from the measuring. Enough information was recorded in measuring, however, to enable us

to be sure that the scan and measure cards for an event did, in fact, represent the same event.

2. Measuring

Most of the measuring was done on one measuring machine, in which the image of the film was projected from above onto a table looped by two wide mylar bands at right angles. The top band was transparent, and the bottom one was painted white, so that the image appeared between the two bands. Each band had a hairline scribed onto it, together forming a crosshair, whose intersection could be moved around the table by moving the bands over two sets of rollers. The rollers were attached to two digital encoders, which gave the coordinates of the crosshair. A touch of a foot pedal transferred the coordinates through an IBM key punch onto cards. In this experiment, a unit of table coordinate corresponded to about 0.2 millimeters in the laboratory, and typical measurement errors were one or two table units, which introduced negligible error in the analysis.

The measurement of an event consisted of punching several numbers (event number, data panel information, length of track in range chamber, etc.) onto the cards through thumbwheel switches, and then recording the coordinates of seven fiducial marks and five sparks in each view of the chambers. More than the minimum number

of fiducials and sparks were punched, so that errors could be detected.

We measured about 34,000 of the 46,000 photographed events. The events not measured were mainly those in which the proton did not penetrate into the range chamber, even though it did go through the three scintillators. The events were measured in several groups, for convenience and simplicity of interpretation. For example, events in which the proton underwent a scatter in the range chamber were measured separately.

3. Kinematical Reduction

As we noted before, the scan and measure cards were used together in the kinematical reduction. This procedure allowed us to keep track of events overlooked in the measuring, and also eliminated errors which would have occurred had the measurer recorded incorrect numbers.

The main steps in the reduction, along with typical uncertainties, are given below:

a) The table coordinates of the measured fiducials were fit to a master grid, by way of a transformation of coordinate system constrained only to preserve straight lines; the spark coordinates were adjusted accordingly. This transformation corrected for rotation and translation of the film in the frame holder, for changes in film size due to temperature and humidity effects, and finally,

for arbitrary misalignment of the mirrors in the projection system. Also, since there were more fiducials punched than parameters in the fit, the goodness of fit could be used to indicate if an error had occurred in the measuring. Any event with an unreasonably large χ^2 for the fit was remeasured and re-analyzed.

b) From the spark coordinates in both views of the two thin foil chambers, the trajectory of the proton was reconstructed, using the known positions of the fiducials in the laboratory. Effects of parallax and refraction through the lucite walls of the chamber were included. Here again, more sparks were measured than were needed to determine the trajectory, so a goodness of fit was calculated and some events were remeasured. The main uncertainty in the trajectory determination was due to multiple scattering of the proton, and varied from about 1° (root-mean-square projected) at the lowest proton energies, to about 0.2° at the highest. Errors due to the measurement and to optical distortions were negligible.

c) The trajectory was followed back to the target, and a most likely event origin was calculated. Here, the main uncertainty was due to the finite diameter of the target. The origin was chosen on the mid-point of the

intersection of the trajectory with the target. The typical uncertainty was about 1.5 centimeters along the trajectory, and a few tenths of a centimeter perpendicular to the trajectory (due to multiple scattering).

d) From the proton angles, the event origin, and the hodoscope information, the trajectories of the eta and the two decay photons were calculated. Each photon was assumed to have gone through the center of the bin (defined by the overlapping hodoscope grid) in which it was detected. This calculation also gave the velocity, β, of the eta. (For a symmetrical decay, $\beta = \cos\frac{\theta}{2}\gamma\gamma$, where $\theta_{\gamma\gamma}$ is the angle between the two photons.) The uncertainty in eta angle was about 1°, due jointly to the finite hodoscope bin size and the finite target size.

e) The proton energy was calculated from the range in the carbon plate chamber. Effects of non-normal incidence and of target origin were included. The relation between proton range and energy was got from a separate program which integrated the energy loss through the various materials in the proton path, using a theoretical expression for the ionization loss.[18] The results were fit to the form

$$\log T_p = \sum_{i=0}^{n} a_i \log(R + \Delta R)^i$$

where

T_p = the proton kinetic energy,

R = the residual range in the carbon chamber,

ΔR = the amount of material in front of the range chamber,

and a_i = an adjustable parameter.

This form was used because the range-energy relation is almost a power law, and a two parameter fit of this type was as good as a five parameter polynomial fit. For n = 3, the expression fit the calculated values to within 0.1 MeV for proton energies between 80 and 300 MeV. This fit was then used in the reduction program to give the energy of the proton. The uncertainty in proton energy was typically about 5 MeV, due to the finite carbon plate and hydrogen target size, and to a lesser extent, to range straggling of the proton.

f) The incoming photon energy, k, was calculated using the proton trajectory and energy, and assuming the mass of the eta. The resolution in k varied from 6 to 20 MeV, and came mostly from proton multiple scattering.

g) The mass of the eta, M_η, was calculated using the proton trajectory and energy, and the eta trajectory. The mass resolution varied from 10 to 20 MeV, depending on the setting, and came mostly from uncertainties in the proton energy and the eta trajectory. (This step is

independent of step f, in which the mass of the eta was assumed.)

h) A quantity ΔE_η was determined. It is the difference between calculated eta energies obtained two different ways using essentially independent information each time. The first comes from the production kinematics, involving the proton direction and energy and the inferred eta direction; the second comes from the decay kinematics, involving essentially the opening angle of the two photons. The resolution in this quantity was about 15 MeV, and was in general insensitive to uncertainties in the proton energy. (The two energies whose difference was taken were typically 800 MeV.)

i) All information relevant to the event was packed in code and punched onto a single IBM card. If the value of some quantity was widely outside the expected limits, so that no card could be punched, the program listed the event and all the quantities calculated to be examined later. All subsequent data analysis was performed using this punched output from the kinematical reduction.

4. Selection of Etas

Figure 3.1 is a dot plot of some events measured in a typical setup, with the calculated mass for each event

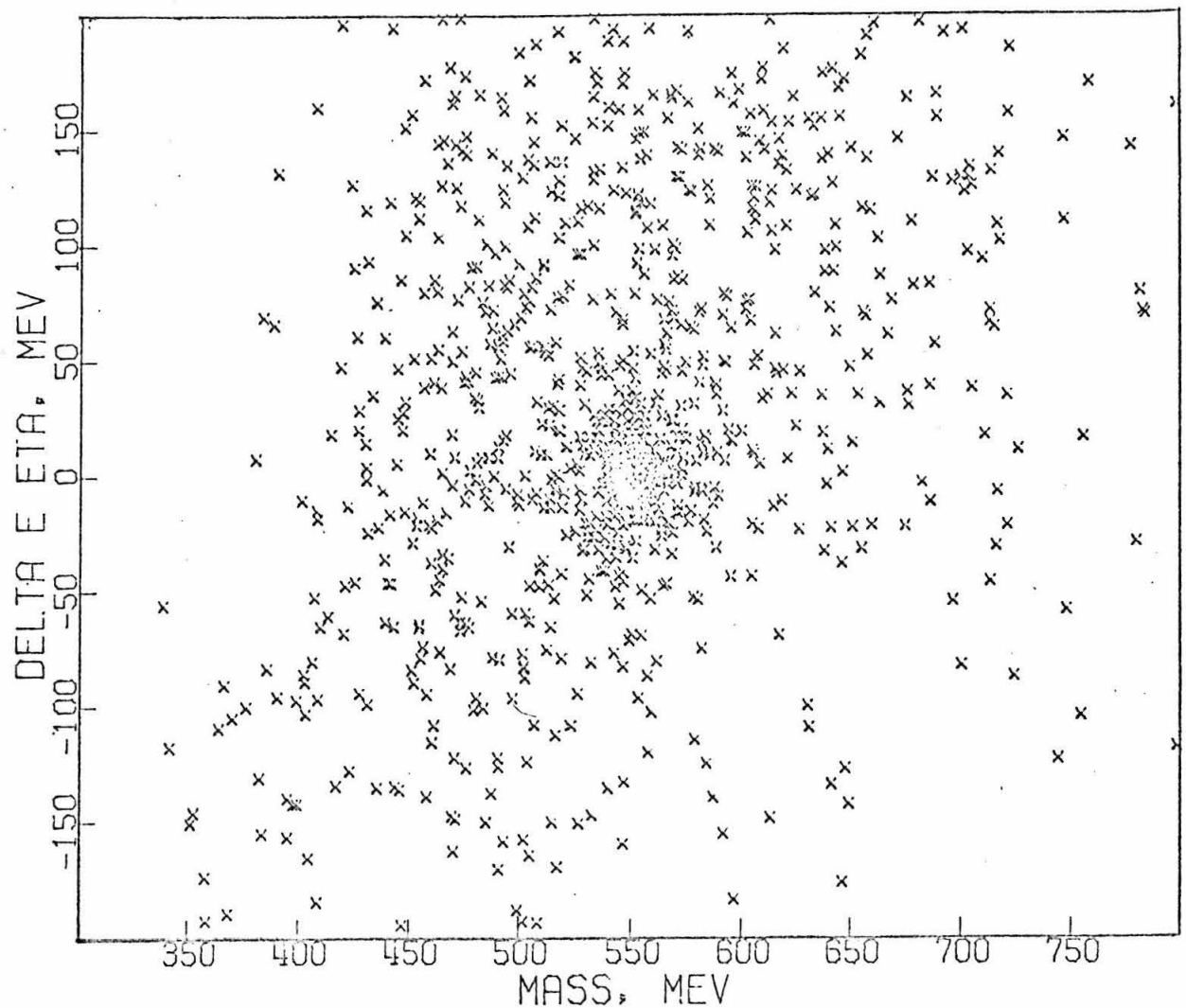

Figure 3.1 Mass vs. ΔE_η for events in a typical setting

as the abcissa and the value of ΔE_η as the ordinate. In this figure, and in succeeding ones, a low pulse height cutoff has been applied. Except for experimental resolution, any foreground event should have a mass of 549 MeV and ΔE_η equal to 0 MeV. The concentration of events around this point is quite striking. The rest of the events, including some under the eta peak, belong to the background, and must be eliminated before a cross section may be calculated.

Figure 3.2 shows projections of such a dot plot, but with many more events, onto the two axes. Again we see a pronounced peak where we expect etas, and a broad background under it.

In Figures 3.3 and 3.4, the projections are made from three bands of the dot plot. In both cases, the extreme bands show no eta peak, and the background in the central band is greatly reduced.

Figure 3.5 shows the distribution of projected origin for all the events measured, along the beam axis (z) and in the vertical plane of the target (x). (The third coordinate of the event origin was not determined in the experiment.) It will be seen that essentially all the events were confined to the dimensions of the target. The small number of events outside of the target appear because the scanners were not asked to

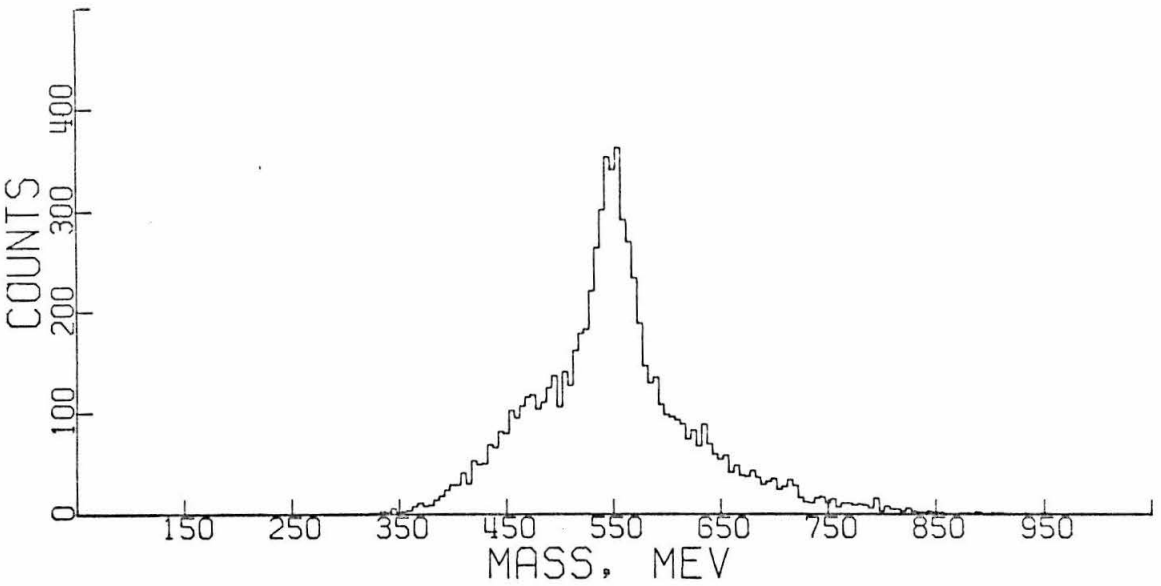

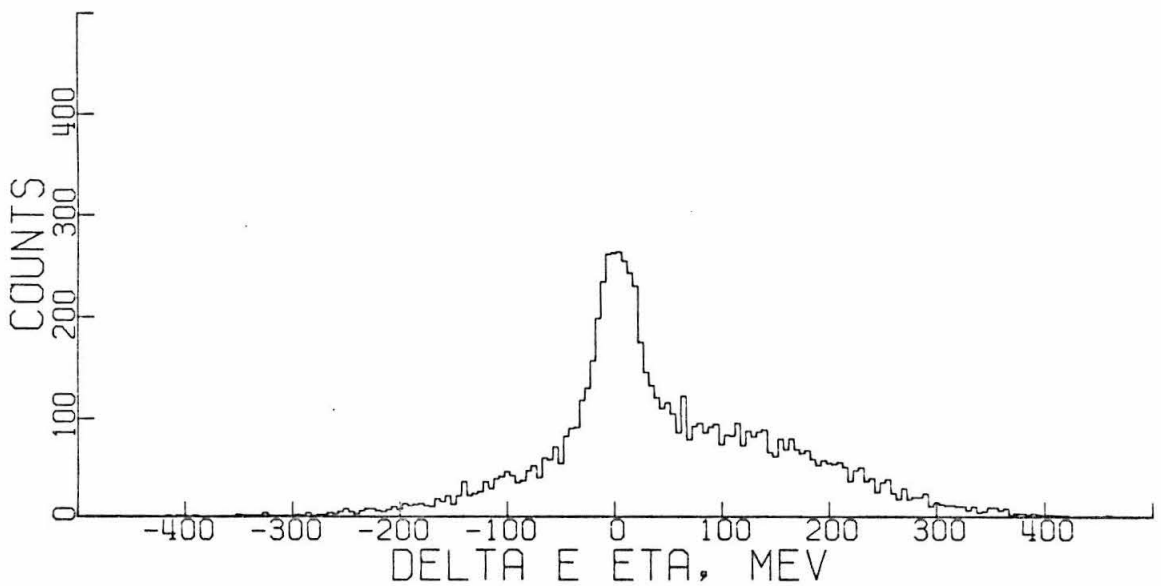

Figure 3.2 Projections of entire mass-ΔE_η plane onto two axes

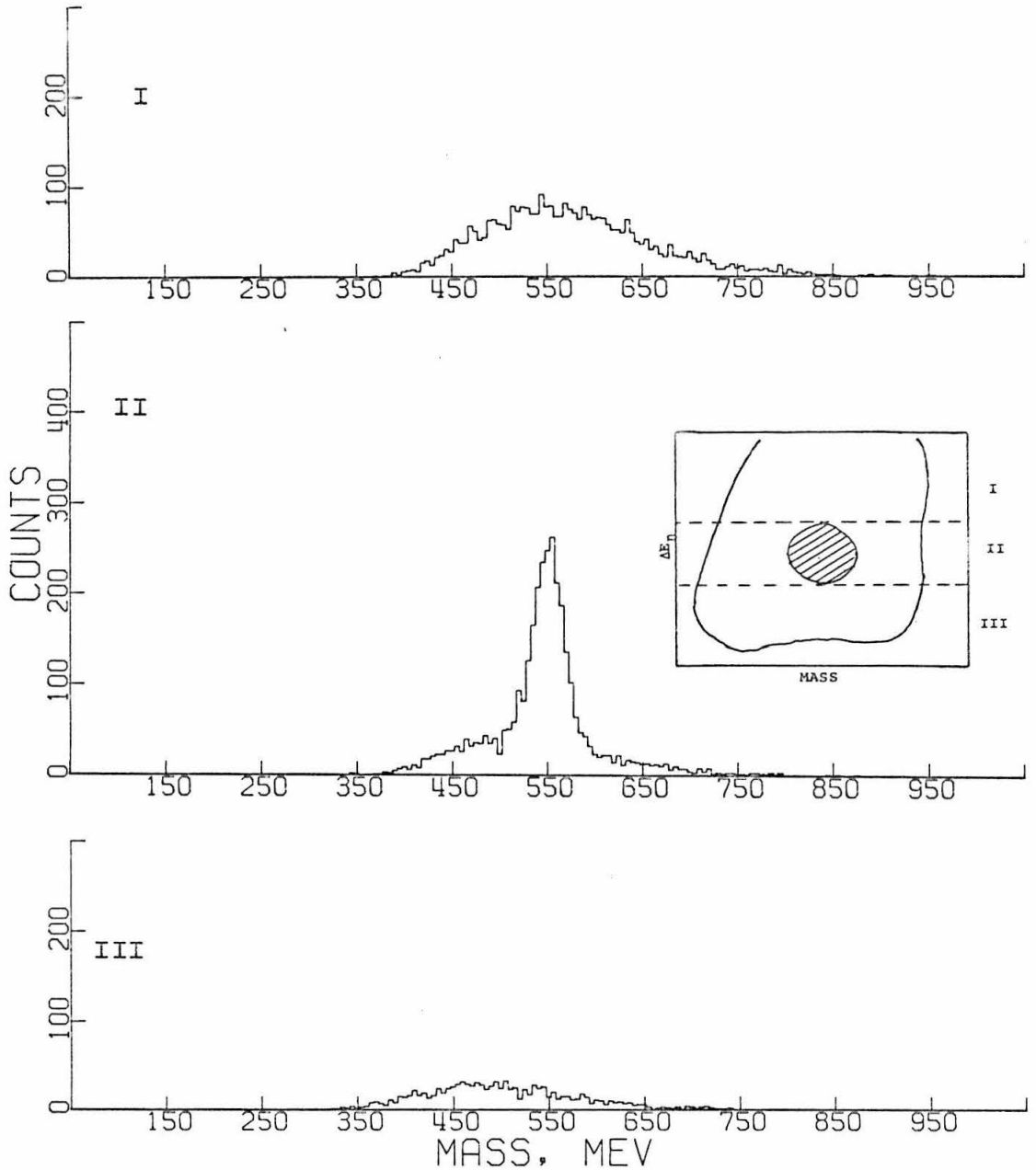

Figure 3.3 Projections of three bands in ΔE_η onto mass axis

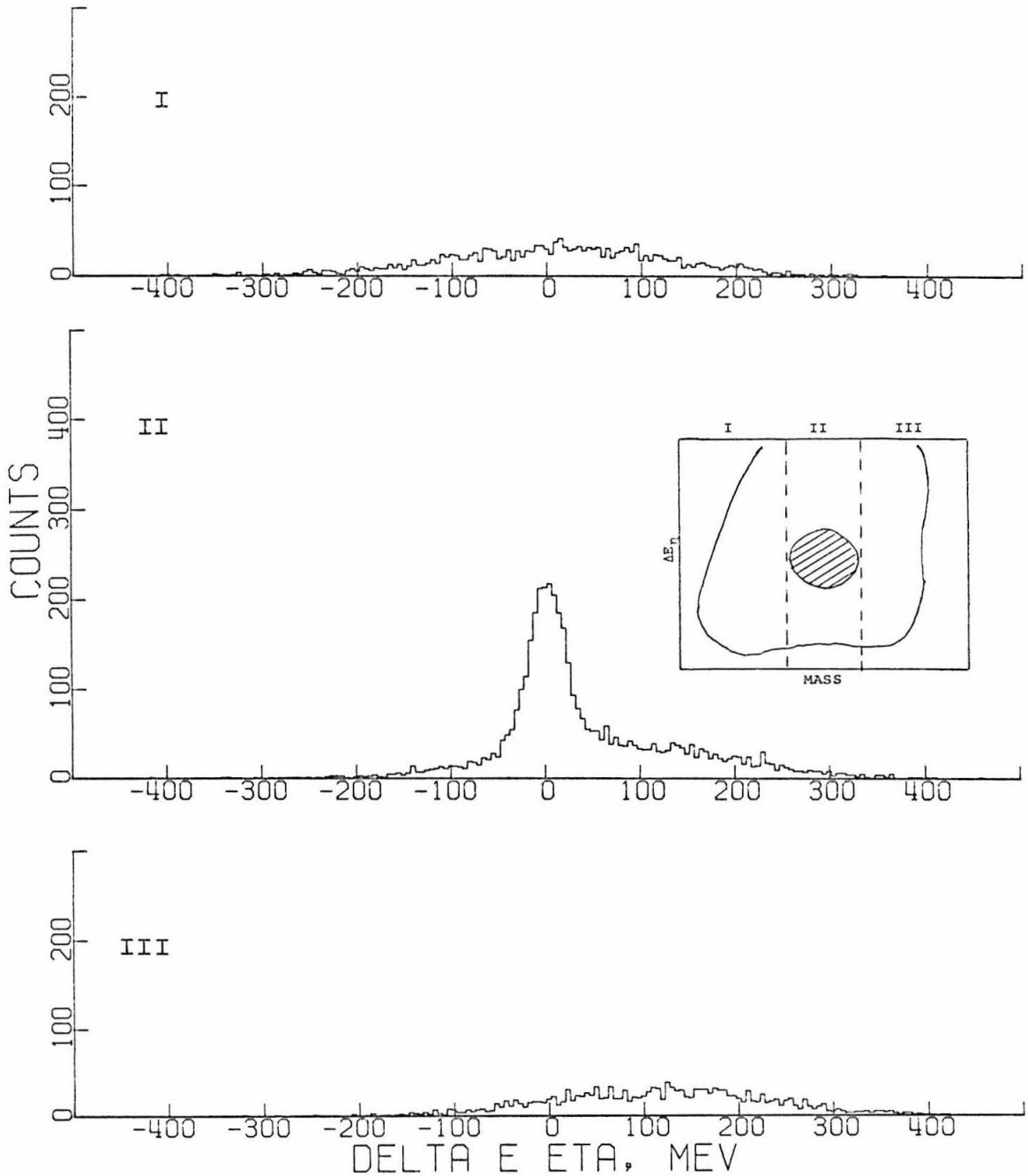

Figure 3.4 Projections of three bands in mass onto ΔE_η axis

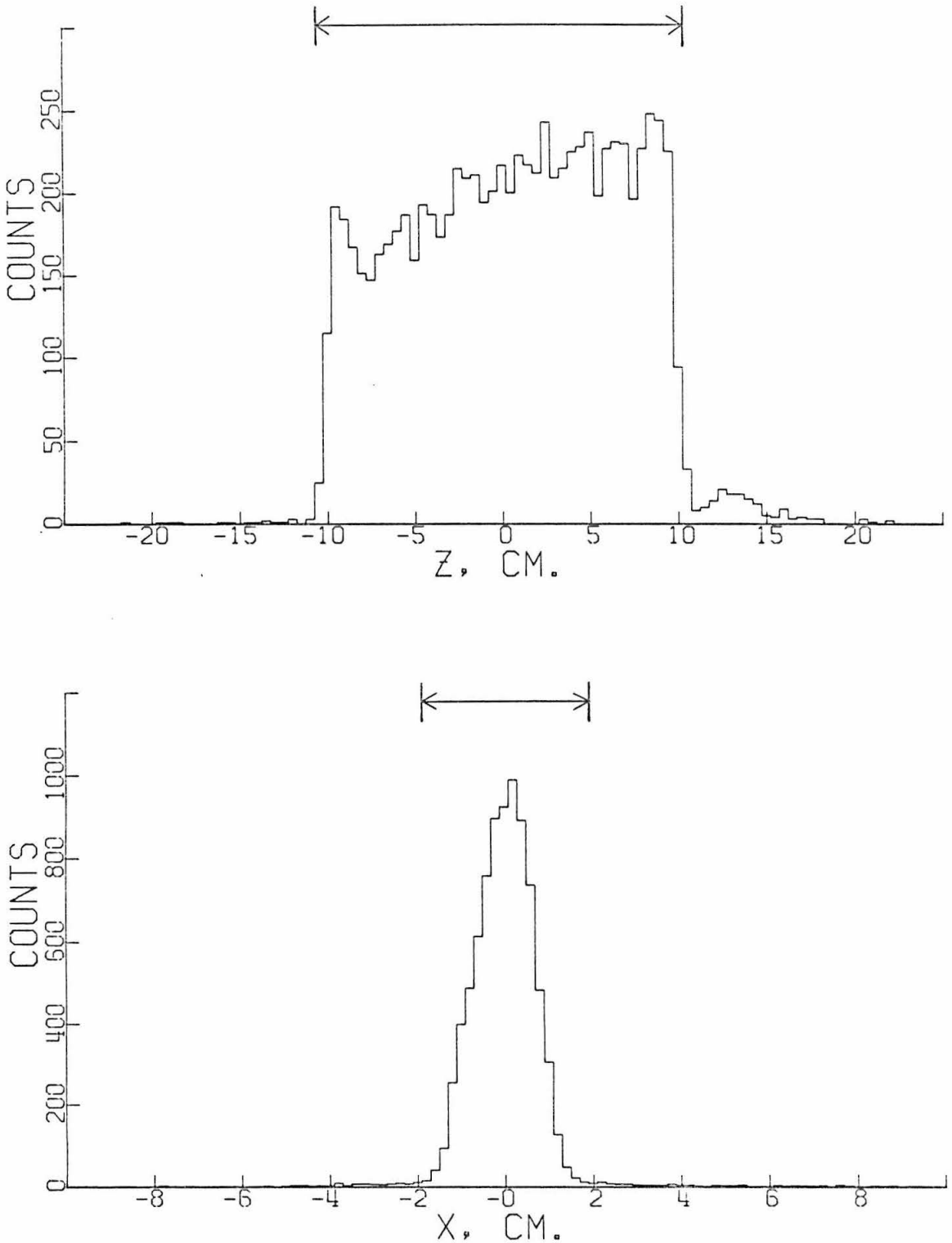

Figure 3.5 Distributions of calculated z and x event origins, showing length and diameter of target

decide whether an event seemed to originate from the target. The events outside the target were found in general not to satisfy eta kinematics, and represent accidental coincidences. The little bump at z = 12 cm is due to a 0.001" aluminum heat shield through which the beam passed. These events did not satisfy eta kinematics.

There were several marked differences between events under the eta peak, and those outside of it. The two most prominent ones can be seen in the pulse height distributions and in the distributions of range chamber penetration.

In Figure 3.6, we see a typical distribution of pulse heights in the two shower counters, and that of the summed pulse height, for events under the eta peak, and in Figure 3.7, for the rest of the events. It can readily be seen that the photons associated with the background events are, in general, of much lower energy than those of the foreground. (The energy of the photon is roughly proportional to its pulse height.) Also, in the summed pulse height for the eta events, the width of the distribution is somewhat narrower than expected from random correlation of pulse heights in the two counters. This is because the energies of the two photons are in fact correlated, so that their sum is

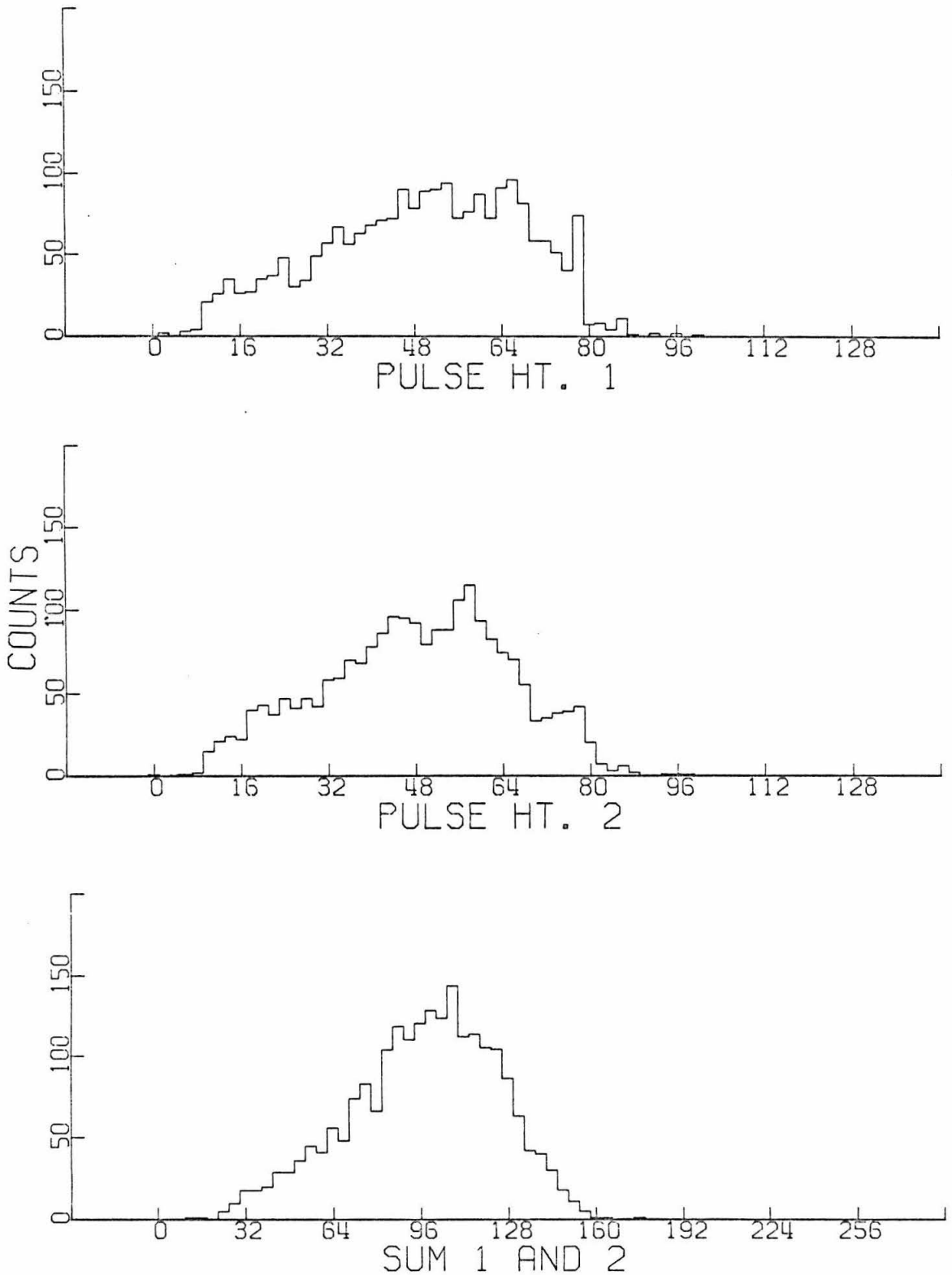

Figure 3.6 Distributions of pulse heights in both shower counters, and of the summed pulse heights, for events under the eta peak (includes 20% background events)

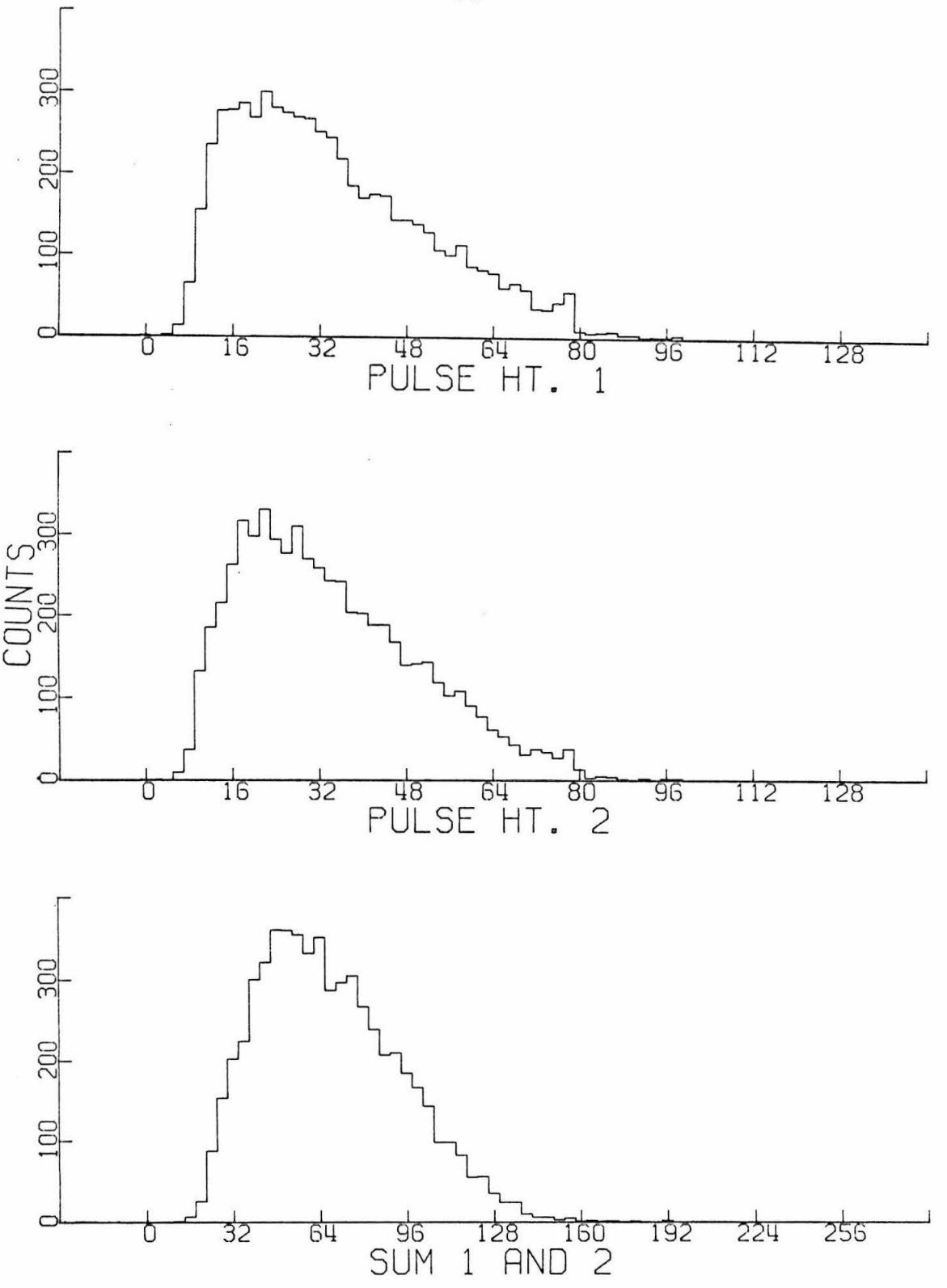

Figure 3.7 Distribution of pulse heights in both shower counters, and of the summed pulse heights, for background events

fairly constant for each setting. The background events do not exhibit this feature.

The distribution in range chamber penetration is shown in Figure 3.8, for etas and for background. We see that the background protons tend to concentrate in the first few modules, while the protons from eta production tend to peak in the center of the energy range.

Other features of the events, such as the distribution in proton angle and photon angles, also differ for etas and background, but these differences are not as striking as in the ones mentioned.

These differences can be exploited to obtain a pure sample of etas. Figure 3.9 shows the distribution of event masses for those events in the central band of Figure 3.3, in which the proton penetrated at least four modules, both pulse heights were greater than 20, and ΔE_η was between -25 MeV and +25 MeV. The height of the eta peak is reduced, but the background is eliminated almost entirely.

In the actual cross section analysis, the pulse height cutoff was set to be the same as the average for $\beta = 1$, non-showering particles, typically about 10. This was done for several reasons. First, the loss of etas was not severe at this point, so that the correction

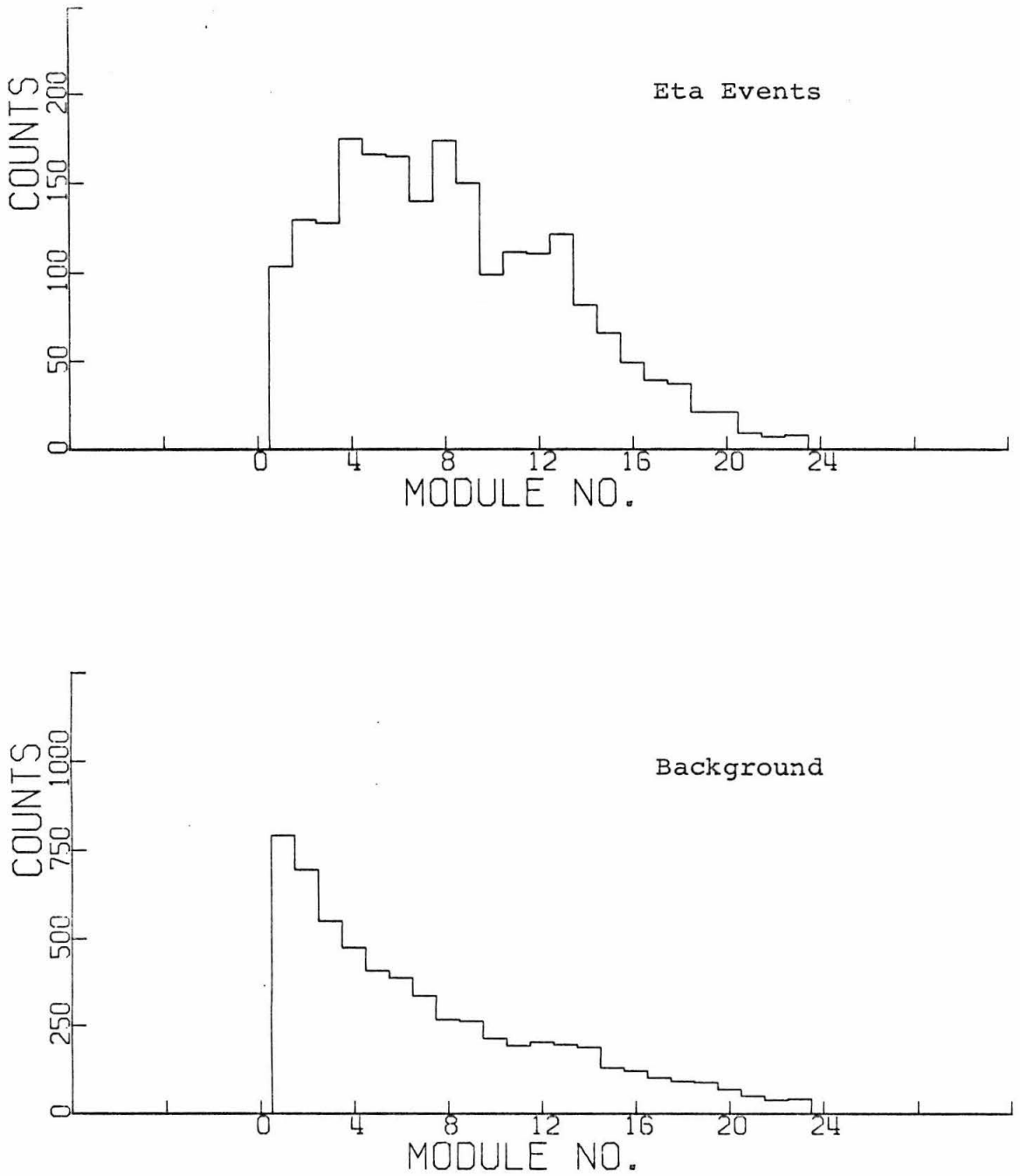

Figure 3.8 Distributions of range chamber penetration for eta events and for background

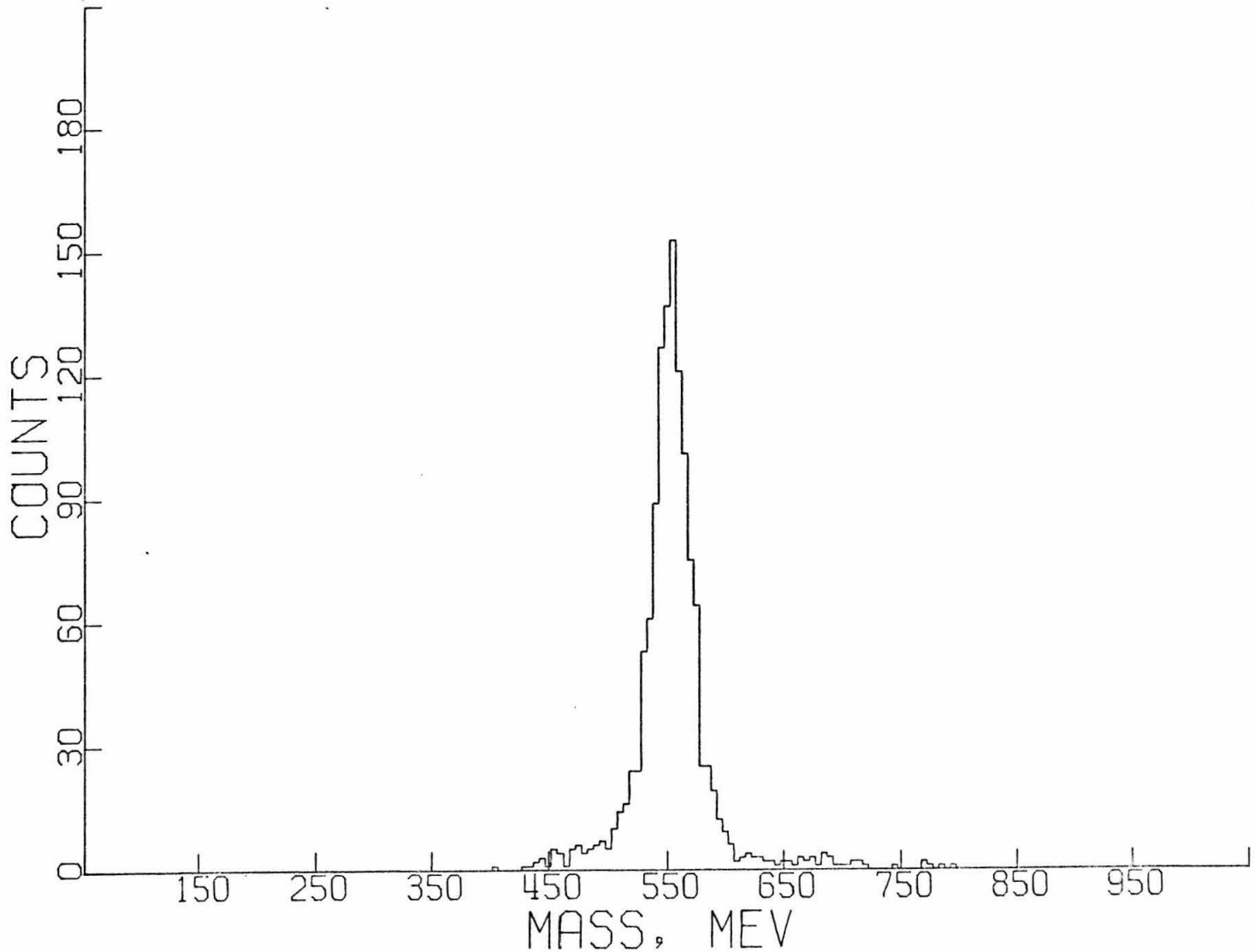

Figure 3.9 Mass distribution using limits which discriminate against background

was manageable, and secondly, this pulse height could be monitored during the running using the pion counters (Appendix VI. 4) independent of gain and pedestal drifts of the system.

5. Background Subtraction

Aside from accidental coincidences, of which there are not too many, the main contributions to the background are thought to come from

$$\gamma + p \rightarrow p + 2\pi^\circ \rightarrow 4\gamma$$

and

$$\gamma + p \rightarrow p + \eta \rightarrow 3\pi^\circ \rightarrow 6\gamma$$

The process

$$\gamma + p \rightarrow p + \pi^\circ \rightarrow 2\gamma$$

does not contribute to the background, because the typical opening angle between the decay photons is too small to be seen by our photon detection system. The other neutral decay mode of the eta, $\eta \rightarrow \pi^\circ \gamma\gamma$, is now thought to occur about 2% of the time, and is therefore not a significant source of background.[4]

The cross section for the first process is not known, but the $\pi^-\pi^+$ production cross section is in the vicinity of 45 μbarns.[19] Using this value, and

assuming a phase space distribution for the two pions, Prescott[20] showed that this process, with detection of one photon from each π°, accounted for about 80% of the background observed in his experiment, which had many features in common with the present one.

The second process has a cross section which is about twenty times smaller than $2\pi^\circ$ production. (Its cross section is known because it is measured in this experiment.) The reason that etas which decay through three π°'s appear as background, is that detection of two of the six photons produced eliminates essentially all kinematic constraints on the produced eta, so that neither the mass nor ΔE_η come out to be that of the eta. The detection of this process is helped by two factors: First, six photons, rather than four, are produced in the final state, so that there is a greater chance to detect two of them than in $2\pi^\circ$ production; secondly, the eta is already heading toward a point between the photon detectors, so that the detection efficiency is further increased. These two effects combine to increase the detection efficiency by about a factor of four, according to Prescott, and so this process accounts for the remaining 20% of the background.

From this discussion it is clear why the photons from background processes tend to have lower energies

than do those from etas. In the case of the background processes, the energy is shared among four or six photons, instead of two. In general, this means that the average photon energy is substantially decreased, even though we are more sensitive to those events in which two photons carry off most of the energy. Also, since we only see a part of the available photon energy, energy correlation between the two observed photons is not strong.

The problem in subtracting the background events in this experiment is twofold, and consists in determining the overall amount of background under the eta peak, and then in finding the distribution in the calculated incident photon energy k. This calculated energy is not the actual photon energy which produced the event, since the calculation assumes that an object of mass 549 MeV was produced, and the effective two-pion mass ranges from 270 MeV up to a maximum determined by the center of mass energy available.

It might be thought that once the total amount of background is determined, the k dependence of this background could be got from the background events outside of the peak. That this is not true can be seen by examining Figure 3.10. There we display the k distribution of background events taken from the

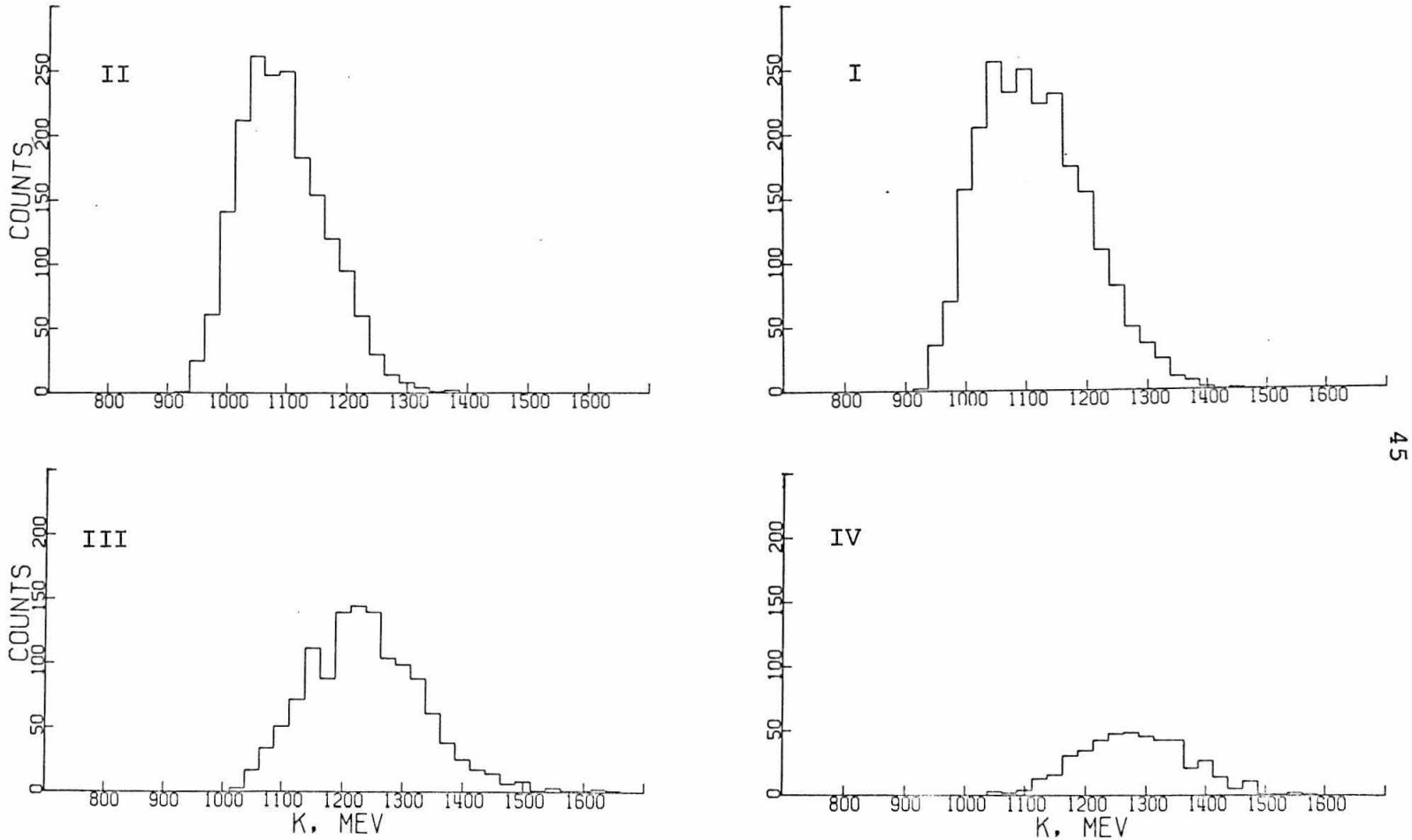

Figure 3.10 Distributions in k of events from the four quadrants of the mass-ΔE_η plane, excluding the eta peak

four quadrants of the mass-ΔE_η dot plot (Fig. 3.1), excluding the eta peak. It will been seen that the k distribution depends upon the position in the mass-ΔE_η plane. This should not be surprising, since, for example, there is a functional relationship among the eta mass, proton energy, proton angle, and k, so that a given eta mass will be correlated with some average k. A successful background calculation must reproduce this dependence, as well as the distribution of events in the mass-ΔE_η plane.

Rather than duplicate Prescott's calculation for our geometry, especially in view of the fact that no $2\pi^\circ$ data has become available, we decided to approach the problem from another direction.

Distributions were made of all the events occurring outside the eta peak, with respect to all the measured variables. The variables used were: the coordinates of the event origin; the range of the proton; the horizontal and vertical coordinates of the proton in the third counter in the proton telescope; and the horizontal and vertical coordinates of the photon in each photon detector (both were the same). The distribution of events in the y direction in the target was taken to be the same as that in the x direction. Then points were selected at random from each distribution and

combined to generate a simulated background event, which was punched out in the standard output card format. The process was repeated until sufficient events had been generated.

The basic assumption inherent in this procedure is that the measured variables were uncorrelated for the background processes in question. Thus, for example, the distribution of events in the photon hodoscope should not depend on the production angle of the proton associated with those events. It is reasonable that this should be so, because $2\pi^\circ$ decay kinematics send photons over a wide solid angle compared to that subtended by the detectors. Several sets of variables were checked pairwise for any correlation, and none was found, within statistics. In particular, the proton energy spectrum did not seem to depend on the proton lab angle.

We also tried to examine the distributions in the measured variables for those events under the eta peak. This can be done by looking at events under the peak with low pulse heights in the shower counters. The fraction of background events is thus enhanced, but their number is reduced. We found that for these events, the distributions did appear to be the same as for the other background events. However, the statistics were rather poor.

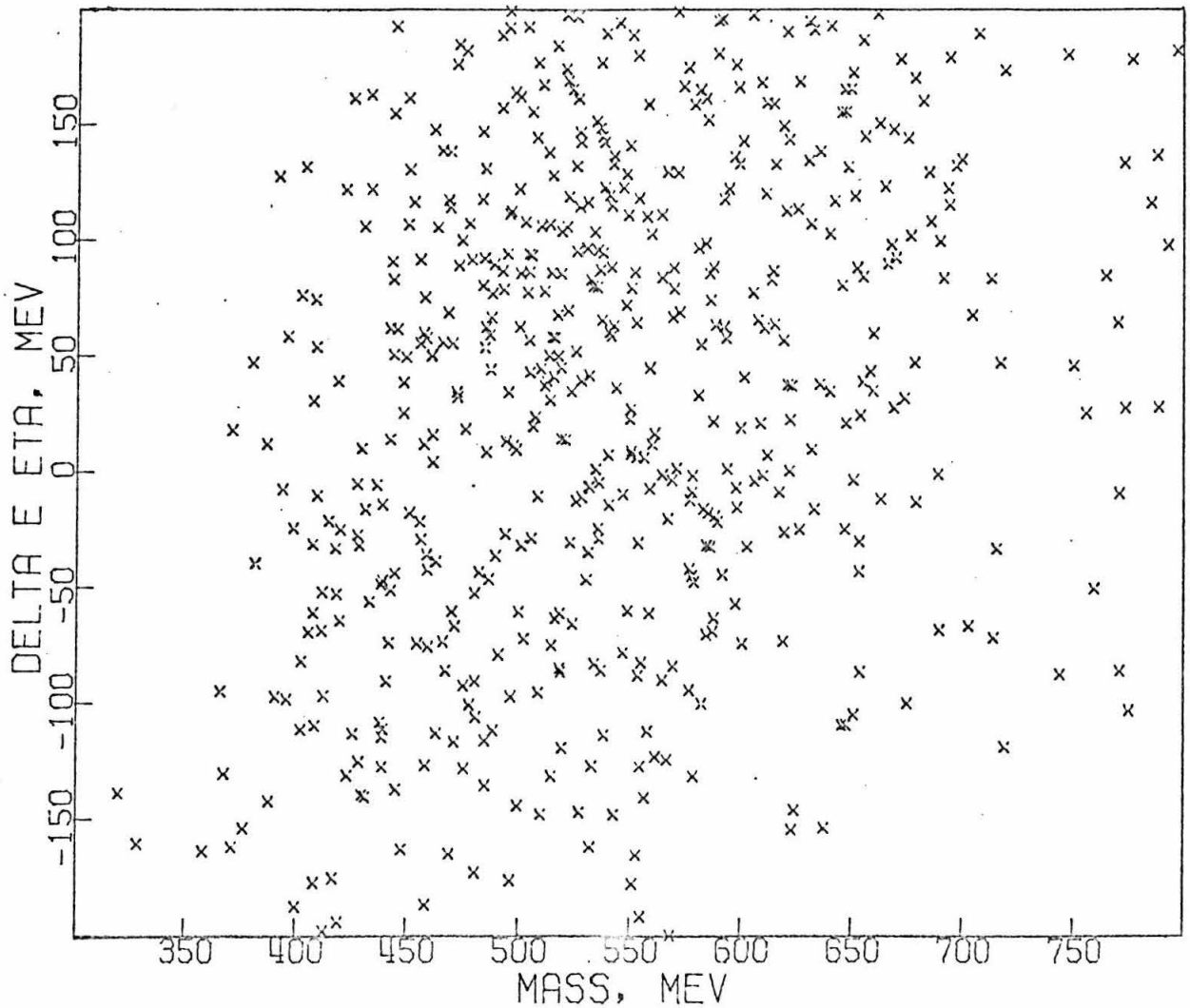

Figure 3.11 Mass vs. ΔE_η for simulated background events

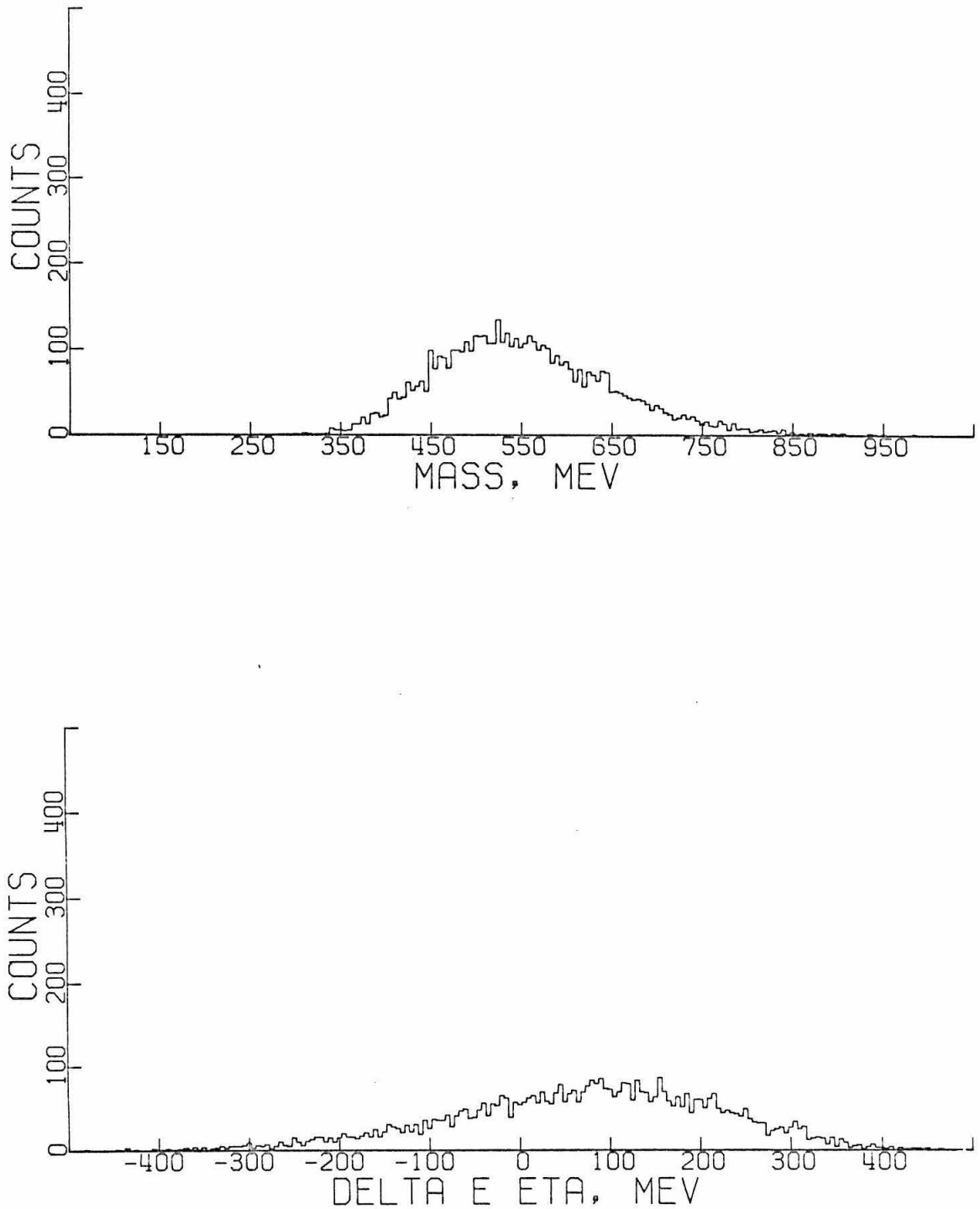

Figure 3.12 Projections of entire mass-ΔE_η plane onto two axes, for simulated background events

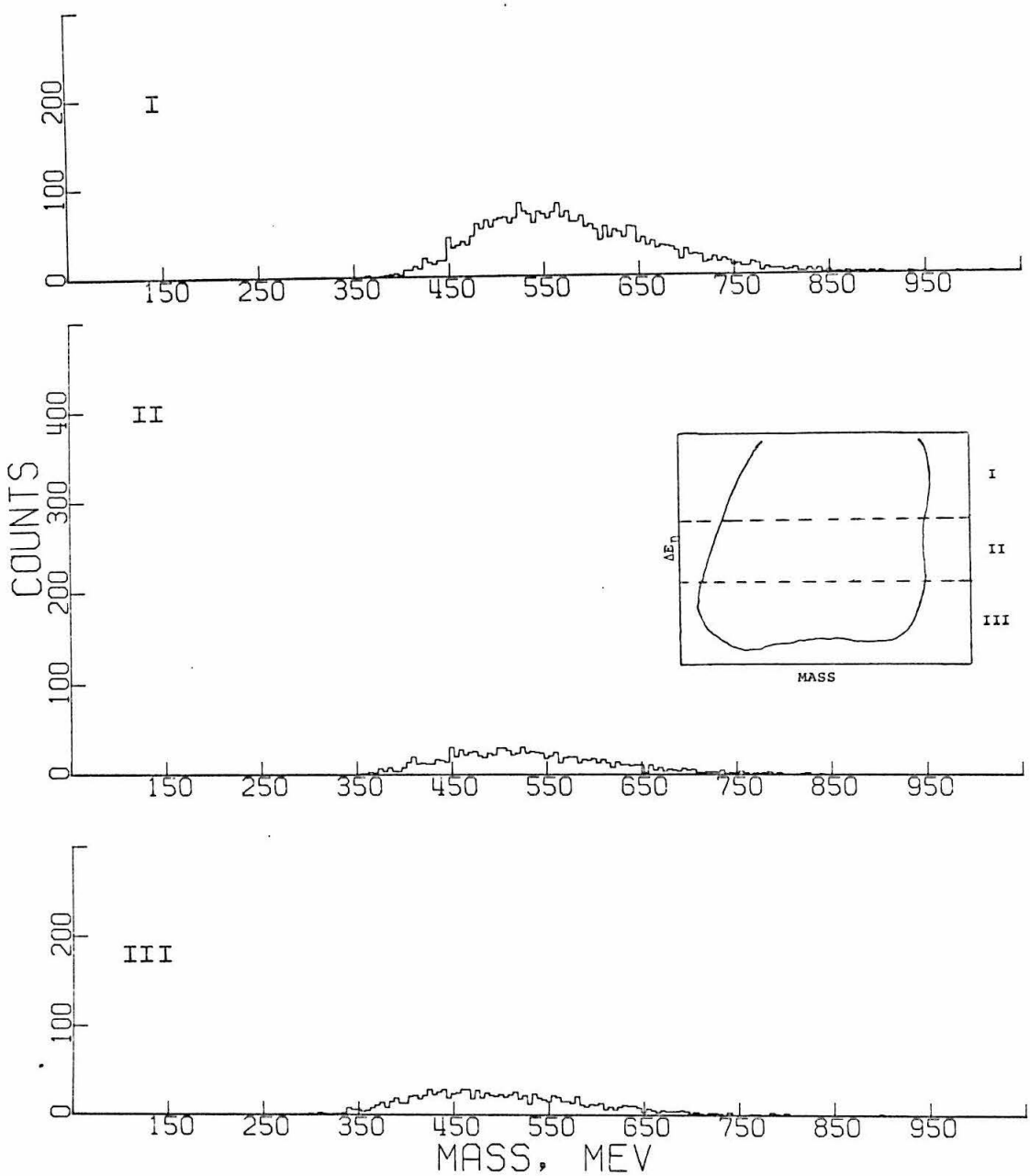

Figure 3.13 Projections of three bands of ΔE_n onto mass axis, for simulated background events

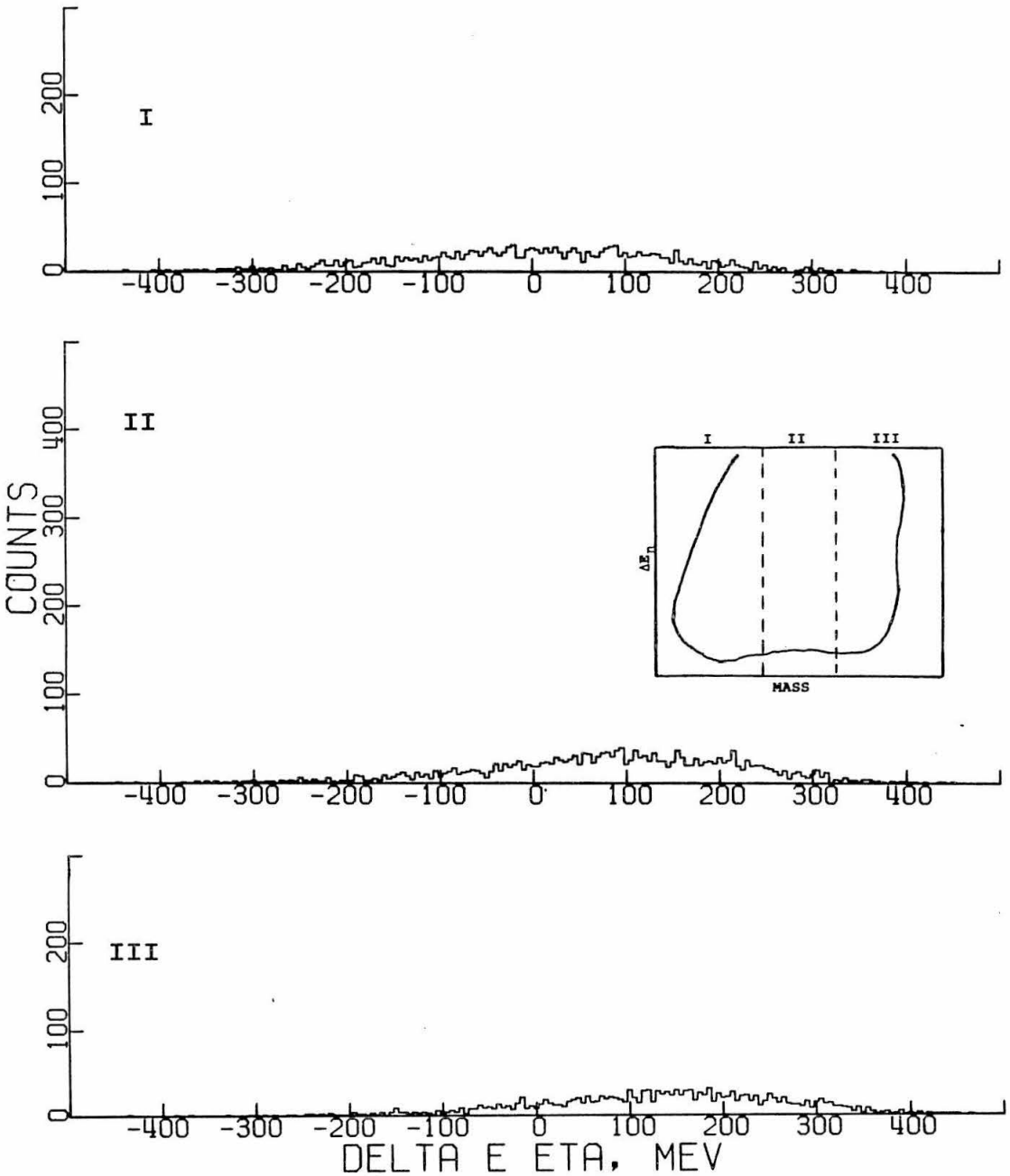

Figure 3.14 Projections of three bands of mass onto ΔE_η axis, for simulated background events

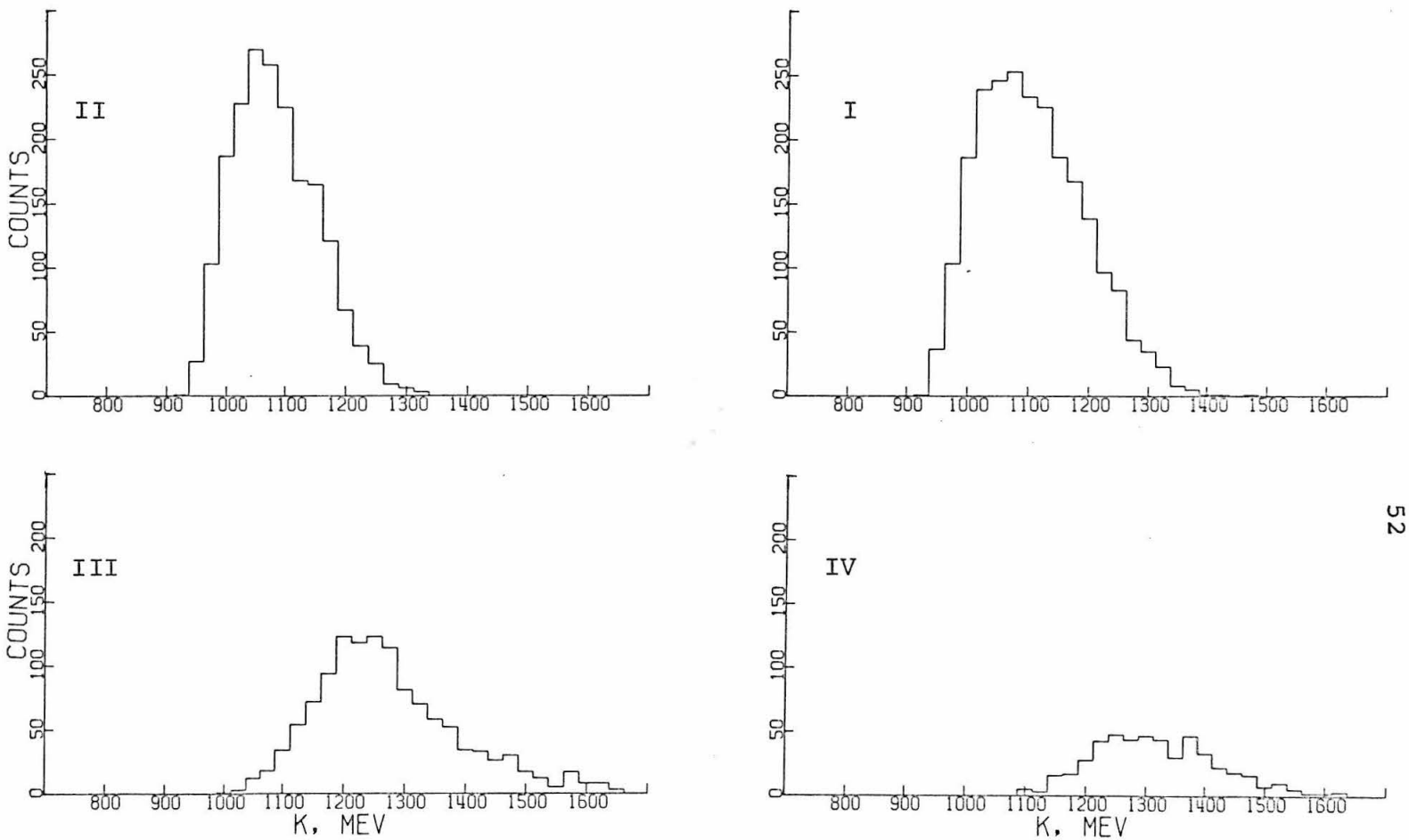

Figure 3.15 Distributions in k for events from the four quadrants of the mass-ΔE_n plane excluding the eta region, for the simulated background

The results of this calculation are displayed in the same way as in Figures 3.1 to 3.4 and Figure 3.10, and reference to these figures will allow a comparison of the real and simulated backgrounds.

Figure 3.11 is a dot plot of the simulated background events in the mass-ΔE_η plane. Figure 3.12 shows the projection of the dot plot onto the two axes. Note that the distribution does not peak in the eta region. (Compare to Figures 3.1 and 3.2.) Figures 3.13 and 3.14 show projections of bands in the mass-ΔE_η plane. (See Figures 3.3 and 3.4.) Figure 3.15 displays the k dependence for events in the four quadrants of the plane, excluding the area where the etas would be. (See Figure 3.10.) It can be seen from these figures that the background calculation indeed reproduces all the features of the real background everywhere that it can be tested.

Is it still possible that the model fails just under the peak, where we cannot see it? No, for the following reason. The minimum width of a bump or dip in the mass-ΔE_η plane is that of the eta peak, which comes from experimental dispersion of a single point in the plane. Any events with less correlation among the observed variables will lead to wider bumps, and our background, which is highly uncorrelated, has a typical

width of about 100 MeV, compared to 15 MeV for the foreground. Thus, any irregularity under the peak must spread out appreciably to where it becomes visible, conversely, the distributions which produce events near the peak will contribute events under the peak as well.

Figures 3.16 through 3.20 show the subtracted mass and ΔE_η distributions for each of the five kinematical settings of the experiment. In each case the only free parameter was the normalization, which was obtained from matching the calculated distribution to the experimental one for events outside the peak. For each, the number of events in the distribution is given, along with the number of events subtracted under the peak. It can be seen that the amount of background varied between 5% and 34% of the amount of foreground in the mass plot, depending on the setting. In general, the background production increases with energy, but kinematic factors also influence the background contamination through their effect on our resolution. Note that by sacrificing perhaps 20% to 30% of our eta counts, we could have decreased the fraction of background by almost a factor of two; we did not do this because the resulting corrections must be made quite carefully and also, because our background subtraction seemed to work well enough to make this improvement only marginally useful. The mass and ΔE_η subtractions were done

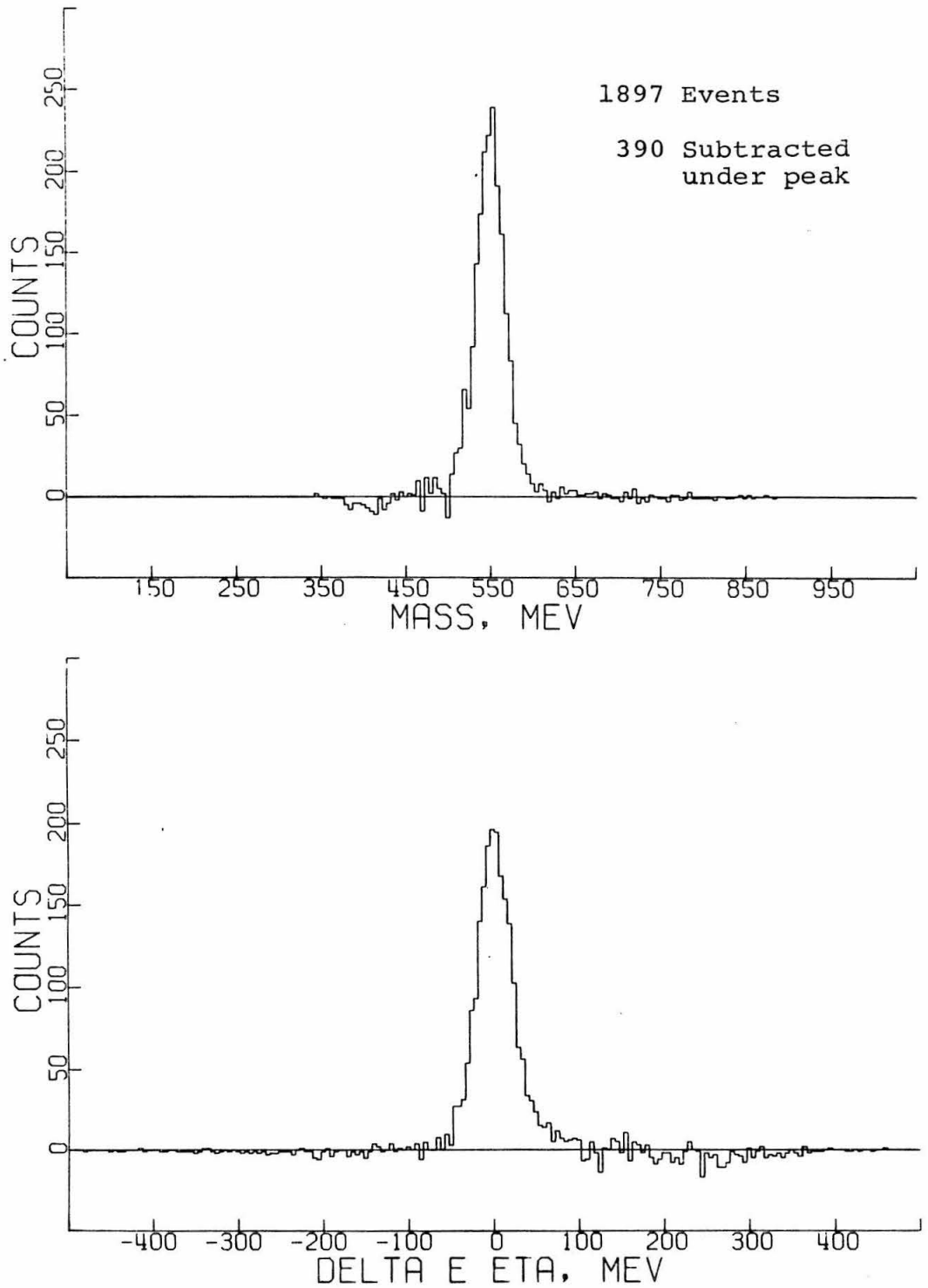

Figure 3.16 Subtracted mass and ΔE_η distributions for Setup I

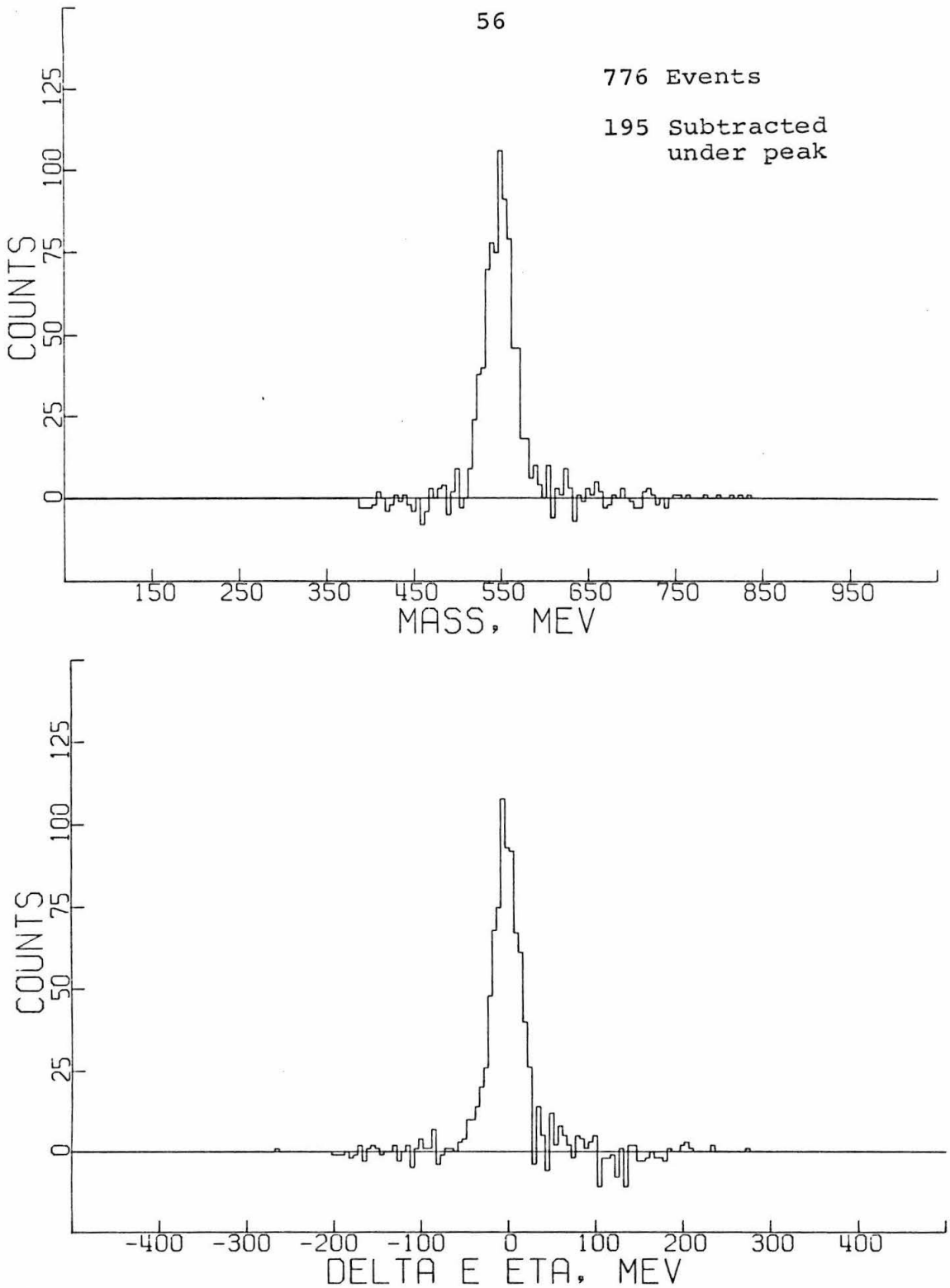

Figure 3.17 Subtracted mass and ΔE_η distributions for Setup II

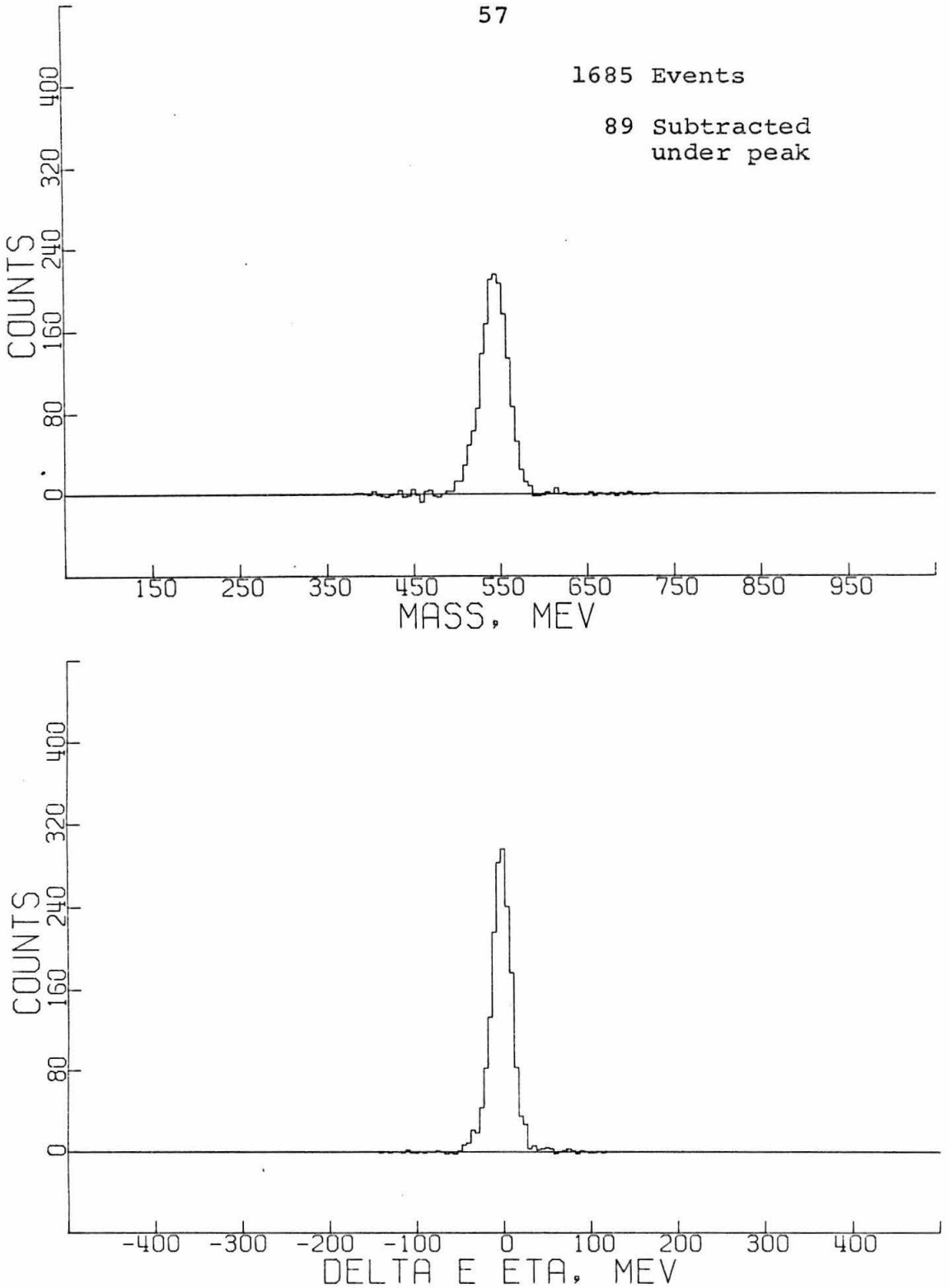

Figure 3.18 Subtracted mass and ΔE_η distributions for Setup III

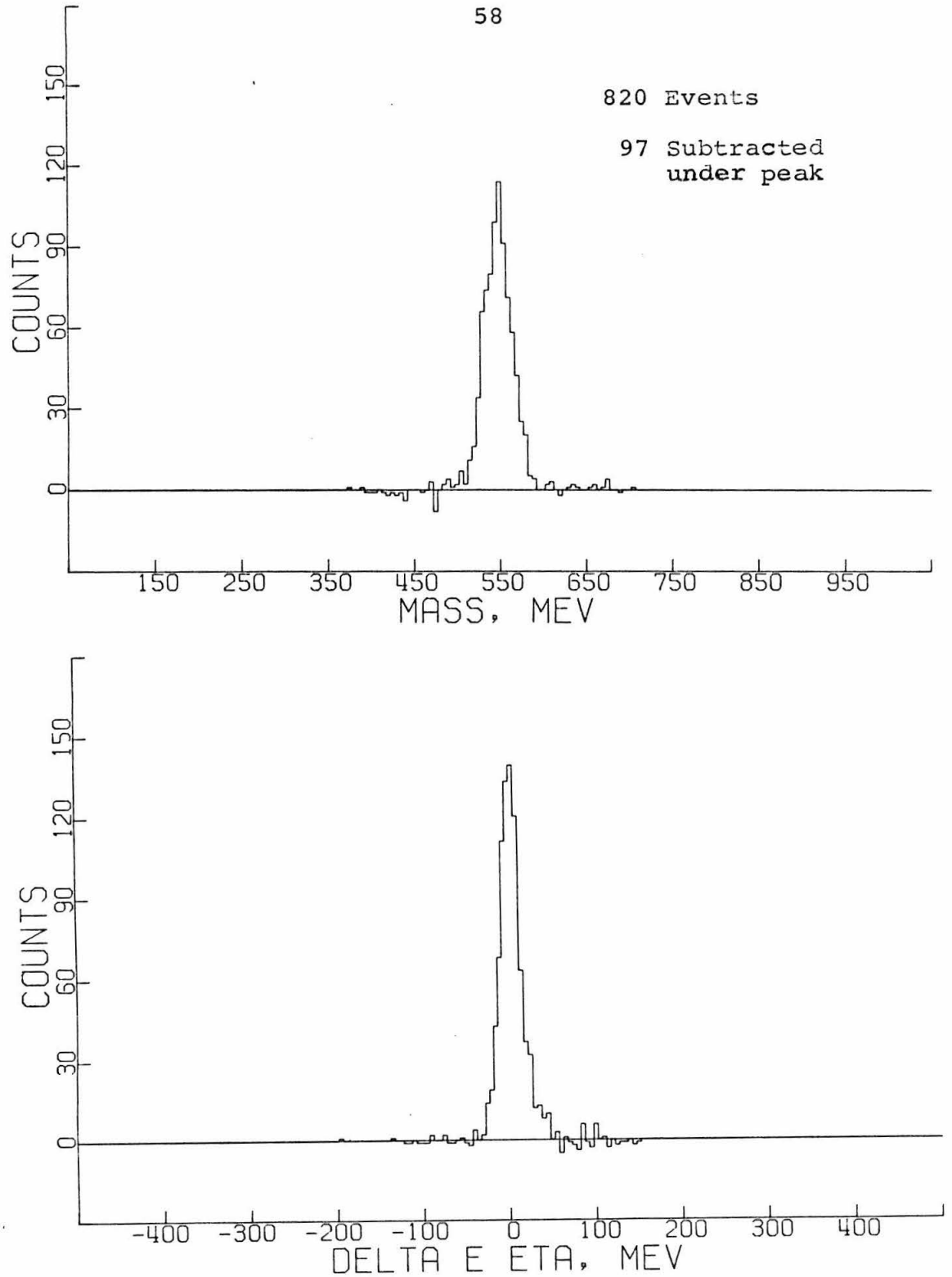

Figure 3.19 Subtracted mass and ΔE_η distributions for Setup IV

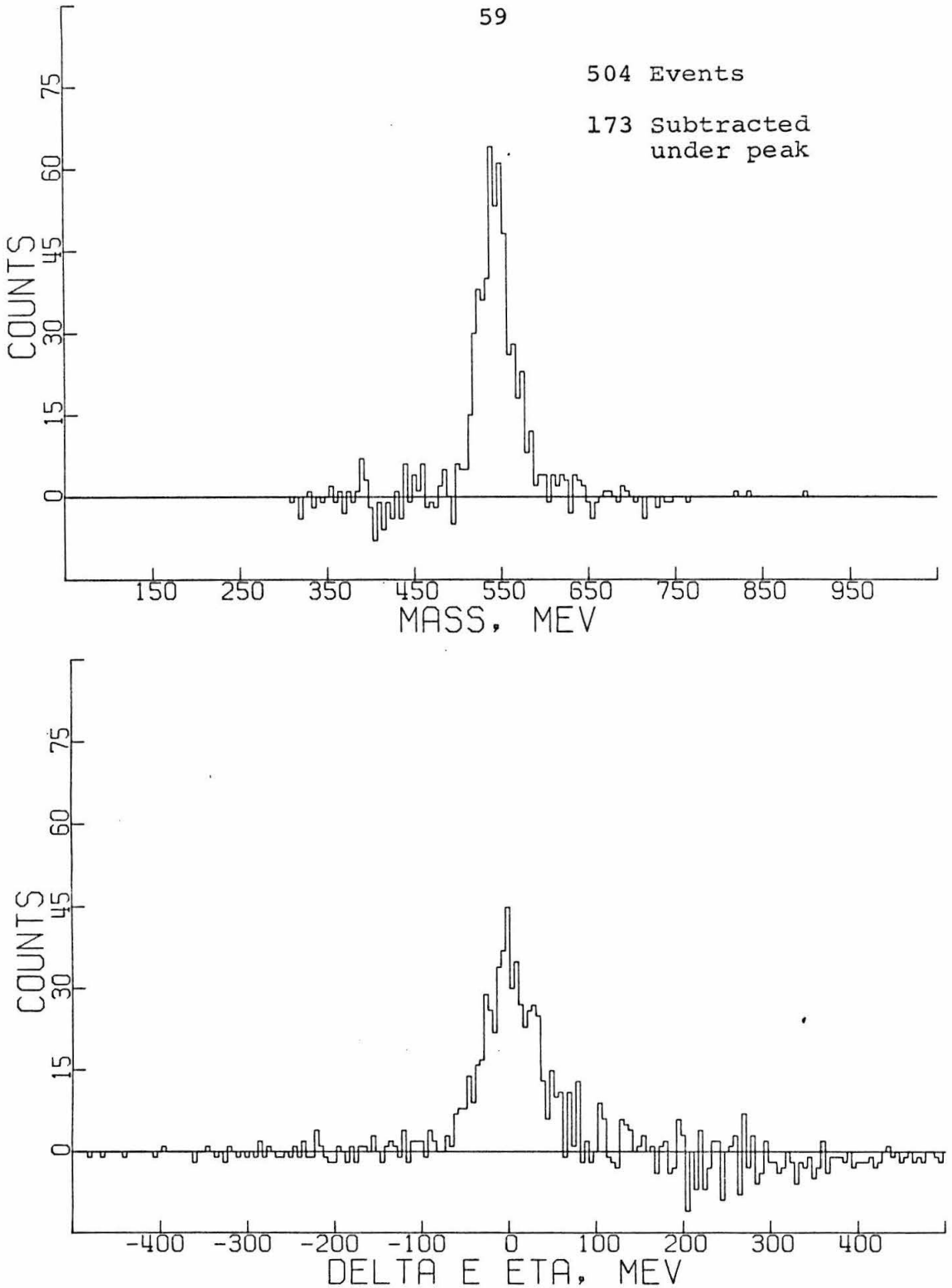

Figure 3.20 Subtracted mass and ΔE_η distributions for Setup V

independently, and the results agreed to within statistics.

After we determined the number of background events under the peak, as described above, we could perform the subtraction in the distribution of k, the incident photon energy. This was done by making a distribution of k for those simulated background events which lay in the region of the eta peak. This distribution in k was then subtracted from that for the actual events in the same region. Thus we obtained the k distribution for eta events. Figure 3.21 shows a superposition of the actual data and the calculated subtraction for a typical setting. The actual numbers for each setting are tabulated in Section IV, where the cross sections are given.

6. Efficiency and Resolution Calculations

To get the cross section from the counting rate we must calculate our efficiency, $\varepsilon(k)$, which is the probability, averaged over center-of-mass production angles, that etas produced from photons of energy k be detected in our system. This number is essentially $1/4\pi$ times the effective solid angle of our apparatus.

This was done using a Monte Carlo technique which simulated the actual setup as closely as possible. For ideal detectors of simple geometry, there is some chance to calculate detection efficiencies analytically, but

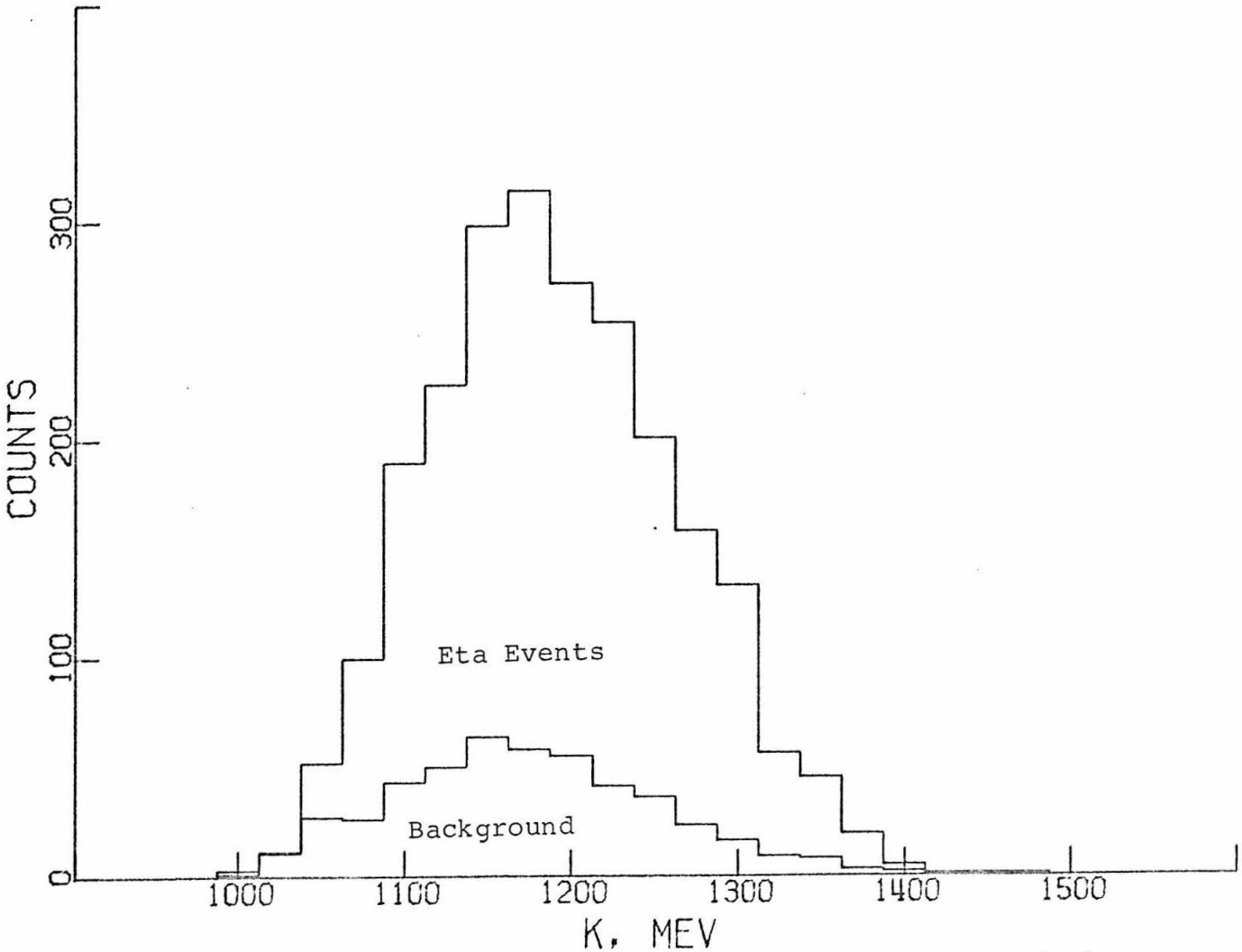

Figure 3.21 Distribution in k of events in the eta peak for a typical setup, showing calculated subtraction

this proved impossible in our situation. Factors which had to be considered included finite target size, variation of photon detection efficiency with energy and with position in the counter, loss of events out the sides of the range chamber, and variation of proton range in the apparatus due to non-normal incidence. Furthermore, because of the small effective solid angle of the apparatus, and the complexity of the kinematic calculations involved, the Monte Carlo method could not be applied naïvely. Having done so would have resulted in about ten successes per day of IBM 7094 computer time. To remedy this, two steps were taken. First, the production and decay angles were limited so that a generated event had a good chance of being detected. This required careful attention to choice of limits so that we could be sure that no good events would be lost. The second step involved choosing some variables from discrete distributions, rather than from continuous and random ones. For example, we divided the target into thirty uniformly distributed event origin bins, and the proton angles were chosen similarly. This allowed us to make some calculations only once for many event tries, thereby cutting the computing time down by almost an order of magnitude. The result of these two steps was that the program produced about 500 successful events per minute of computing time,

so that an hour of computer time gave Monte Carlo statistics which were very small compared to the experimental ones.

A typical efficiency curve covered about 200 MeV in photon energy and about 20° in center of mass production angle. The peak value of the efficiency was 1×10^{-5} to 2×10^{-5}, depending upon setting.

This efficiency function is, for two reasons, not the one used in calculating the cross sections. First, the number of photons is not constant as a function of k, and secondly, our experimental resolution affects the efficiency.

A slight refinement of our efficiency program gave us the experimental resolutions in our various calculated quantities. In this program, after an event was generated, the measured quantities were altered in a way which simulated the effects of our measuring apparatus. Four effects were included, as follows:

1) The proton was allowed to multiple-scatter before being "detected";
2) the range of the proton was taken to be the central value for the module in which it stopped;
3) the event origin was moved into the central vertical plane of the target; and

4) the positions of the decay photons were moved to the centers of the hodoscope bins which they traversed.

These altered values were then used to calculate M_η, ΔE_η, and k. The widths of the resulting distributions were taken to be our experimental resolutions. The resolution in mass and ΔE_η could be checked against our subtracted mass and ΔE_η plots; the resolution in k could not be checked.

The simulated distributions in mass and ΔE_η were found to be about 3 or 4 MeV narrower than those obtained experimentally. We think this is due to small fluctuating errors in the determination of the proton energy from the range. The mass in particular depends fairly sensitively on the proton energy, so that a 1 MeV error in the proton energy will lead to a 2 or 3 MeV error in the calculated mass. The calculated value of k is less sensitive to the proton energy, and we think that the calculated and actual resolutions in k should agree quite well. In any case, a discrepancy of the order that we see will not visibly affect the final answer, since the resolution width is small compared to the width of our efficiency.

Strictly speaking, we should use our known resolution in k to unfold our experimental distribution in k. Instead, we used the converse method, as follows: First, we calculated the number of counts expected as a function

of k, per unit cross section, using the known efficiency and photon spectrum. This result was then folded with our resolution in k, and we compared the resulting function to the distribution of counts obtained in the experiment.

The quantity obtained in this way is the cross section averaged over our resolution. For a constant cross section, the answer is unchanged by this averaging. Over much of the range of the experiment, the cross section turns out to be fairly constant. Also, at about 850 MeV, where there is a rapid decrease of the cross section with energy, our resolution has a gaussian sigma of only 6 MeV, which is much smaller than the energy scale of the cross section variation. Therefore, we feel that nothing has been lost by following the procedure outlined above.

The actual values obtained by this process are tabulated in Section IV, where the results are given.

IV. RESULTS

1. Cross Section Formula

The general relation which gives counting rate as a function of cross section is

$$C(k) = \overline{\frac{d\sigma}{d\Omega}}(k) \cdot N_p \cdot N_\gamma(k) \cdot \varepsilon(k) \cdot \Gamma \cdot 4\pi\Delta k \cdot \alpha$$

where

$C(k)$ = number of events in an interval Δk centered at k,

$\overline{\frac{d\sigma}{d\Omega}}(k)$ = differential cross section averaged over production angle acceptance and k interval and resolution,

N_p = number of protons in the target per cm^2,

$N_\gamma(k)$ = number of photons in a unit energy interval,

$\varepsilon(k)$ = efficiency for detection of event initiated from a photon of energy k,

Γ = branching ratio into mode of interest,

α = factor arising from systematic corrections.

Solving for the cross section, and inserting the

appropriate constants, we have

$$\overline{\frac{d\sigma}{d\Omega}}(k) = \frac{C(k)}{F(k)} \frac{E_o}{4\pi\alpha \cdot \Gamma_{\gamma\gamma} \cdot N_p \cdot W \cdot B \cdot \Delta k}$$

where

E_o = the synchrotron endpoint in MeV,

W = quantameter constant ($\simeq 1.12\times10^{13}$ MeV/BIP),

N_p = number of protons in target ($\simeq 0.93\times10^{24}$ /cm^2),

B = number of BIP's (unit of integrated beam energy,

and $\Gamma_{\gamma\gamma}$ = branching ratio for $\eta \to \gamma\gamma$ (=.406±.016).

$F(k)$ is the product of the efficiency and the bremsstrahlung spectrum folded with our experimental resolution:

$$F(k) = \frac{\int\{B(k)\cdot\varepsilon(k)/k\}\cdot\exp\{-(k-t)^2/2\sigma^2(t)\}dt}{\int\exp\{-(k-t)^2/2\sigma^2(t)\}dt}$$

where

$B(k)$ = the bremsstrahlung function,

$\varepsilon(k)$ = the detection efficiency,

and $\sigma(k)$ = the experimental resolution in k.

2. Systematic Effects

The factor α in the cross section formula is a correction for events lost for various reasons. Table

4.1 is a list of sources of event loss and the amount of each for a typical setup. Below, we give a little more detail about some of these.

The correction for photon preconversion results from the fact that some of the decay photons materialize in the hydrogen target and in the air path before reaching the veto counters. Since the veto counters will then detect charged particles, the system will not be triggered.

Missing events are those which appeared on the measure lists but which did not appear on the final list of analyzed events. Some of these events were skipped by the scanners, or mislaid while being handled; the rest are the events which were twice measured incorrectly.

Events with three-light hodoscopes are ones in which three adjacent counters in a single hodoscope set fired. This occurred when a particle in the shower was produced at a large enough angle to trigger an extra counter. They were not used in the analysis because the experimental resolution in M_η or ΔE_η was worse than for the standard events.

Events with double tracks are ones in which two tracks identified as protons penetrated the range chamber. In general, only one of these protons triggered the apparatus, but we could not tell which one, so the

Table 4.1

Typical Systematic Corrections

Effect	Loss (%)	
Electronic Inefficiencies		
Proton counter 1	1.5	
Proton counter 2	0.8	
Proton counter 3	0.5	
Gamma counters	-- (negligible)	
Veto counter 1	0.5	
Veto counter 2	0.5	
Photon preconversion	6.8	3.4% each counter
Scanning inefficiency	1.0	
Events not measured		
Missing	3.0	
Three-light hodoscopes	12.0	
Double tracks	2.0	

event was not analyzed.

The systematic uncertainty in all the above corrections taken together is about three percent. An additional systematic uncertainty arises in the measurement of beam normalization as described in Appendix VI.2, and is about two percent.

One other source of error hidden in the data is the calibration of the shower counter, and the measurement of conversion efficiency. Although the actual errors in these measurements were primarily statistical, the results were applied as an overall correction, and so the error propagates systematically. The magnitude of resulting uncertainty is about three or four percent.

The correction made for nuclear interaction discussed in Appendix VI.7 is not shown here.

3. Cross Sections

The cross sections obtained in this experiment are tabulated in Tables 4.2 through 4.6, along with some of the numbers that went into the result. Fifty-two data points are given, at three center-of-mass angles. In these tables, the results of each setup appear separately. For each setup, the outlying bins, which contain about 5% of the events, are not included, because a number of effects make those results less certain

Table 4.2

Cross Section Calculation for Setup I

$\langle k \rangle$ = 1200 MeV $\langle \theta^*_\eta \rangle$ = 50°

k MeV	F(k) $\times 10^8$	Raw Counts	Subtraction	Final Counts	$\frac{d\sigma}{d\Omega}$(μb/ster)
1075	0.955	100	26	74	0.229 ± .034
1100	1.500	190	43	147	0.289 ± .029
1125	2.000	226	50	176	0.260 ± .024
1150	2.480	299	64	235	0.280 ± .022
1175	2.770	315	58	257	0.274 ± .020
1200	2.830	272	55	217	0.226 ± .018
1225	2.600	254	41	213	0.242 ± .019
1250	2.210	201	36	165	0.220 ± .020
1275	1.750	158	23	135	0.228 ± .022
1300	1.280	133	16	117	0.270 ± .028
1325	0.850	56	9	47	0.163 ± .028

Table 4.3

Cross Section Calculation for Setup II

$\langle k \rangle$ = 1000 MeV $\langle \theta_\eta^* \rangle$ = 50°

k MeV	F(k) $\times 10^8$	Raw Counts	Subtraction	Final Counts	$\frac{d\sigma}{d\Omega}$(μb/ster)
925	1.070	113	30	83	0.419 ± .059
950	1.730	179	33	146	0.456 ± .045
975	2.480	177	40	137	0.298 ± .031
1000	2.790	137	38	99	0.192 ± .025
1025	2.480	140	25	115	0.242 ± .028
1050	1.790	104	20	84	0.254 ± .033
1075	0.990	46	17	29	0.158 ± .043

Table 4.4

Cross Section Calculation for Setup III

$\langle k \rangle$ = 850 MeV $\quad \langle \theta^*_\eta \rangle = 70°$

k MeV	F(k) $\times 10^8$	Raw Counts	Subtraction	Final Counts	$\frac{d\sigma}{d\Omega}$(μb/ster)
810	0.900	83	7	76	1.003 ± .122
820	1.580	139	11	128	0.962 ± .095
830	2.160	189	10	179	0.984 ± .076
840	2.600	235	10	225	1.028 ± .070
850	2.810	217	11	206	0.871 ± .063
860	2.790	219	10	209	0.890 ± .064
870	2.630	183	10	173	0.782 ± .062
880	2.260	145	7	138	0.726 ± .064
890	1.770	111	6	105	0.705 ± .071
900	1.320	78	4	74	0.666 ± .095
910	0.970	55	2	53	0.650 ± .091
920	0.670	29	1	28	0.496 ± .095
930	0.450	28	0	28	0.739 ± .140

Table 4.5

Cross Section Calculation for Setup IV

$\langle k \rangle$ = 1000 MeV $\langle \theta^*_\eta \rangle$ = 90°

k MeV	F(k) $\times 10^8$	Raw Counts	Subtraction	Final Counts	$\frac{d\sigma}{d\Omega}$ (μb/ster)
920	0.650	89	14	75	0.700 ± .090
940	1.270	125	12	113	0.540 ± .054
960	1.790	139	13	126	0.427 ± .041
980	2.170	135	15	120	0.336 ± .033
1000	2.420	93	11	82	0.205 ± .025
1020	2.410	88	9	79	0.199 ± .024
1040	2.190	73	8	65	0.180 ± .024
1060	1.730	56	5	51	0.179 ± .027
1080	1.270	39	3	36	0.172 ± .030
1100	0.810	22	1	21	0.157 ± .035

Table 4.6

Cross Section Calculation for Setup V

$\langle k \rangle$ = 1300 MeV $\quad \langle \theta_\eta^* \rangle = 50°$

k MeV	F(k) $\times 10^8$	Raw Counts	Subtraction	Final Counts	$\frac{d\sigma}{d\Omega}$ (μb/ster)
1200	1.030	44	9	35	0.392 ± .081
1225	1.480	53	14	39	0.304 ± .064
1250	1.920	57	16	41	0.246 ± .051
1275	2.310	65	21	44	0.220 ± .046
1300	2.640	79	24	55	0.241 ± .044
1325	2.860	85	17	68	0.275 ± .041
1350	2.950	65	15	50	0.196 ± .035
1375	2.910	73	14	59	0.234 ± .037
1400	2.700	60	14	46	0.197 ± .037
1425	2.280	41	12	29	0.146 ± .036
1450	1.190	32	13	19	0.184 ± .065

than the rest.

These same results are given graphically in Figures 4.1, 4.2, and 4.3. In Figure 4.1 we show the results of the three setups centered at 50° in the center of mass.

Tables 4.7, 4.8, and 4.9 show the cross sections retabulated for convenience. In Table 4.7 the results from the three 50° setups have been combined. Figure 4.4 shows this averaging of the 50° cross section. In all of these results, the errors quoted are statistical.

4. Mass of the Eta

For each setup, we calculated the mean of the subtracted mass distribution. The five mass values were then averaged. We obtained the result

$$M_{\eta} = 547.5 \pm 2.5 \text{ MeV}.$$

The error quoted is the root-mean-square deviation of the five values from the mean, not the statistical error. The statistical error would be 0.15 MeV.

The main systematic uncertainty in the result comes from the range-energy relation for protons in our setup. The results used are supposed to be good to better than 1%, which means that the average energy might be wrong by perhaps 1 MeV. This would lead to about a 2 MeV

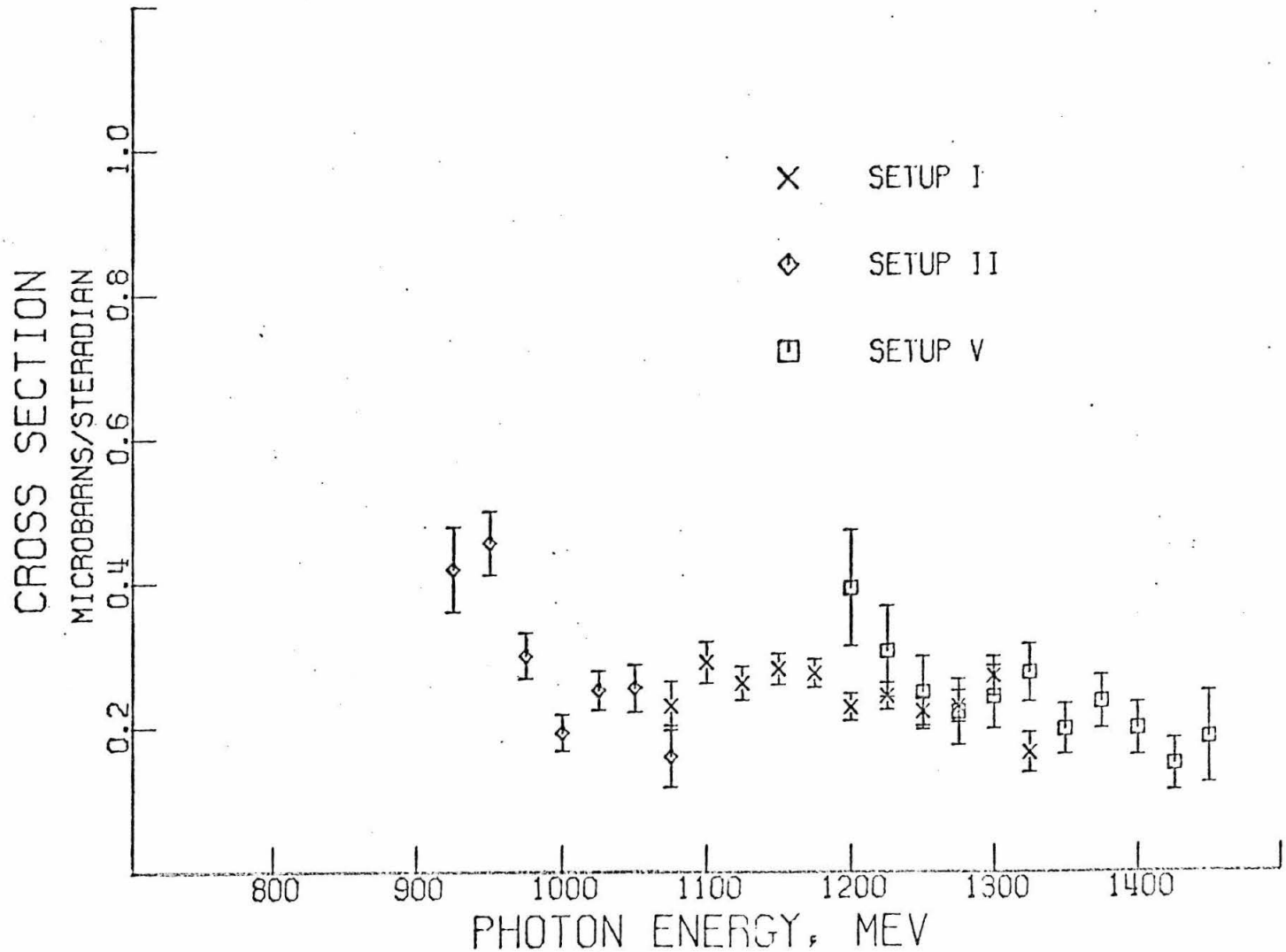

Figure 4.1 Eta photoproduction cross section at 50° C.M., for three setups

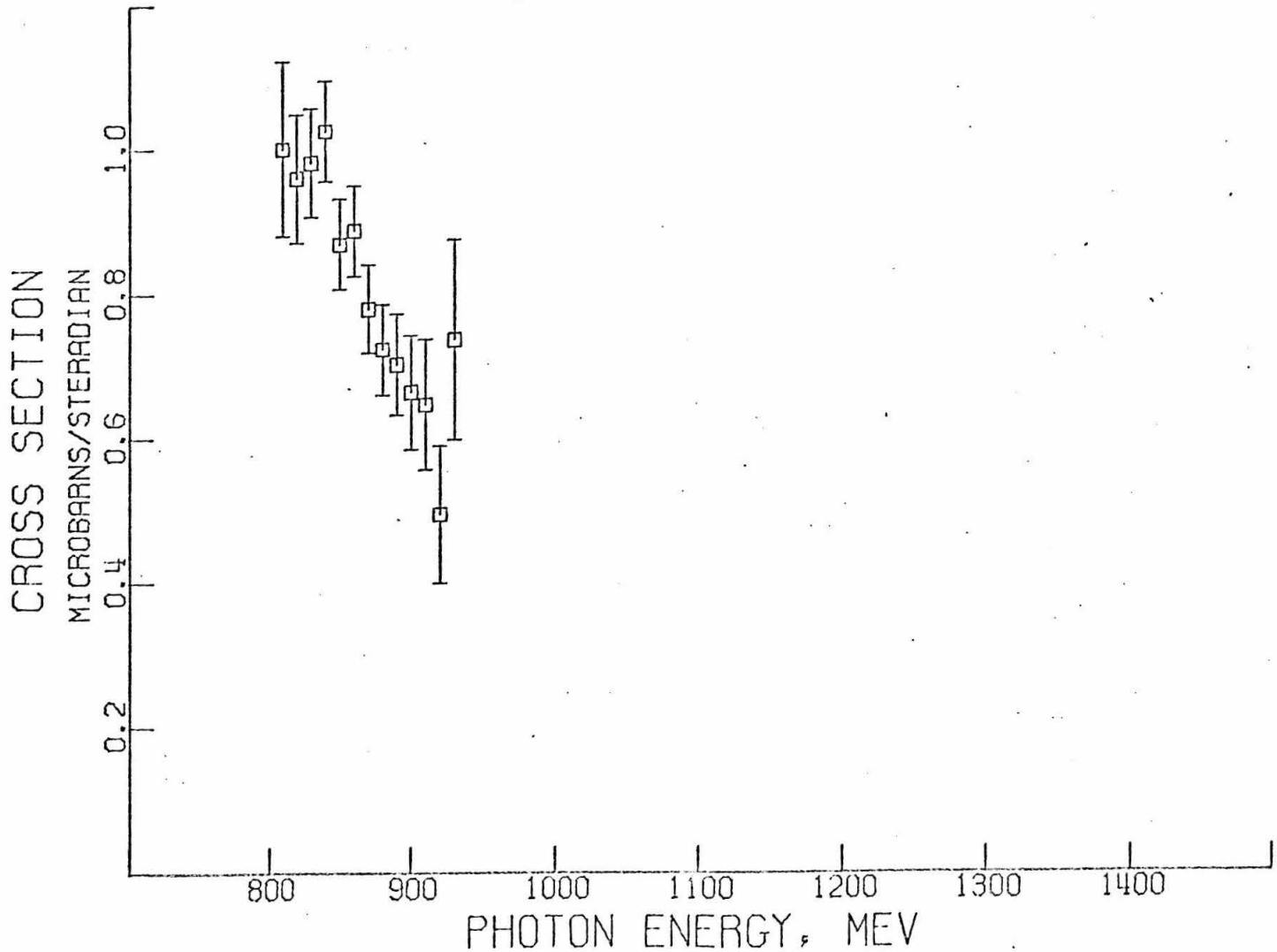

Figure 4.2 Eta photoproduction cross section at 70° C.M.

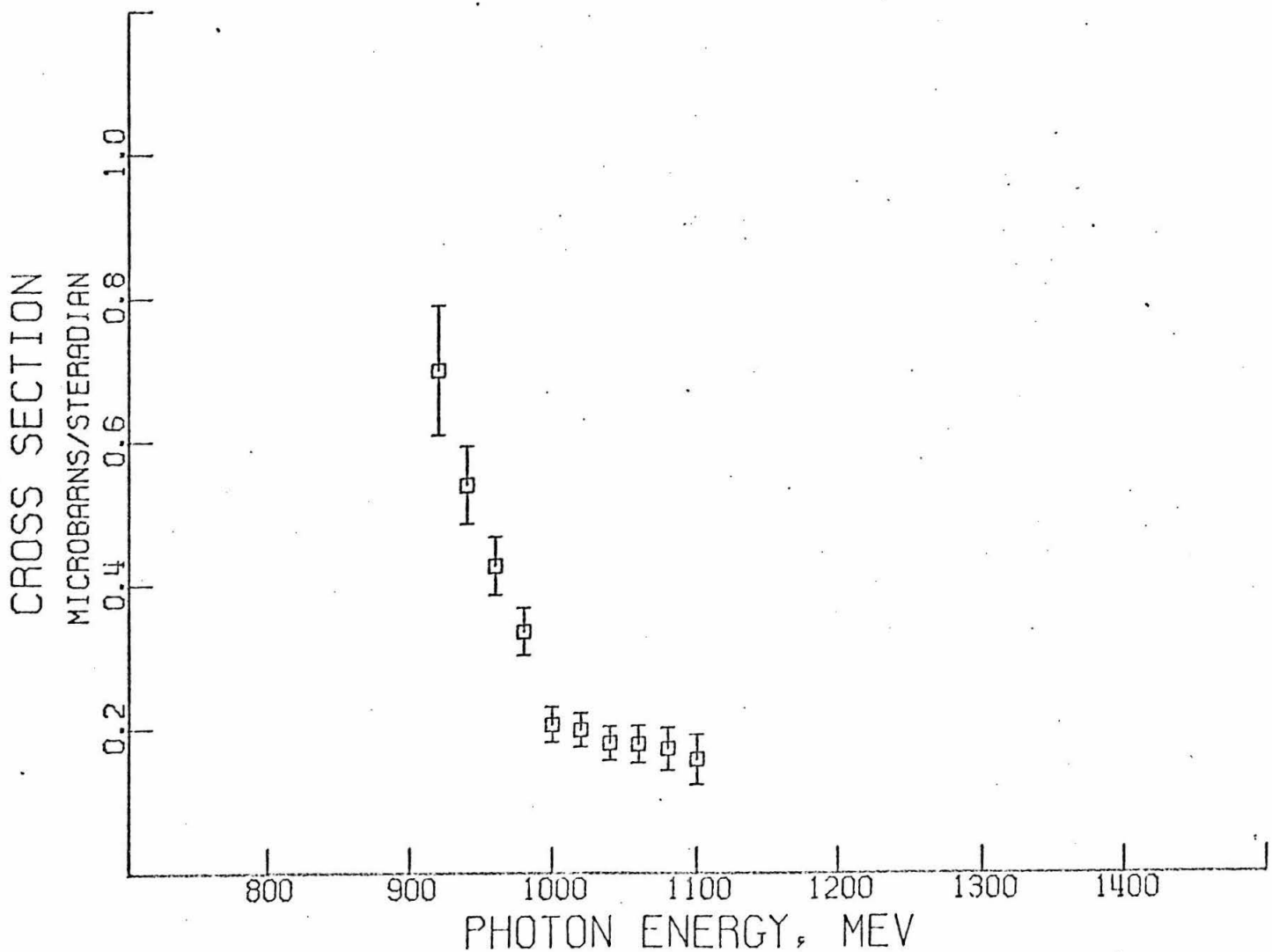

Figure 4.3 Eta photoproduction cross section at 90° C.M.

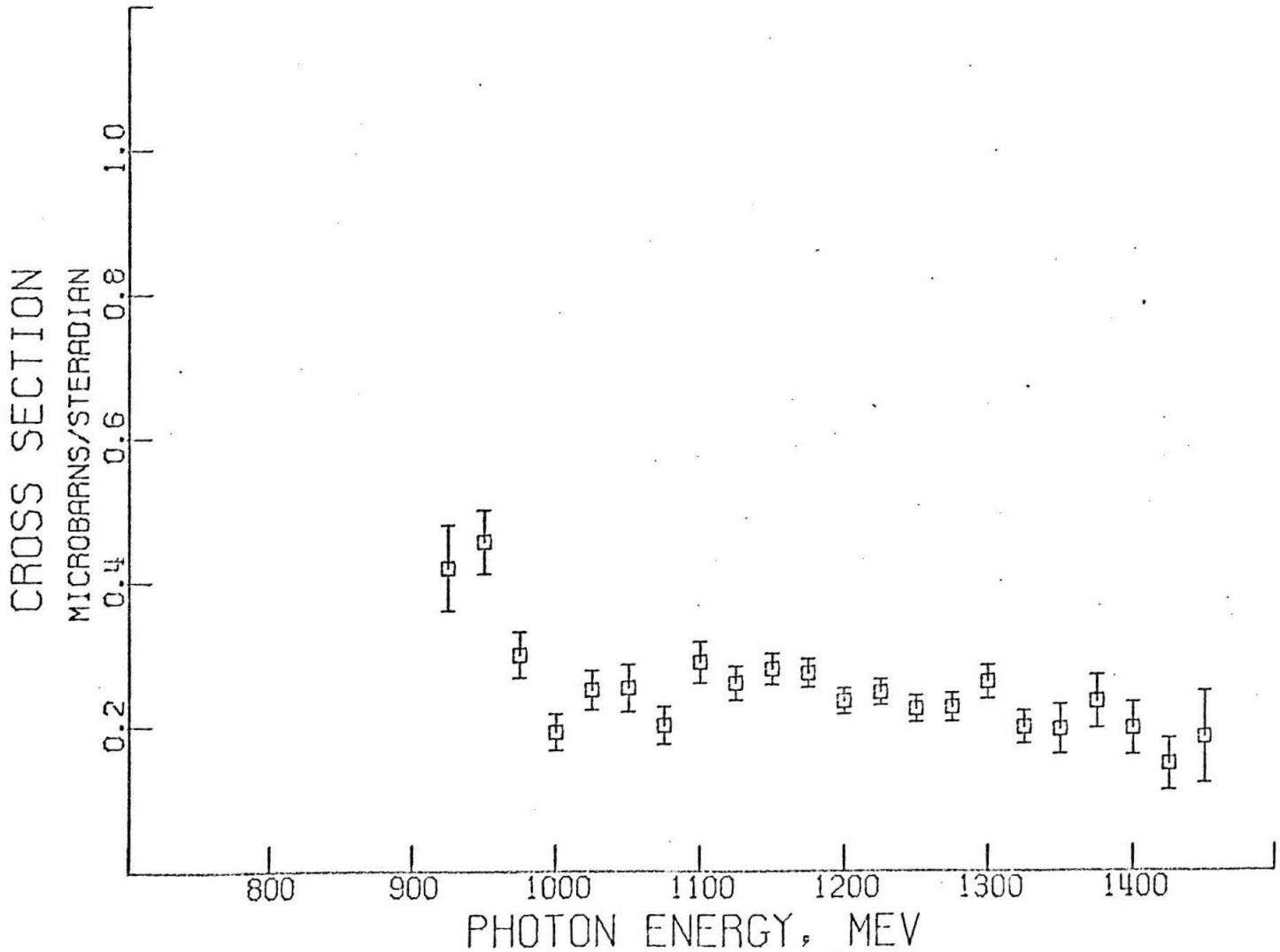

Figure 4.4 Eta photoproduction cross section at 50° C.M., averaged over three setups

TABLE 4.7

ETA PHOTOPRODUCTION CROSS SECTION AT 50° C.M.

k MeV	$\frac{d\sigma}{d\Omega}$(μb/ster)
925	0.420 ± .059
950	0.456 ± .045
975	0.299 ± .032
1000	0.192 ± .025
1025	0.251 ± .028
1050	0.254 ± .033
1075	0.202 ± .026
1100	0.289 ± .029
1125	0.260 ± .024
1150	0.280 ± .022
1175	0.274 ± .020
1200	0.234 ± .018
1225	0.247 ± .018
1250	0.224 ± .019
1275	0.226 ± .020
1300	0.261 ± .024
1325	0.198 ± .023
1350	0.196 ± .035

TABLE 4.7 (cont.)

ETA PHOTOPRODUCTION CROSS SECTION AT 50° C.M.

k MeV	$\frac{d\sigma}{d\Omega}$(μb/ster)
1375	0.234 ± .037
1400	0.197 ± .037
1425	0.147 ± .037
1450	0.184 ± .064

TABLE 4.8

ETA PHOTOPRODUCTION CROSS SECTION AT 70° C.M.

k MeV	$\frac{d\sigma}{d\Omega}$(μb/ster)
810	1.003 ± .122
820	0.962 ± .090
830	0.984 ± .076
840	1.028 ± .070
850	0.871 ± .063
860	0.890 ± .063
870	0.781 ± .062
880	0.725 ± .064
890	0.705 ± .071
900	0.666 ± .080
910	0.649 ± .091
920	0.496 ± .096
930	0.739 ± .140

TABLE 4.9

ETA PHOTOPRODUCTION CROSS SECTION AT 90° C.M.

k MeV	$\frac{d\sigma}{d\Omega}$(μb/ster)
920	0.700 ± .090
940	0.540 ± .054
960	0.427 ± .041
980	0.336 ± .033
1000	0.206 ± .025
1020	0.199 ± .024
1040	0.180 ± .024
1060	0.179 ± .027
1080	0.172 ± .030
1100	0.157 ± .035

shift in the apparent mass.

Another error which would shift the mass is a mis-estimation of the beam profile centroid, which would shift the average event origin and thus the average eta production angle. A change of 1 mm in the beam centroid would lead to a 0.7 MeV shift in the apparent mass.

The effect of surveying errors is quite small.

V. DISCUSSION

Figure 5.1 shows the results of this experiment, with the cross section at three center-of-mass angles on the same graph. Although we have not yet attempted a complete analysis of our data in terms of a phenomenological model, we can point out a number of features of the data and draw several conclusions:

1. The cross section between 800 and 1000 MeV exhibits the rapid decrease which has been seen before. Our points represent a substantial improvement in statistics over the previously existing data. The cross section is roughly constant over the angles measured, and agrees fairly well with the existing data, which are shown in Figure 5.2. The Frascati points (around 110°) were calculated using a branching ratio $\Gamma_{\gamma\gamma} = .386$. The Stanford points (around 100°) and the Orsay points (around 135°) do not depend on this number, although the Stanford data are normalized to π^o photoproduction cross sections.[6,14,15,16,17] The falling off of the threshold enhancement with energy is difficult to fit, and these new data with good statistics will be very useful in distinguishing among the various models proposed.

2. The cross section exhibits a slight, though statistically significant, dip between 1000 and 1100 MeV.

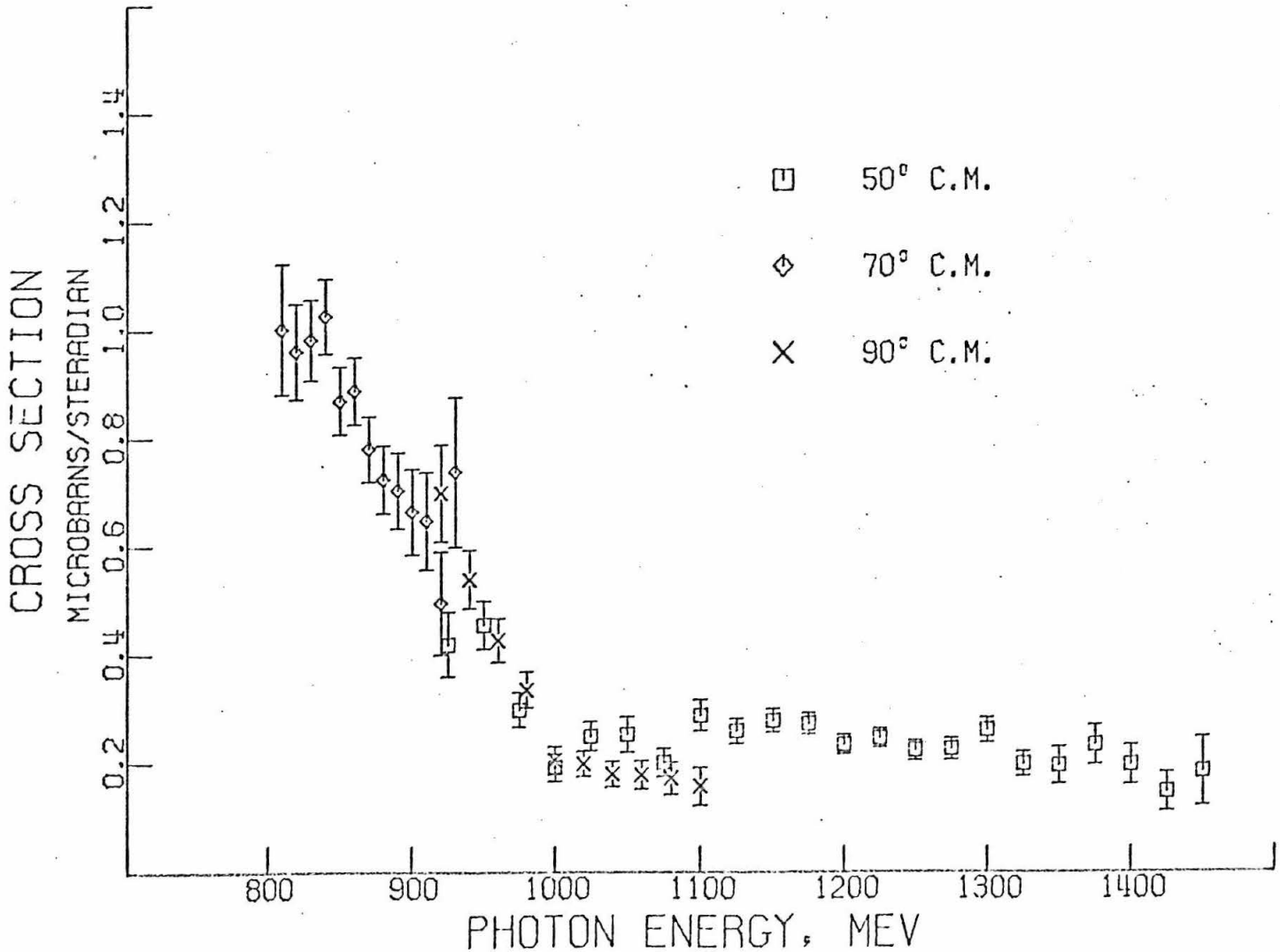

Figure 5.1 Eta photoproduction cross section at three center-of mass angles, as measured in this experiment

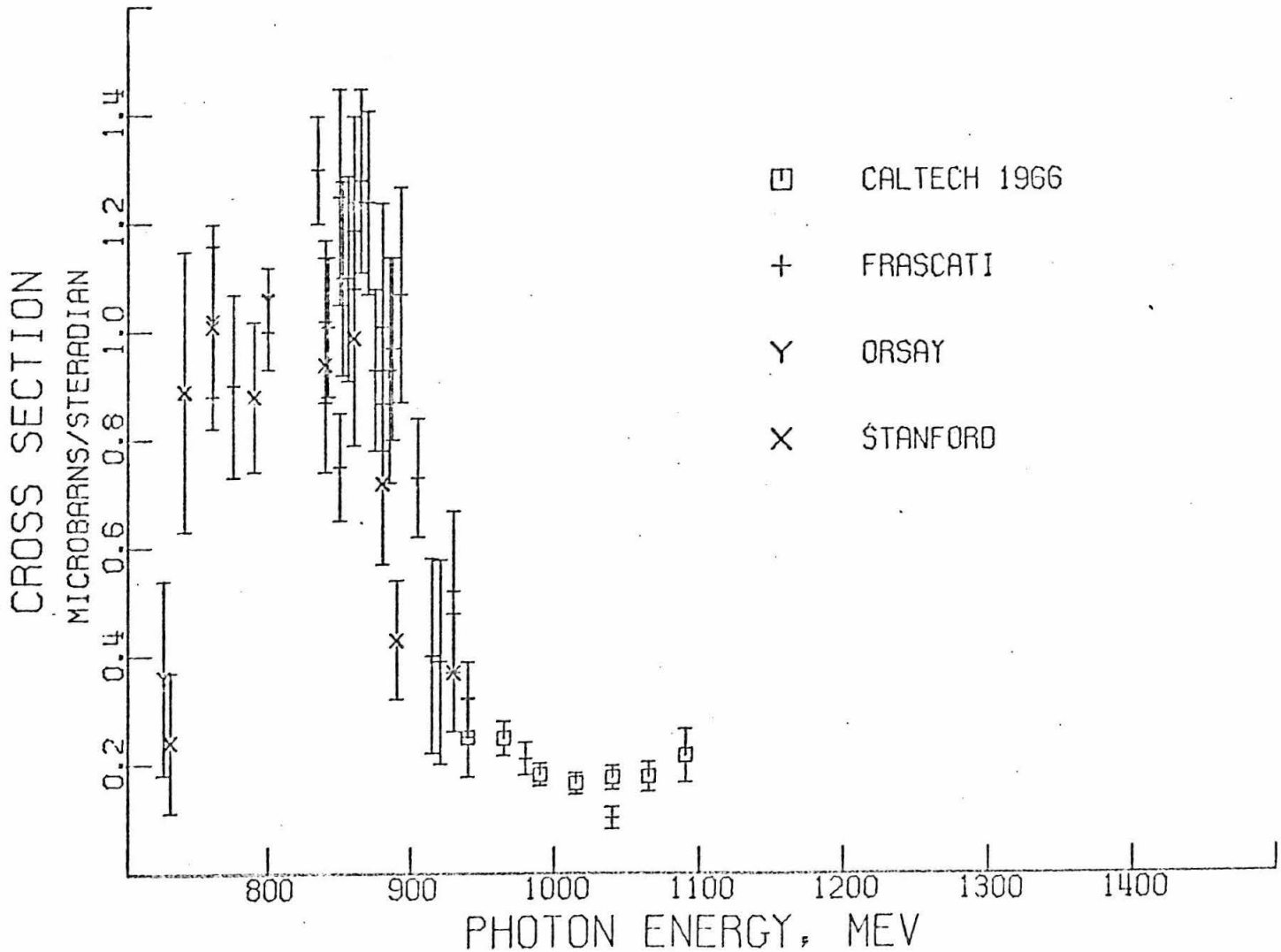

Figure 5.2 The total world's eta photoproduction data previous to this experiment

It is interesting to note that the same feature is indicated in pion production of etas.[21]

3. Between 1000 and 1100 MeV, the points at 90° fall below the points at 50°, which indicates a slight forward peaking. Such an angular dependence is seen in a recent Frascati experiment[11] at even lower energies.

4. The fairly small difference between the 50° and 90° cross section in this region indicates that the F_{15} (1688) resonance probably contributes at most only a small fraction of the already small cross section here. (The ratio of 50° to 90° cross section for a pure F wave is about 2.5 to 1.) This confirms the result of one of our previous experiments.[17]

5. The flatness of the 50° cross section between 1100 and 1450 MeV probably indicates that no resonance is contributing in any important way to this process. It would be very surprising if the cross section remained so constant at 50° throughout a 350 MeV interval while changing rapidly at other angles. We can therefore reasonably assume that there is probably not much angular variation going on through the entire region. Also, a bubble chamber point[22] in this region, which is a total cross section measurement, is consistent with our differential cross section if we assume a roughly isotropic

angular distribution, but does not exclude some forward peaking.

A number of workers have attempted to fit the eta photoproduction cross section with various models.[23,24,25] The fits of Deans and Holladay[25] are the most extensive and have been carried up to 1100 MeV. In their work, various combinations of diagrams, including the nucleon Born terms, isobar terms, and vector meson exchange terms, are fit to the data. The data which we have obtained should help to sharpen the fits up to 1100 MeV, and the roughly constant 50° cross section above 1100 MeV should provide a significant constraint on any fits attempted in that region.

It is clear that more cross section data are needed to enable us to untangle the diagrams which contribute to eta photoproduction. In particular, complete angular distributions at several energies will be invaluable.

The techniques used in our experiment become difficult, if not impossible, to apply outside the region where our data were taken, for a variety of reasons: At most other center-of-mass angles, the protons are produced at sufficiently small angles to the beam so as to make their detection in our spark chambers unfeasible. Also, range measurements for protons whose energies are above 350 MeV become increasingly difficult, because of large corrections for nuclear interactions; below about 60 MeV, the protons

do not have enough energy to leave the target and pass through the trigger counters. Finally, considerations of eta energy and direction further limit the accessible region. Thus, the complete investigation of the reaction will involve modes of detection which differ from ours.

Another kind of useful information comes from measurement of the recoil proton polarization in this process, described above in Section II. An experiment is currently being conducted at the synchrotron to determine this quantity as a function of energy from just above threshold to 1100 MeV, at 90° in the center-of-mass.

Finally, production off polarized protons, or using polarized photon beams, will help to complete the picture: the former experiment awaits technical advances in polarized target design, and the latter will probably have to be done in a bubble chamber, due to the extremely low polarized photon beam intensities currently available.

VI. APPENDIX

1. Photon Beam

The photon beam at the Caltech synchrotron is produced when the circulating electrons, which have been accelerated to energy E_o, strike a thin tantalum target in the synchrotron ring. For our experiment, the beam emerging from the synchrotron was collimated and then scraped at several points along its path by passing it through apertures in lead bricks. Before reaching the hydrogen target the beam passed between the poles of a permanent 3 kilogauss magnet, 10 inches long, which deflected some of the charged contamination out of the aperture of the last scraper. These features are seen in Figure 2.1. At the target, the cross section of the beam was a circle of radius 1.5 cm, and its angular divergence was 4 milliradians.

The differential energy spectrum of photons in the beam is given by

$$n(k)dk = \frac{W}{E_o} \frac{B(k,E_o)}{k} dk$$

where

k = photon energy,

E_o = energy of the accelerated electrons,

and W = total energy in the beam.

The function $B(k,E_o)$ is calculated using a Fortran program called BPAKI.[26] It is approximately equal to unity for k less than E_o, and is normalized such that

$$\int_0^{E_o} B(k,E_o)\,dk = E_o.$$

The uncertainty in $B(k,E_o)$ is estimated to be approximately 2%. W is known to about 1% as noted in Appendix VI.2. E_o is determined by measuring the peak field of the synchrotron and is known to 0.5%.[27] The small drifts of E_o over short periods can be ignored, since they average to zero over many runs, and are in any case, a few tenths of one percent of E_o.

Thus n(k) is known with an uncertainty of 2.5%.

2. Beam Monitoring

The total energy of photons in the beam was measured using a Wilson quantameter,[28] known as the "west" quantameter, situated downstream from our hydrogen target. The quantameter, which also served as a beam stopper, was mounted in a lead box backed by concrete, with an opening to admit the beam. The pressure, P, of the gas in the quantameter and its external temperature, T, were measured frequently. The value of P/T, which is proportional to the amount of gas in the quantameter, and thus also proportional

to the sensitivity of the device, was found to be constant to better than 0.2% for the first five months of the experiment, and then began to decrease linearly by about 0.15% per month for the remaining six months, due to a small leak. Since the quantameter was filled to a substantial overpressure, so that little outside air could leak in, we corrected for this leak by adjusting the sensitivity according to P/T.

The west quantameter was calibrated against a second, "south" quantameter, before and after our experiment, and the latter has been calibrated at intervals against a Faraday cup at the Stanford electron beam.[29] All of these measurements were internally consistent to within the measurement errors, which were typically 1.5%, and were also consistent with the calculated value of the sensitivity, W, which is the one used in our data reduction:

$$W = 13.10 \times 10^{18}\ T/P\ \text{MeV/coulomb},$$

where

T = temperature in °K,

and P = pressure in mm Hg.

The charge from the quantameter was collected and measured with a current integrator built at the lab, which was calibrated frequently during the experiment against a known current source. Its response was

constant to about 1% for most of the running time, but there were abrupt changes of two or three percent several times during the experiment. These changes were recorded and the overall response was known to typically 0.5% for a particular setting of the experiment.

During most of the experimental running, a synchrotron malfunction caused part of the internal beam to strike the radiator before the magnetic field had reached its peak value. Our trigger was inhibited by a beam gate during this "predump" and a relay shorted the quantameter output to ground at the same time. Because the relay took 0.75 milliseconds to pull in, the integrator was gated out for part of the time during which the trigger was sensitive. The correction due to this effect averaged about 0.2% and was less than 1% at worst. In the middle of the running, a delay was added into the trigger logic beam gate, which eliminated the effect.

The combined uncertainty in absolute normalization from all these sources was estimated to be about 2%.

3. Hydrogen Target

The liquid hydrogen target used in this experiment is shown in Figure 6.1, and has been described in

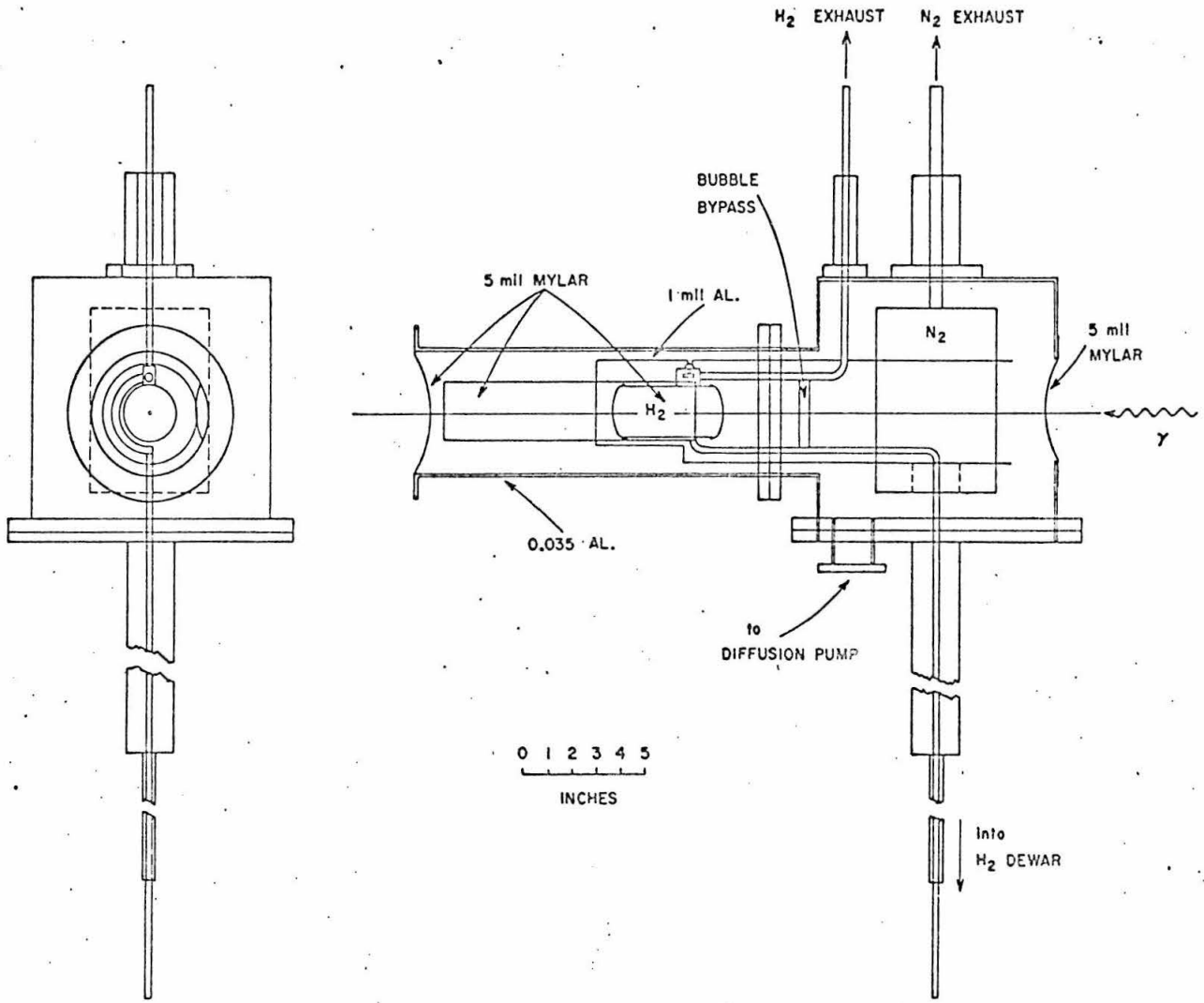

Figure 6.1 The hydrogen target

in an earlier thesis.[20] The hydrogen was contained in a cylindrical mylar cup 20.0 cm in length and 3.8 cm in diameter, oriented so that the beam passed along the cylinder axis. The cup was surrounded by an aluminum foil heat shield in thermal contact with a liquid nitrogen reservoir, and was suspended by its filling tubes in an evacuated aluminum cylinder with mylar end walls. A bypass tube connected the inlet to the outlet tubes to provide a path, other than through the cup, for bubbles formed in the filling tube. The beam traversed 0.012" of mylar in addition to the hydrogen, and the reaction products went through 0.005" of mylar and 0.035" of aluminum after leaving the hydrogen.

The liquid hydrogen was vented to the outside air, so that it was at approximately atmospheric pressure. Its temperature was 20.3°K, and its density was 0.0708 g/cm^3.

By observing that a typical bubble took about one second to rise through the target, and that about one-half liter of liquid hydrogen evaporated each hour, we may estimate the fraction of target volume occupied by gas bubbles, assuming that all evaporation took place through bubble formation at the bottom of the cup. A crude calculation gives about 0.5%. How-

ever, much of the bubbling took place in the bypass tube of the target, and some of the evaporation occurred at the top surface of the liquid, so that the calculated value is certainly quite high. Therefore, we have assumed that this effect is negligible.

For part of the running, a malfunction in the target filling system caused the hydrogen level to drop about 20 minutes after the initial filling. This was not noticed for over a week, during which time about 50 runs, constituting about 10% of the data, were taken. By comparing the distribution in vertical target coordinate for events in these runs with those in the normal runs, we found that 6.6 ± 1% of the beam passed through the target above the liquid level for the runs affected. The cross section obtained from these runs has been corrected for this effect.

4. Photon Detector

A. Apparatus

The apparatus used in this experiment was similar in most respects to that used in two previous experiments in our group,[17,30] except that additional hodoscope counters were added to help reject background. Figure 6.2 shows two views of the setup as employed in the experiment.

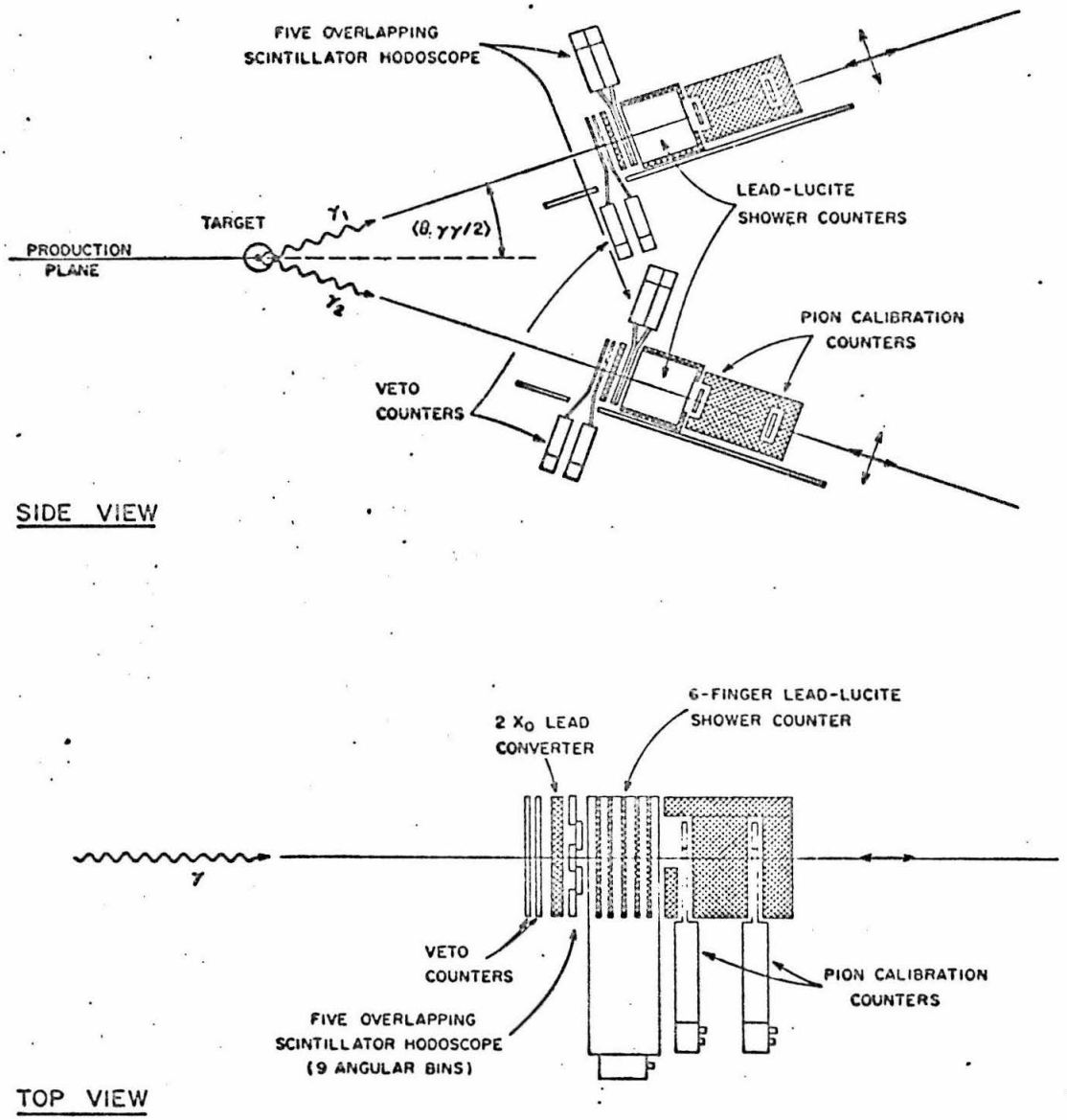

Figure 6.2 The photon detection system
(horizontal hodoscopes not shown)

Each of the two detectors had three important parts, each with a 6" by 10" aperture:

1) Two scintillation counters in coincidence, used to veto charged particles. Between the two was placed 0.060" of copper to help absorb low energy electrons making counts in the first scintillator. Since a coincidence was required to veto, a photon which converted in the copper would not be vetoed, and an electron which stopped before the second counter would not generate an accidental veto pulse. The system was about 98% efficient for minimum ionizing particles. In general, it was most useful at small angles to the incident beam; at our smallest angle, the trigger rate increased about a factor of two when the vetoes were removed from the logic, while at our largest angle, the rate remained about the same.

2) A hodoscope grid of scintillation counters, behind two radiation lengths of lead. Five overlapping vertical slats gave nine bins, and four horizontal slats gave seven bins, so that each grid element had dimensions 0.9" by 0.85", and had an angular acceptance of about 1.4° at the typical distance from the target in the experiment. The bias on each hodoscope counter was set so that the

counter would be 100% efficient for detecting minimum ionizing particles. Any photon converting in the lead would send at least one high energy electron through the hodoscope grid, so we were assured that all such photons would be detected. The probability that a photon convert in the lead was found to depend on the photon energy, as described in Appendix VI.5. Photons whose energies were above 400 MeV converted 79% of the time.

The extent to which the hodoscope system localized the photon shower can be seen in Figure 6.3, which shows a typical distribution of counts in the nine bins of the vertical hodoscope, and a schematic representation of the counter arrangement yielding these bins. Note that the even-numbered bins, where two counters overlap, contain more counts than do the odd-numbered ones. About one-third of this effect comes from shading of one counter by another for non-normal particles. The rest represents the effects of lateral shower spreading. To understand this, note that a photon headed toward an odd-numbered bin will sometimes send an electron through an adjacent counter, with the result that the count will appear in an adjacent (even-numbered) bin; but a photon aimed at an even-numbered bin will almost always send at

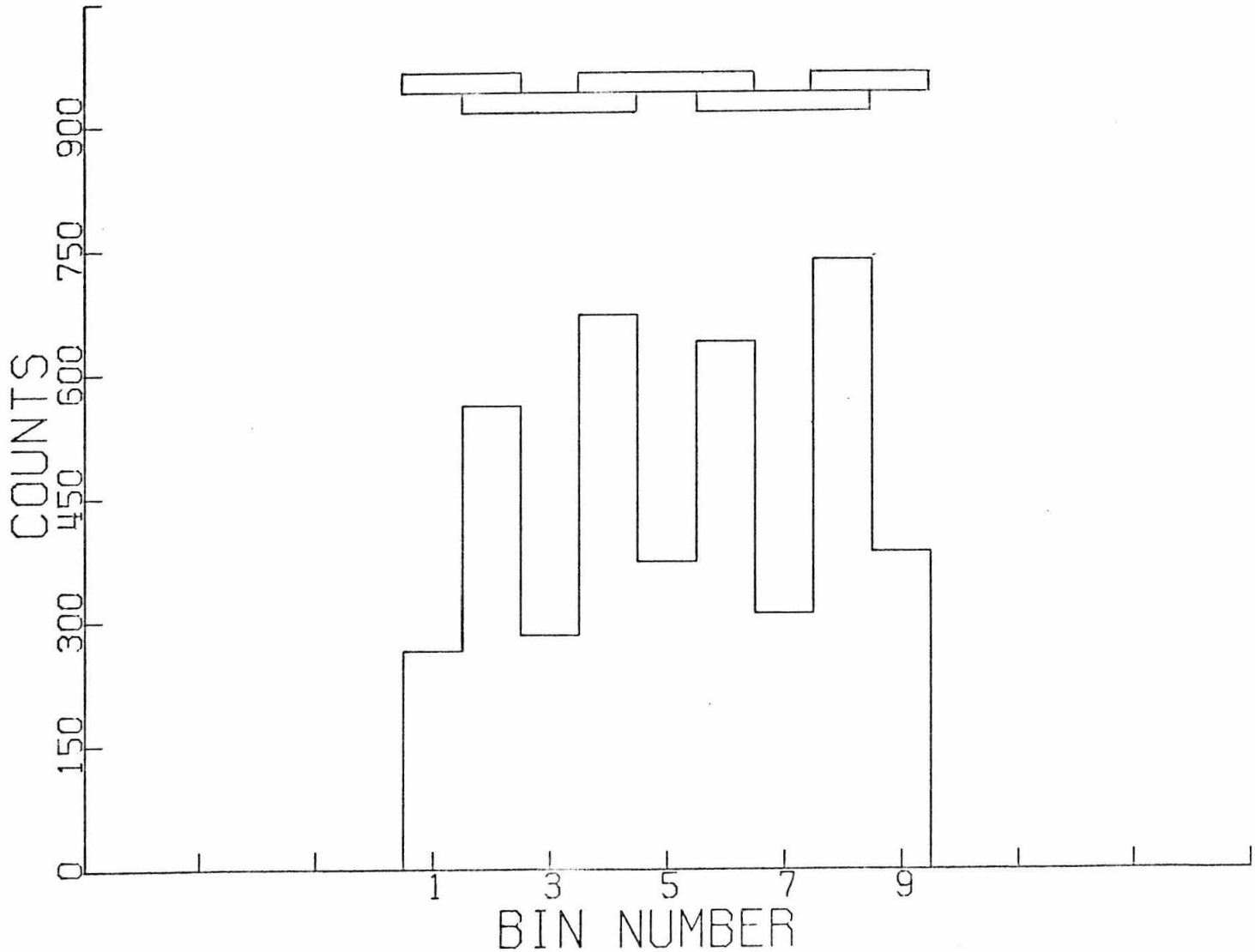

Figure 6.3 Distribution of counts in the hodoscope bins, showing counter combinations yielding each bin

least one electron through both counters constituting that bin. A shower half-width of about 2 mm at the hodoscope accounts for the effect observed.

3) A lead lucite Čerenkov shower counter. This consisted of six lucite plates attached to one lucite light pipe, with room between the plates to insert up to a total of five radiation lengths of lead. A 5" RCA 7046 phototube was used to collect the light. The basic structure of the counter can be seen in Figure 6.4. For photons normally incident on the center of the counter, the intensity of light given out was roughly proportional to the energy of the photon, with a gaussian sigma which went like $E^{-1/2}$ and was 10% at 1000 MeV. Near the edges of the counter, the behavior also depended on the angle of incidence (over and above the obvious effect of increased path length) and on the distance from the edge. Details of the energy calibration, including edge effects, are given later in this appendix (VI.4. C).

B. Photon Conversion Efficiency

As we mentioned earlier, the probability that a photon convert in the lead in front of the hodoscope depends upon the energy of the photon. This probability was measured using the monochromatic photon facility of the Caltech synchrotron. Electrons are produced in

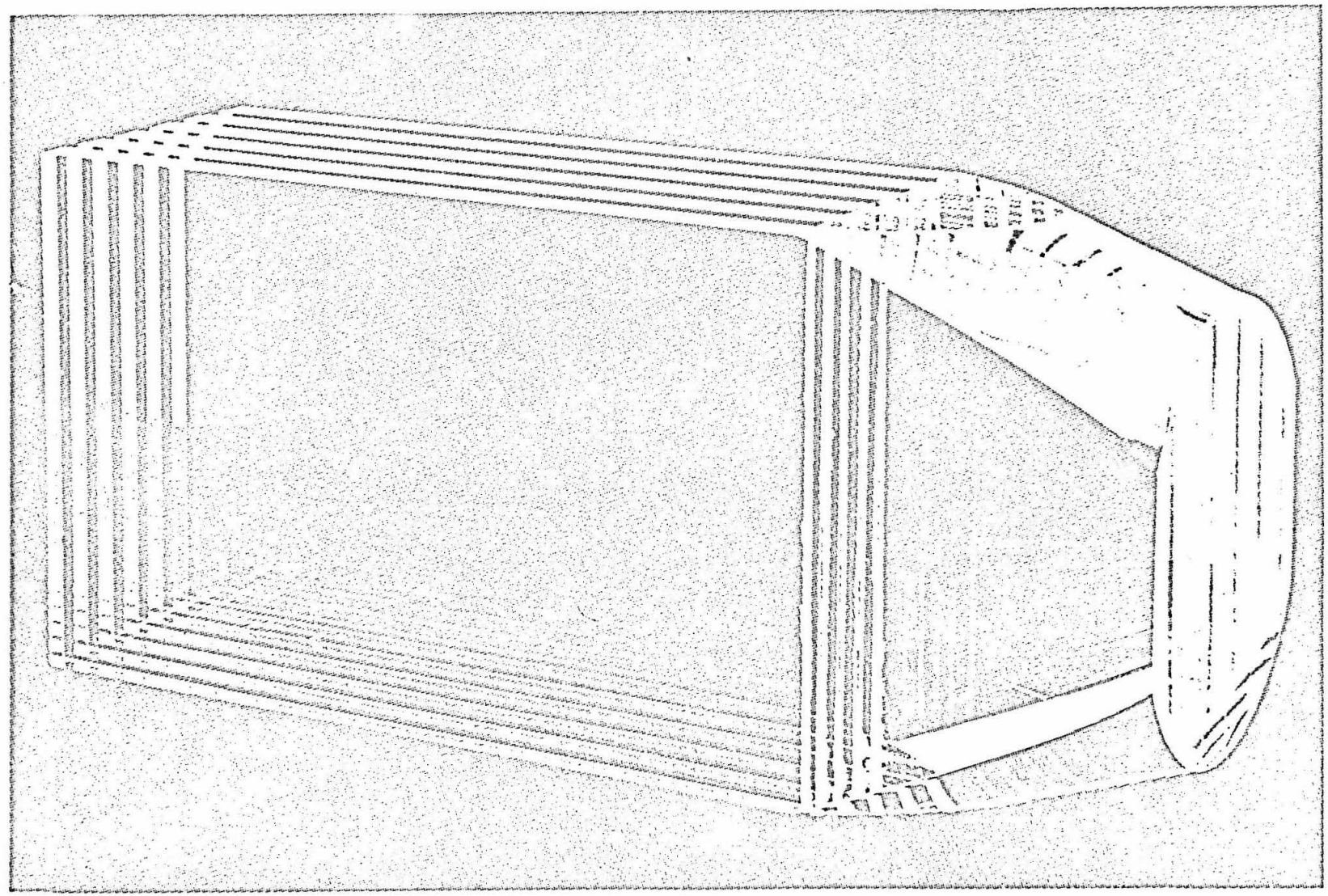

Figure 6.4 The unwrapped lucite radiator

a target placed in the bremsstrahlung beam, and those of energy E_1 are focused on a small defining counter. These electrons pass through a thin radiator, where some of them radiate a photon, and emerge with energy E_2. A second magnet selects these electrons in fast coincidence with the incoming electrons, and with veto counters placed strategically. The difference between the incoming and outgoing electron energies, E_1-E_2, must be the energy of the photon produced, which emerges almost exactly in the direction of the electron.

Before measuring the photon conversion efficiency, we compared the pulse height distributions developed in the shower counter for photons of a given energy with those from electrons of the same energy. (Electrons are obtained by turning off the second magnet and allowing the initially focused electrons to pass undeflected into the test setup.) In each case, the trigger supplied from the standard counters was used to gate the pulses from the shower counters. We found that the photon and electron spectra differed in that a few percent of the photon triggers produced essentially zero pulse height in the shower counter, while this did not occur in the case of the electrons. However, when in addition to the photon trigger

provided, we required a count in one of the hodoscope counters and no count in our veto counters, the low pulse height events disappeared, and the electron and photon spectra became identical. We decided that the extra counts were spurious accidentals which did not send photons into our counter, and to eliminate them when measuring the conversion efficiency, we required a reasonable pulse height in the shower counter.

Figure 6.5 shows the fraction of photons which gave pulses in the hodoscope counters as a function of photon energy. In principle, the effects of finite photon energy resolution and of second order bremsstrahlung processes should be unfolded from this curve, but both of these effects will be negligible, since the conversion efficiency is fairly constant over the whole region of interest.

C. Shower Counter Calibration

In the analysis, we accepted only those events in which the shower counter pulse heights were above some minimum value. This caused some small loss of real eta events, but depleted the background events more than it did etas, as has been seen in Section III.4. It was important, therefore, to determine how many photons would be lost as a function of photon energy

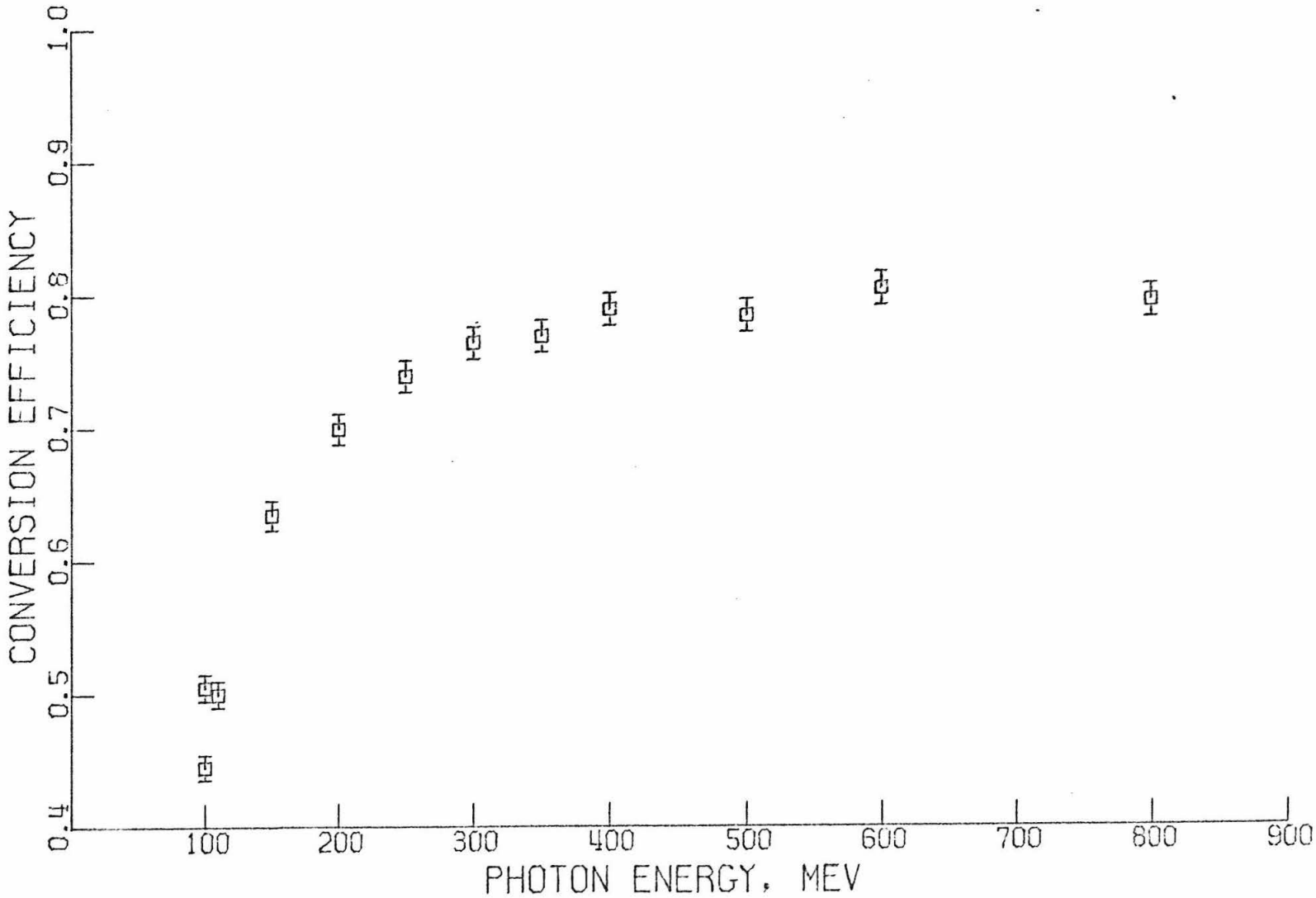

Figure 6.5 Photon conversion efficiency

due to this pulse height cutoff.

Electrons rather than photons were used to perform the energy calibration of the shower counter, since they were more plentiful by about a factor of 1000. As noted before, we verified in several cases that the spectra from electrons and photons of the same energy were the same. The counter was calibrated as assembled in the experiment, with the results shown in Figures 6.6 and 6.7. The $\beta = 1$ peak was obtained by removing the lead from the counter and allowing 600 MeV electrons to pass through it.

For photons near the edges of the counter, sizeable corrections must be made to these curves. At the edge opposite the light pipe, part of the shower will "leak out" of the counter, especially if the photon impinges at an oblique angle. On the edge attached to the light pipe, the effect is obviously different, since here any part of the shower which enters the light pipe may produce more light because of the extra lucite radiator. Furthermore, non-normally incident photons hitting the lead near an edge would sometimes produce showers that missed the hodoscopes completely. We investigated both of these effects, again using electrons rather than photons. We used a 1/4 inch cube of scintillator as a defining counter to localize the electrons. We varied

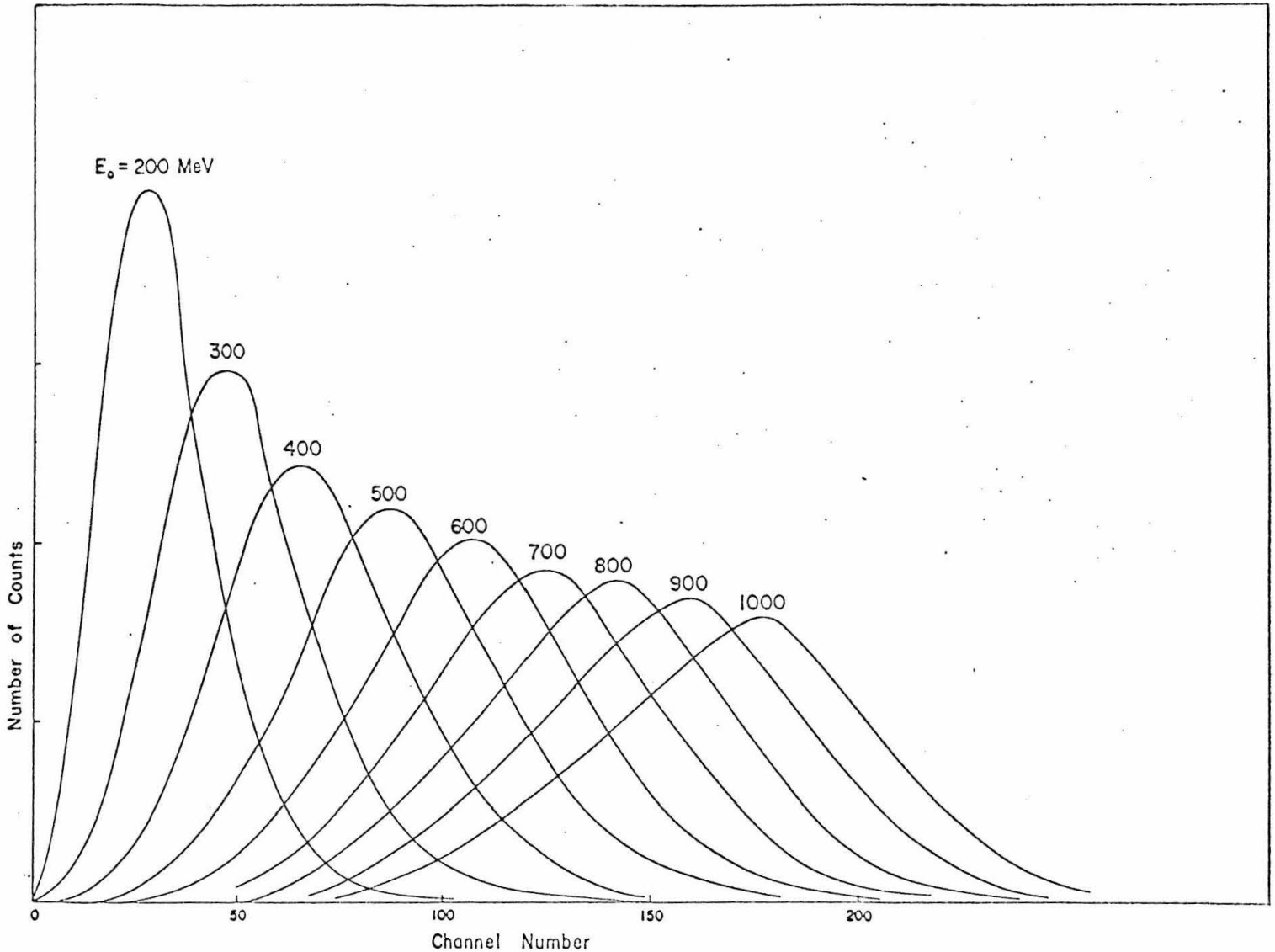

Figure 6.6 Pulse height distributions in the shower counter for mono-energetic electrons

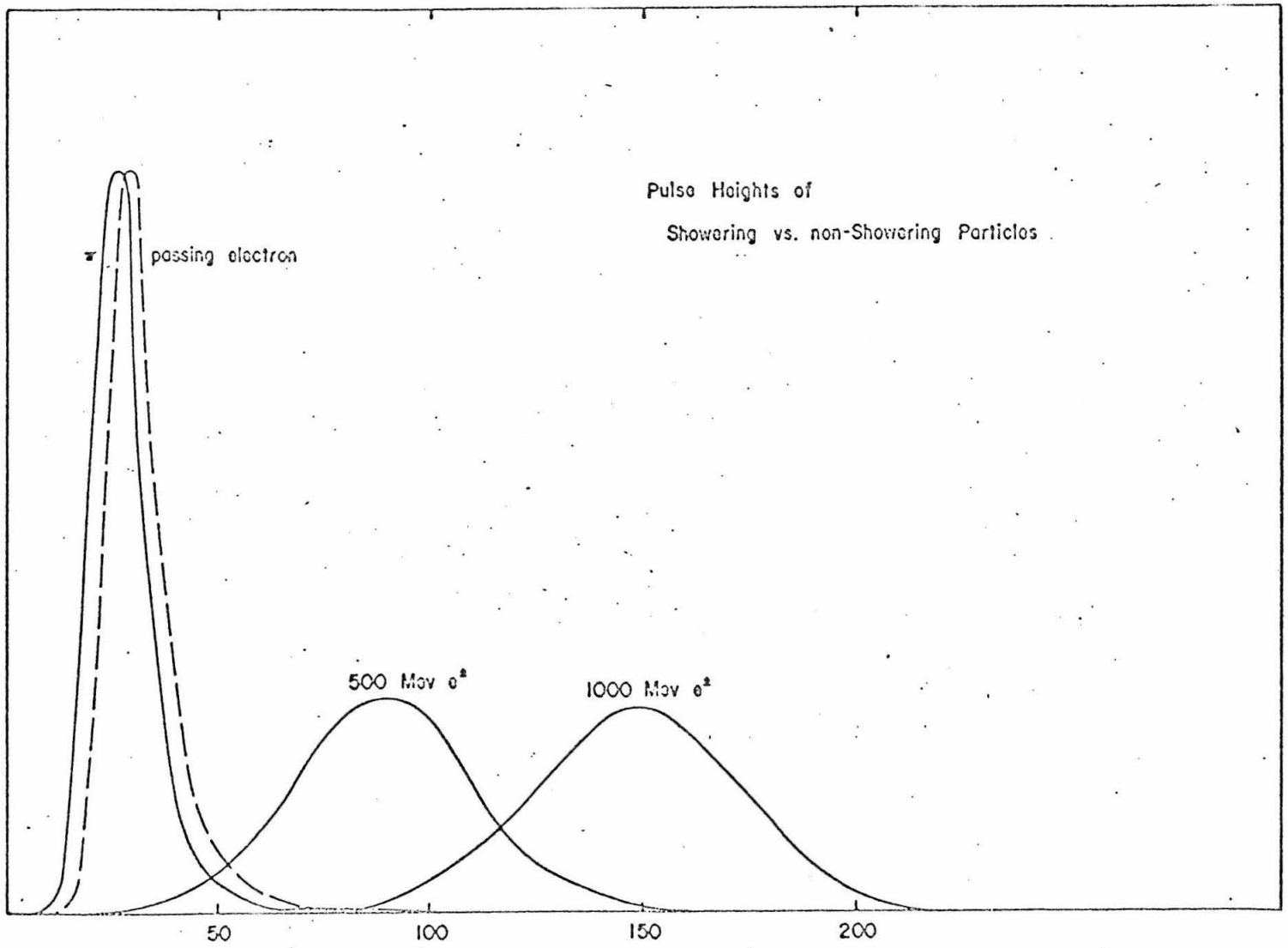

Figure 6.7 Distribution from $\beta \simeq 1$ non-showering particles compared to typical electron distributions

electron energy, angle, and distance from the edge and took distributions at each of the four edges. The results of this investigation are voluminous and we will not show them here. The effect could have been avoided had the shower counter been made with a larger aperture than the hodoscope. In general, the bulk of the effect occurred within one centimeter of an edge, at typical electron energies and incident angles.

The data obtained in these calibrations were used to calculate the experimental eta detection efficiency, as described in Section III.6.

D. Pion Counters

Behind each photon detector we placed two smaller scintillation counters with six inches of lead between them. These counters, operating in coincidence, triggered mainly on fast pions and muons and provided us with a source of non-showering particles with $\beta \geq 0.96$. These particles were used to check veto and hodoscope efficiencies during the experiment, and to monitor the gains of the shower counters.

5. Proton Telescope

A. Apparatus

The proton telescope consisted of three scintillation

counters and several spark chambers, as shown in Figure 6.8. It is essentially the same as that used in a previous experiment.[30] Each of the three counters measured 35 cm by 35 cm by 1/4 inch and was carefully centered to insure that only the last one determined the proton solid angle. This last counter was typically 190 cm from the target center.

The bias on each of the three proton counters was set so as to detect all protons in the energy range of interest (typically 80 to 250 MeV), and at the same time to discriminate against pions and electrons, which tend to be minimum ionizing. This was accomplished using a fourth counter, one-inch-thick, behind the range chamber, whose bias was set high enough to detect only heavily ionizing particles which stopped in it. This counter in coincidence with two of the telescope counters provided a sample of events rich in protons in the third counter. The bias in this counter was set to include these protons and to partially exclude the minimum ionizing peak, which was also visible. Any protons of interest in the actual running would stop in the range chamber, and would produce pulses even higher than those of our calibration sample. Figure 6.9 shows our calibration distribution with bias indicated, and a distribution of pulse heights from actual event triggers, for one of the proton scintillators. It can be seen that there is no event loss due to electronic

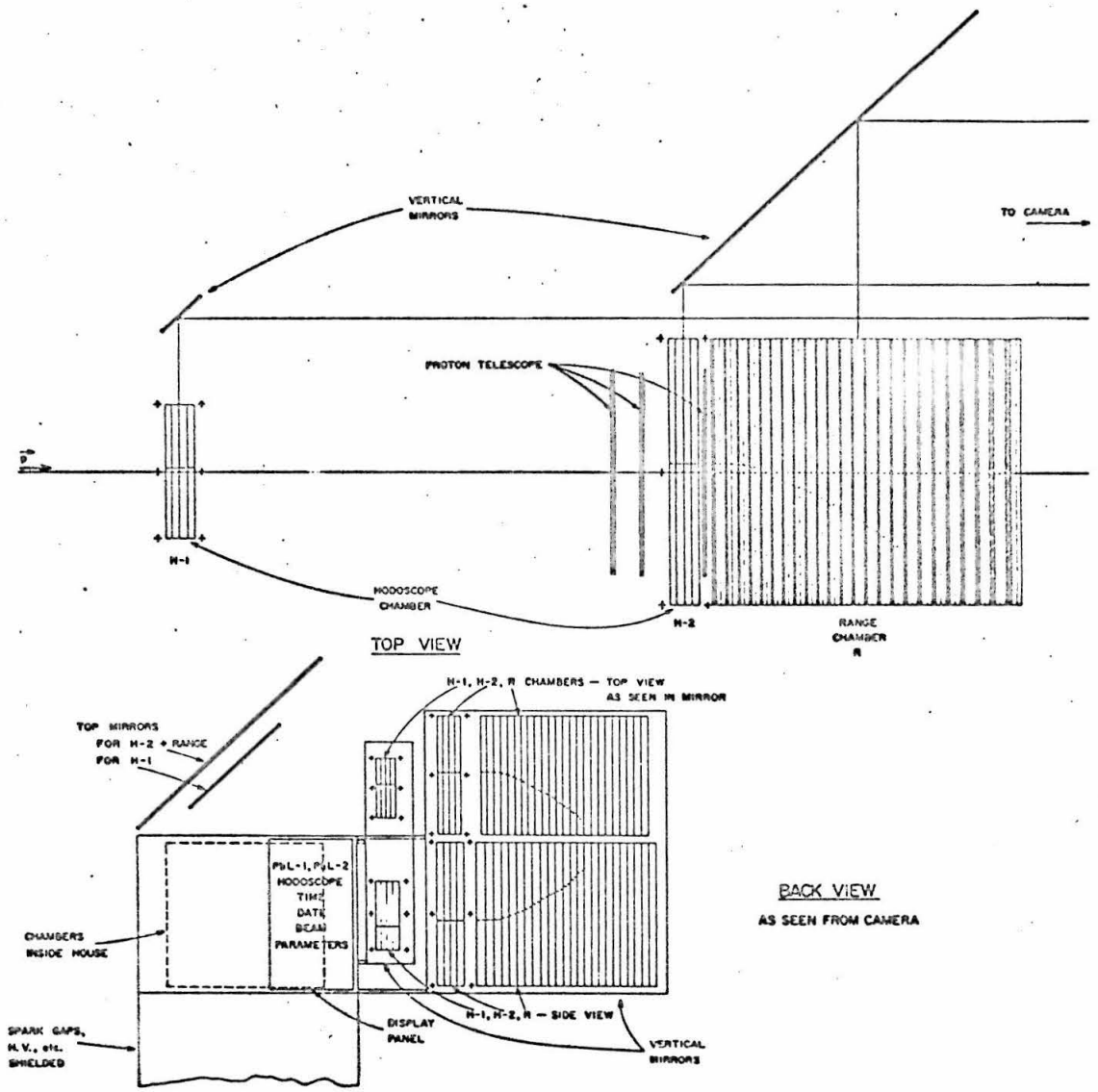

Figure 6.8 The proton detection system

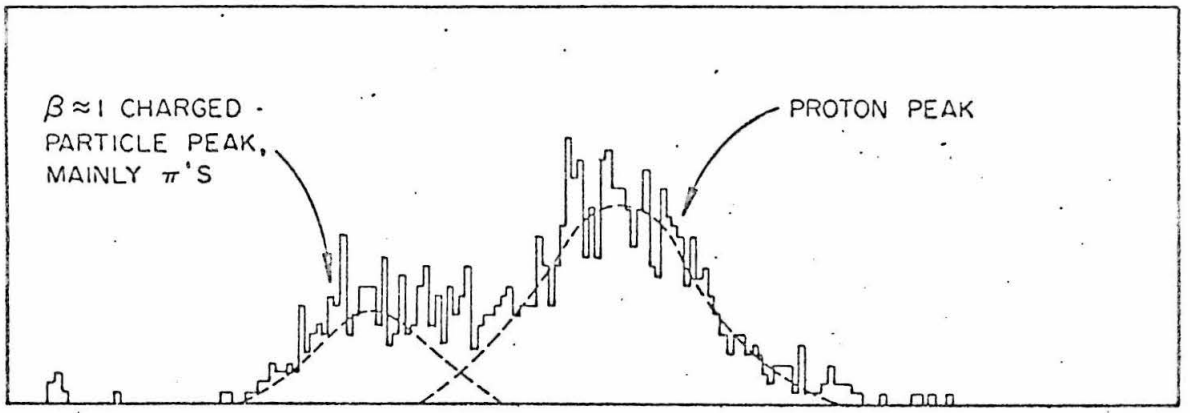

Calibration distribution

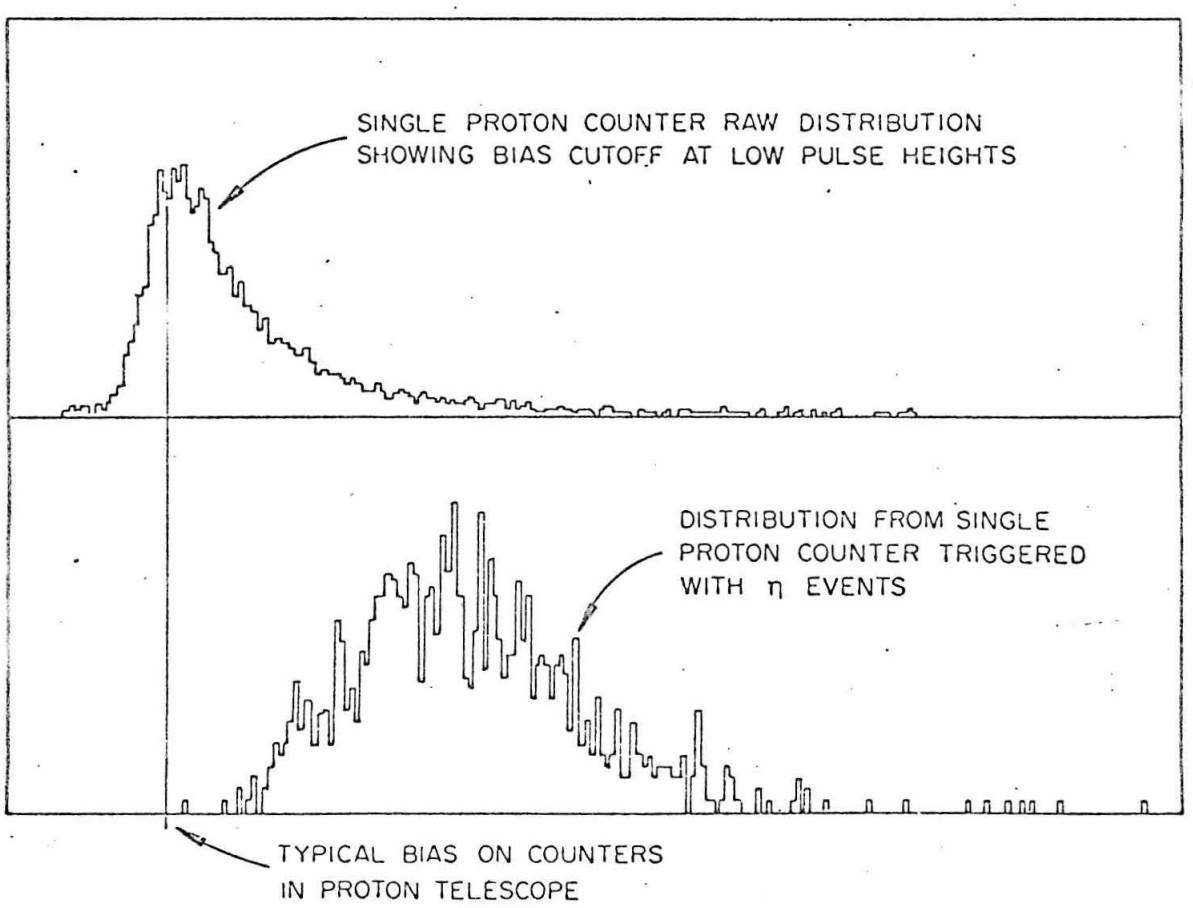

Distribution of protons associated with η's

Figure 6.9 Typical proton counter pulse height distributions

bias.

The two thin foil chambers contained four gaps each, separated by stretched 0.001" aluminum foil. The active area of the first was 8" by 10", and of the second, 17.5" by 17.5", as described in Reference 20 . The range chamber was modular, and consisted of alternate two gap sparking modules, and carbon modules. These have been described before,[30] and are shown in detail in Figure 6.10.

The chambers were run at 16 kilovolts, with a 50 volt sweeping field across the plates. An argon-helium mixture with some ethanol vapor added was used. The individual gaps were very efficient for single tracks and the two gap modules were 100% efficient. In the case of multiple tracks, there was some inefficiency, but the tracks could almost always be reconstructed by comparing the sparks in both views of the chambers.

B. Optics, Fiducials, and Surveying

All the chambers were viewed in 90° stereoscopy through mirrors, which were mounted flat on metal plate backings. Distortions across the face of the mirrors were measured and found to lead to negligible distortions in the photographed tracks.

Because of the size of the range chamber, field lenses were required to see into the gaps. We used two plano-convex plastic lenses, each with a focal length

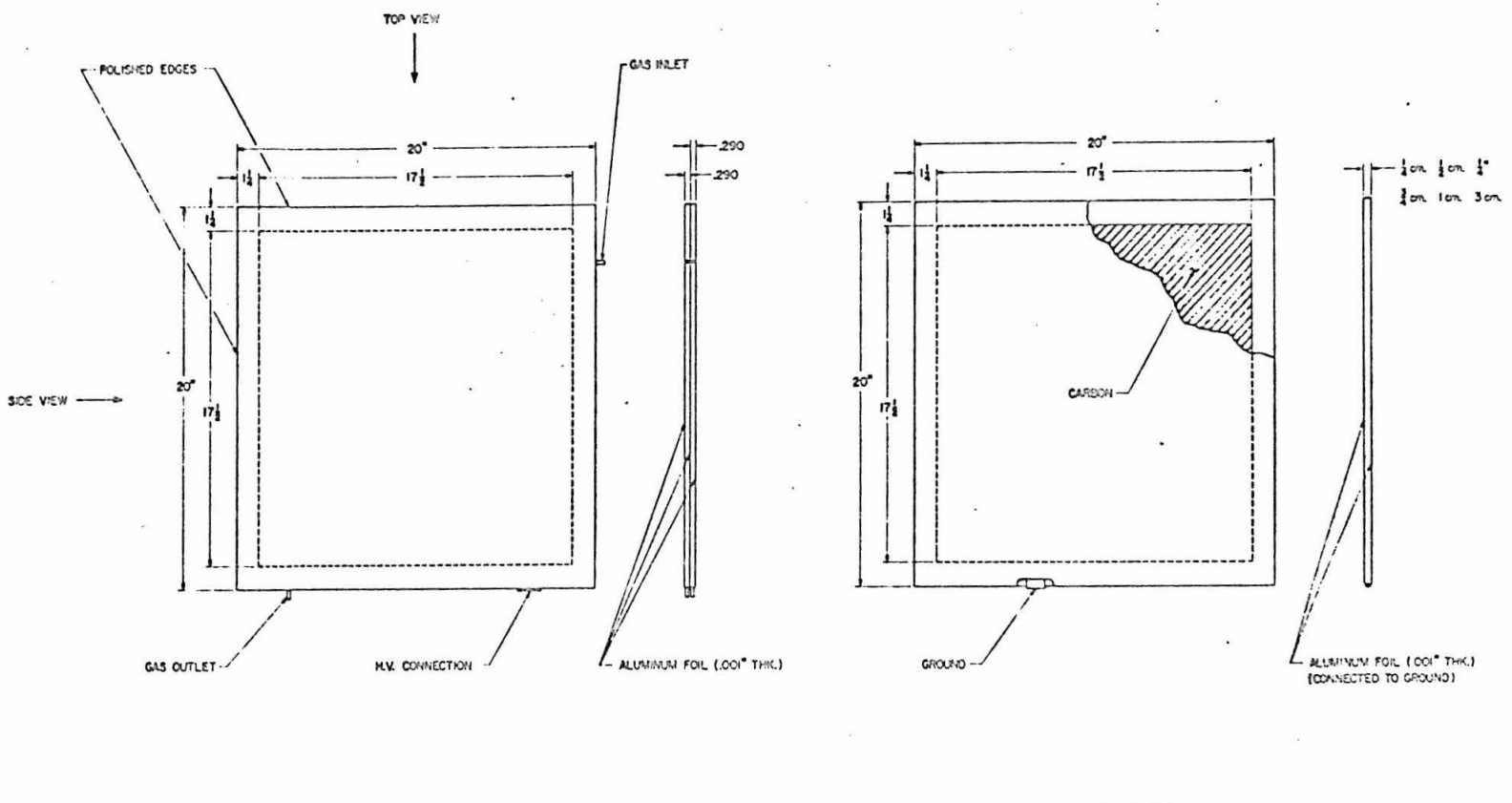

SPARKING MODULE

CARBON MODULE

Figure 6.10 Details of chamber module construction

of 19 feet. After we installed and aligned the lenses, we photographed a grid through them, and determined that distortions were negligible. The main distortions present came from machining irregularities, rather than the more common aberrations.

The placement of the lenses is shown in Figure 6.11, along with a schematic representation of our fiducial system. The fiducials were machined onto plastic strips which were end-lighted; they were rigidly attached to metal frames, and mounted independent of the spark chambers. In this way the thickness of the range chamber could be changed without moving the fiducials.

The straight edge seen in Figure 6.11 was used in surveying, and provided a reference line with respect to which the fiducials and proton counters could be centered. In general we measured the positions of fiducials and counter centers to about one minute of arc, or typically less than 0.5 mm, using a transit placed at the experimental origin. Distances from the origin were measured to about 1 mm.

6. Electronics

Figures 6.12 and 6.13 show the general features of the logic and readout systems. The logical requirements for an event trigger were explained in Section II, and

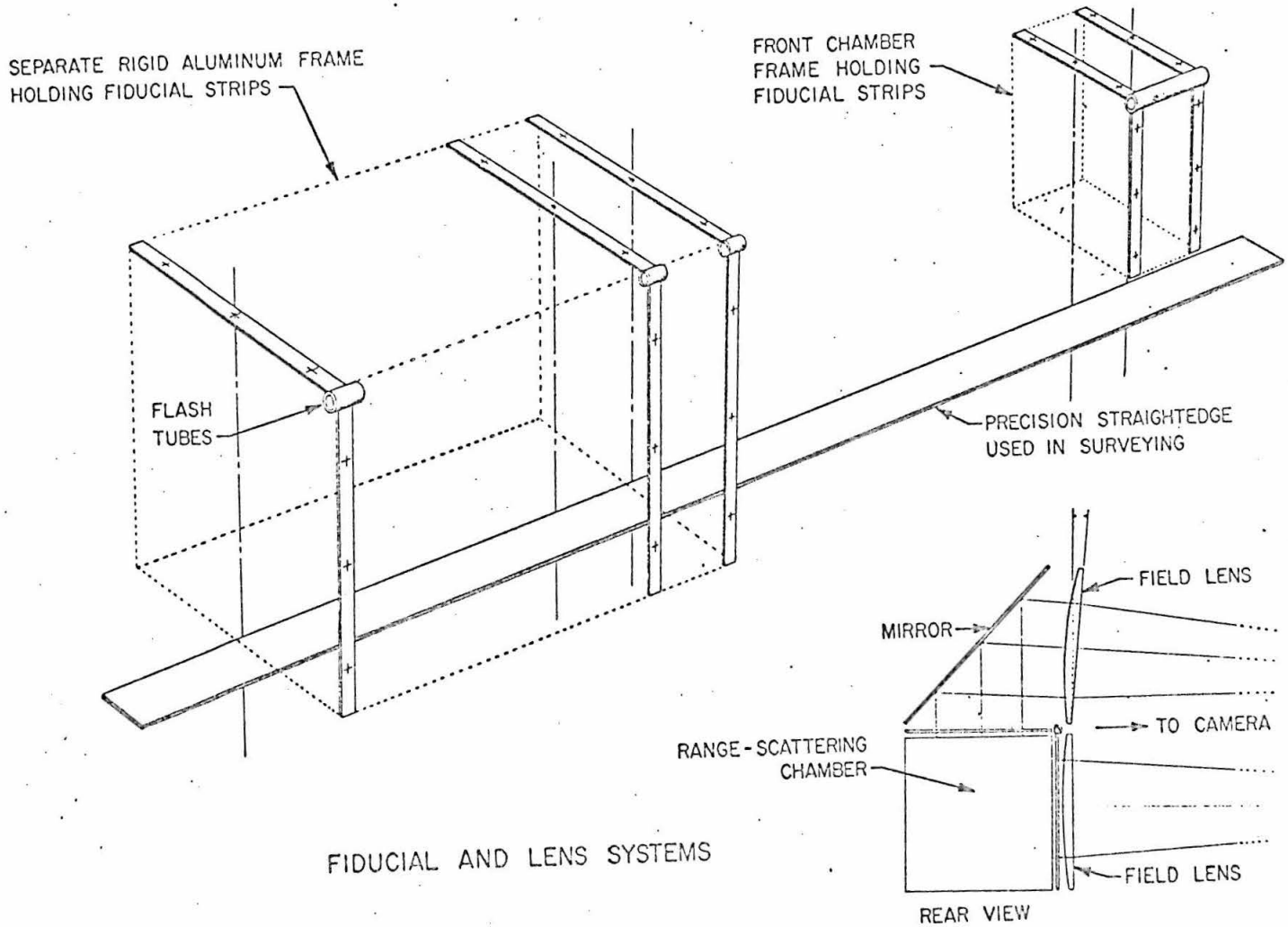

FIDUCIAL AND LENS SYSTEMS

Figure 6.11

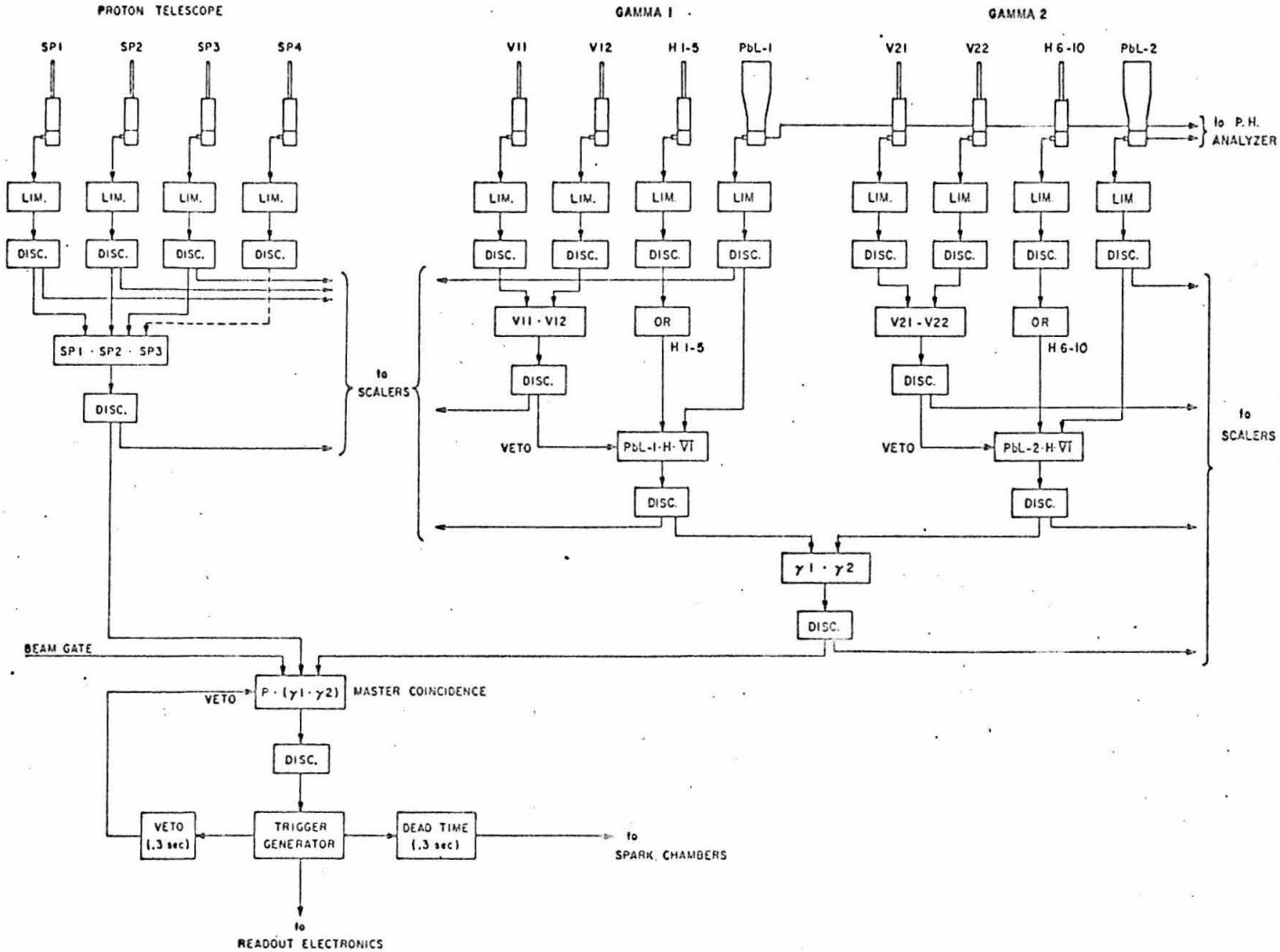

Figure 6.12 Fast logic for eta trigger

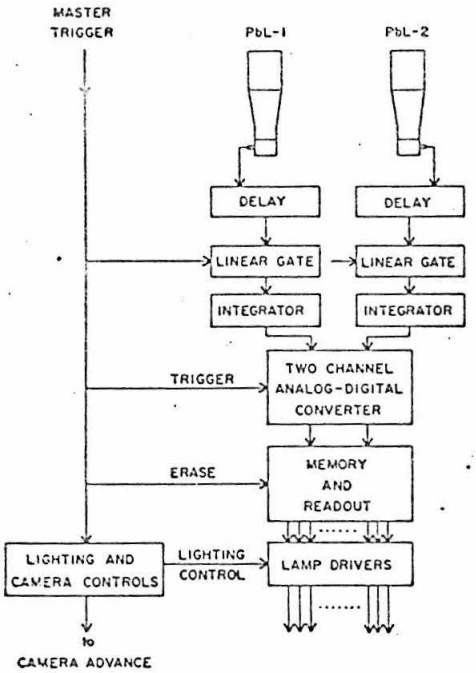

PULSE HEIGHT ELECTRONICS

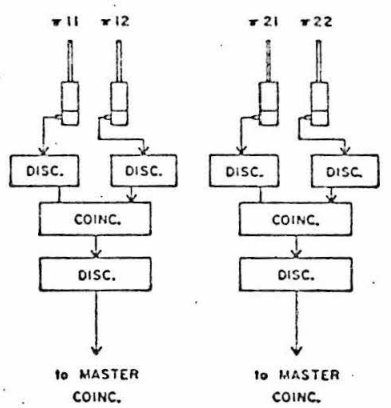

PION CALIBRATION FOR SHOWER COUNTERS

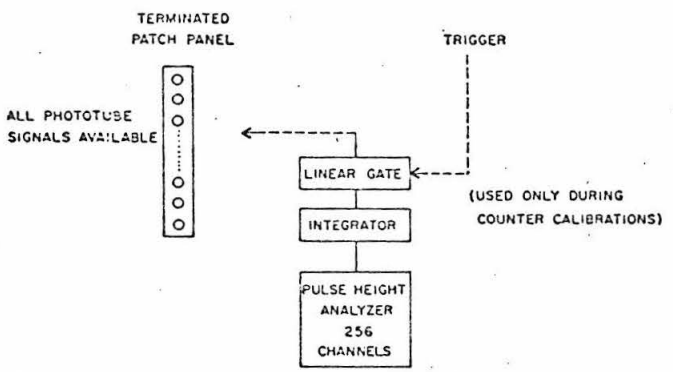

SYSTEM FOR COUNTER CALIBRATION

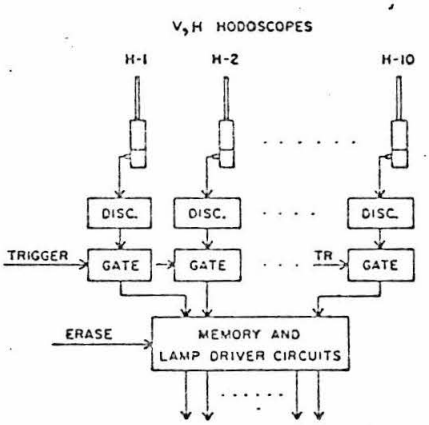

HODOSCOPE ELECTRONICS

Figure 6.13 Readout and calibration systems

we will not review them here. (In the two figures, SP refers to counters in the proton telescope and PbL to the lead-lucite shower counters.)

The outputs of all counters in the fast logic were put through clipped limiters and then discriminators. The pulses out of the disciminators were 10 nsec. wide, so that coincidence delay curves were 20 nsec. wide. The resulting dead time corrections were not severe.

7. Correction for Nuclear Interactions

The range-energy relationship for protons used in this experiment was based on the assumption that the protons lose energy only by ionization of the atoms in the material traversed. In reality, however, protons also undergo interactions with nuclei in matter. In addition to multiple Coulomb scattering, which is essentially elastic, the proton and nucleus may interact via nuclear forces. Depending upon the energy of the proton and the scattering angle, this interaction has some probability of being inelastic; various levels of the nucleus may be excited, and at higher energies, numerous catastrophic events may take place. When an inelastic interaction has occurred, the proton comes off with less energy than it started with, and the range of the proton no longer gives the true initial energy, but

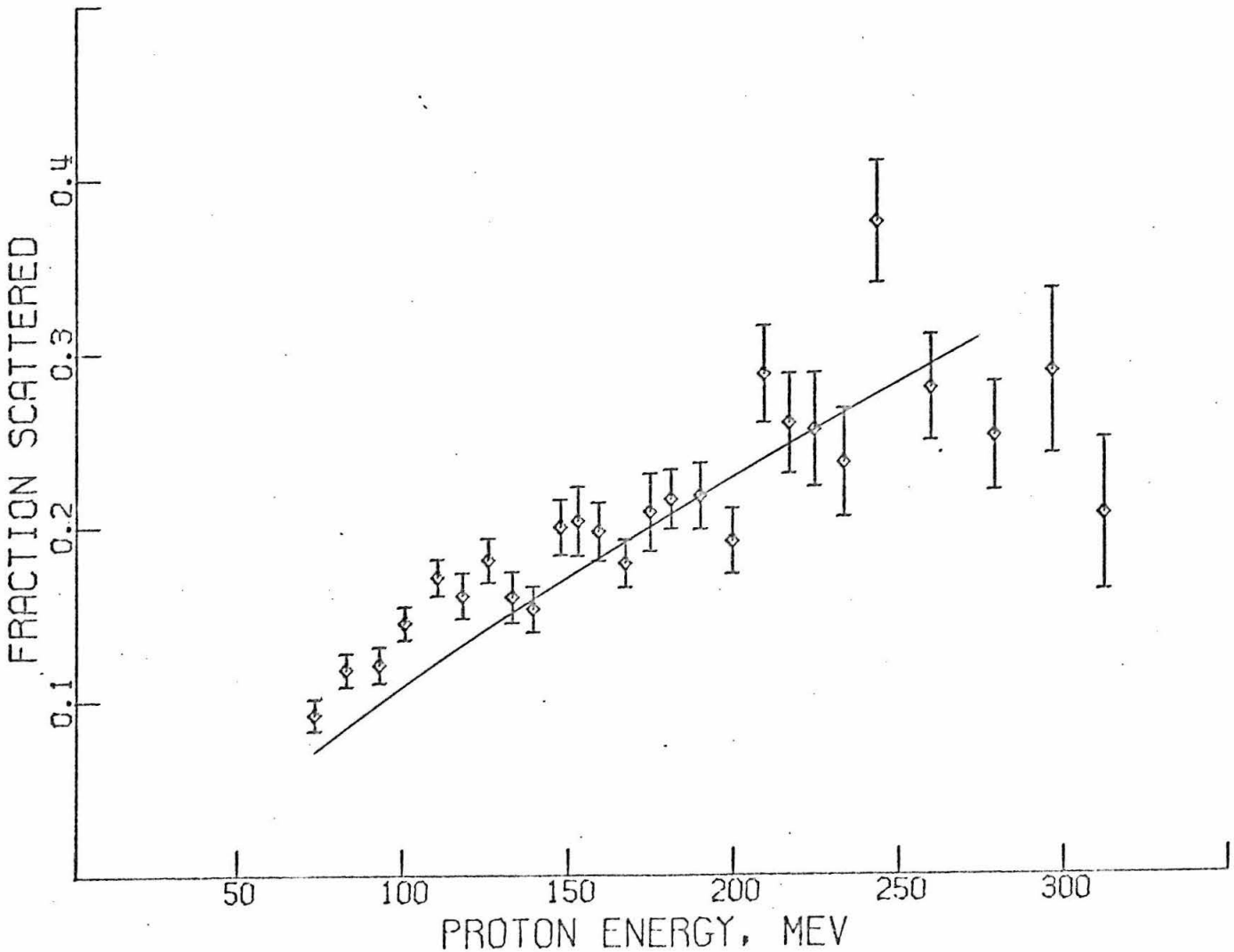

Figure 6.14 Fraction of protons observed to scatter as a function of initial proton energy. The curve gives the results of a calculation of this effect.

a smaller value. Since the proton energy goes into the calculation of the M_η, ΔE_η, and k, these nuclear interactions may lead to a systematic shift in the results.

One striking difference between elastic and inelastic processes is that the elastic cross section is peaked strongly forward, while the inelastic cross section remains fairly flat to large angles (about 30°). We used this fact to minimize the number of inelastically scattered events in our data. We did this by noting any event in which the proton was observed to scatter by more than 5° in either view of the spark chambers. These protons were more likely to have undergone an inelastic interaction than were the ones which did not scatter.

Only the non-scattering proton events were used in the final analysis, and a correction was made for events not counted.

Figure 6.14 shows the fraction of protons which scattered as a function of apparent initial proton energy for all the settings combined. These numbers were determined directly from the scan cards, so that no correction for non-normal trajectories has been included. The curve shown in the figure is a calculation based on known carbon-proton cross sections. A correction has been added at the low end, to account for multiple scattering between the second thin foil chamber and the range

chamber. This effect is indistinguishable from nuclear scattering in our setup, because the vertex, which is between chambers, cannot be seen.

The curve gives a reasonable fit to the observed data. Whatever discrepancy exists might have two causes: first, the calculation itself is uncertain near the end of the proton range, because the cross section is changing rapidly, and the geometry becomes complicated, especially at low proton energies; second, inelasticities could shift the data to lower energies with respect to the calculated curve.

The first effect might change the calculated curve by a few percent. As for the second, an average inelasticity of about 10 MeV would not be incompatible with the observed data. This amount of inelasticity changes the quoted cross sections by about one percent, an amount well within the limits of statistical error.

The actual correction was made with a smooth fit to the observed data, and not with the calculated curve. The correction was applied to the efficiency curves as a function of the proton energy. We estimate that the uncertainty introduced by the entire correction is about one or two percent.

REFERENCES

1. A. Pevsner et al., PRL 7, 421 (1961).
2. P. L. Bastien et al., PRL 8, 114 (1962).
3. M. Chrétien et al., PRL 9, 127 (1962).
4. C. Baltay, Conference on Meson Physics, University of Pennsylvania, Philadelphia, Pennsylvania, April 1968.
5. C. Bemporad, et al., Proceedings of the 1967 International Conference on Electron and Photon Interactions at High Energies, Stanford.
6. C. Bacci, et al., PRL 11, 37 (1963).
7. F. Bulos, et al., PRL 13, 486 (1964).
8. D. Berley, et al., Proceedings of the International Conference on High Energy Physics, Dubna, 1964.
9. D. Cline and M. Olsson, Proceedings of the 13th International Conference on High Energy Physics, Berkeley, California, 1966.
10. I. Gyuk and S. Tuan, PRL 14, 121 (1965).
11. C. Bacci, et al., PRL 20, 571 (1968).
12. C. A. Heusch, C. Y. Prescott, R. F. Dashen, PRL 17, 1019 (1966).
13. Desy Bubble chamber group, according to C. A. Heusch.
14. C. Bacci, PRL 16, 157 (1966).
15. B. Delcourt, et al., Orsay preprint.

16. R. Prepost, D. Lundquist and D. Quinn, PRL 18, 82 (1967).

17. C. A. Heusch, C. Y. Prescott, E. D. Bloom, and L. S. Rochester, PRL 17, 573 (1966).

18. W. S. C. Williams and F. Corbett, "Ionization Loss Range, and Straggling of Charged Particles," High Energy and Nuclear Physics Data Handbook, Rutherford High Energy Laboratory (1964).

19. J. V. Allaby, H. L. Lynch, and D. M. Ritson, Phys. Rev. 142, 887 (1966).

20. C. Y. Prescott, Caltech thesis (unpublished)(1966).

21. W. B. Richards et al., PRL 16, 1221 (1966).

22. E. Lohrmann, Proceedings of the 1967 International Symposium on Electron and Photon Interactions at High Energies, Stanford.

23. R. K. Logan and F. Uchiyama-Campbell, Phys. Rev. 153, 1634 (1967).

24. S. Minami, Phys. Rev. 147, 1123 (1966).

25. S. R. Deans and W. G. Holladay, Phys. Rev. 161, 1466 (1967).

26. F.B. Wolverton, Manual for BPAKI, Thick Radiator Bremsstrahlung computer program (unpublished).

27. H. A. Thiessen and J. Pine, CTSL Internal Report No. 22 (unpublished).

28. R. R. Wilson, Nucl. Instr. Methods 1, 101 (1957).

29. H. A. Thiessen, CTSL Internal Report No. 21 (unpublished).

30. E. D. Bloom, Caltech thesis (unpublished) (1967).